UNIVERSITÀ DEGLI STUDI DI PADOVA

DIPARTIMENTO DI SCIENZE CHIMICHE

CORSO DI LAUREA MAGISTRALE IN CHIMICA INDUSTRIALE

TESI DI LAUREA MAGISTRALE

Development of EC-SERS sensors for Cr(VI) in aqueous matrix.

Relatore: Dr. Lucio Litti

Correlatrice: Prof. Sara Bonacchi

Controrelatore: Prof. Stefano Agnoli

Laureanda: Sofia Nataloni

Anno Accademico 2024/2025

Index

1. Abstract and aim of the thesis

Nowadays, heavy metals are of significant concern for the environment and human health. Hexavalent chromium is one of the most important along others. Unlike the trivalent form, hexavalent chromium is classified as carcinogenic, making the monitoring of its environmental occurrence of crucial importance. The most used methods for detecting Cr(VI) relies on colorimetric assays, as with 1,5-Diphenilcarbazide for instance, as well as mass spectrometry and spectro-electrochemical techniques.

The aim of this thesis is the development of an Electrochemical-SERS based sensor dedicated to the detection of hexavalent chromium in aqueous matrixes. The sensor is composed by a thin film of gold nanoparticles functionalized with Nile Blue dyes. The reason for Nile Blue is about the reversibility of its reduction/oxidation reaction and its characteristic, bright, SERS signals. The hypothesis under the sensing principle considers that the reduced, SERS-silent, form of Nile Blue is produced by electrolysis. The presence of Cr(VI) repristinates the oxidized form of Nile Blue, eventually detected by means of electrochemical and Raman techniques.

Several thin film fabrication techniques are evaluated, namely dropcasting, inkjet printing, and spray coating, which proved to be the most effective choice.

The EC-SERS technique would allow the simultaneous Cr(VI) monitoring by electrochemical and spectroscopic perspectives. One of the most interesting advantage of the sensor herein presented is the ability to be regenerated for multiple measurements without compromising the output reliability.

Abstract e scopo della tesi

Al giorno d'oggi, i metalli pesanti sono di grande preoccupazione per l'ambiente e la salute umana. Il cromo esavalente è tra i più importanti insieme ad altri. A differenza della forma trivalente, il cromo esavalente è classificato come cancerogeno, rendendo il suo monitoraggio di cruciale importanza. I metodi più utilizzati per rilevare il Cr(VI) si basano su saggi colorimetrici, come ad esempio con il 1,5-difenilcarbazide, oltre a tecniche di spettrometria di massa e tecniche spettro-elettrochimiche.

Lo scopo di questa tesi è lo sviluppo di un sensore basato su una tecnica ibrida elettrochimica-SERS per la rilevazione del cromo esavalente in matrici acquose. Il sensore è composto da un sottile film di nanoparticelle d'oro funzionalizzate con il colorante Nile Blue. La scelta del Nile Blue è legata alla reversibilità della sua reazione di riduzione/ossidazione ed ai suoi segnali SERS caratteristici e intensi. L'ipotesi sottostante il funzionamento del sensore considera la forma ridotta del Nile Blue, che mostra bassi segnali SERS è prodotta per elettrolisi. La presenza di Cr(VI) ripristina la forma ossidata di Nile Blue, rilevata mediante tecniche elettrochimiche e Raman.

Questo lavoro di tesi si interessa altresì della valutazione di diverse tecniche di fabbricazione di sottili film, vale a dire dropcasting, stampa a getto d'inchiostro e deposizione via aerografo, delle quali quest'ultima si è dimostrata la scelta più efficace.

La tecnica EC-SERS potrebbe consentire il monitoraggio simultaneo di Cr(VI) attraverso tecniche elettrochimiche e spettroscopiche. Uno dei vantaggi più interessanti del sensore qui presentato è la capacità di essere rigenerato per successive misurazioni senza comprometterne la affidabilità.

2. Introduction

2.1 About hexavalent chromium

Chromium is widely used in the chemical industry for different applications such as pigments, metal plating, or leather tanning and for the production of chemicals.[1] As a result, different species of chromium can be released into the environment (soil, surface, and ground waters) and it comes ultimately available to humans. Chromium can exist in several chemical forms between Cr^0 and Cr(VI). However, only trivalent and hexavalent chromium are stable enough to occur in the environment.

The most common form in which Cr(VI) is found is chromate CrO_4^{2-}, dichromate $Cr_2O_7^{2-}$, and the corresponding acids, while Cr(III) is present as a cation. The most oxidized state can be readily reduced to Cr(III) as it is the most stable form of chromium in aqueous samples (Figure 1).[2]

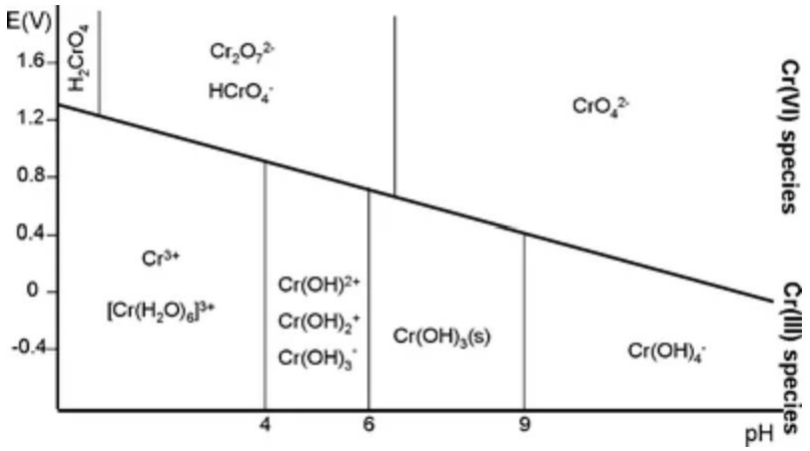

Figure 1:Stable chemical species of chromium as a function of potential E and pH. Cr(III) species are the most stable in water in a wide pH range and in absent of applied potential. The values were taken using a SHE reference electrode in standard contitions.[2]

2.1.1. Environmental issues

Environmental pollution, that effect water, soils, and atmosphere, has emerged as a pressing concern since the advent of the industrial era and now poses a significant threat to contemporary society. Pollution is delineated as the introduction of substances into the environment that elicit physical, chemical, or biological disruptions to living organisms, including humans. Various categories of pollutants exist, including inorganic, biological, and organic compounds, such as metals, salts, bacteria, viruses, and organic substances with a propensity for bioaccumulation, such as pesticides. Of particular concern are heavy metals, including lead, nickel, chromium, cadmium, arsenic, mercury, cobalt, selenium, zinc, and copper that may arise from natural sources, such as volcanic activities, or

result from anthropogenic processes. Heavy metals become toxic when they are not metabolized by the body and accumulate in soft tissues. They can enter the human body through food, water, air, or absorption through the skin when individuals meet them in agricultural, manufacturing, pharmaceutical, industrial, or residential settings. Industrial exposure represents a common source for adults, while ingestion is the most common exposure route for children. Both natural and human activities are contaminating the environment and its resources, exceeding the environment's capacity to manage them.[3]

Among these heavy metals, hexavalent chromium is in the top 10 of toxic substances in the world, according to Agency for Toxic Substances and Disease Registry (ATSDR)[4] and the International Agency for Research on Cancer (IARC), that has classified Cr (VI) compounds as human carcinogens in 1990. US Environmental Protection Agency (USEPA) achieved the same classification. The maximum chromium concentration allowed in the drinking-water is 50 μg/L (total chromium).[5] For what concern the hexavalent chromium, according to Italian Dlgs 31/2001, for water intended for human consumption, the precautionary limit is 10μg/L.[6] Chromium highlights a fascinating contrast in behavior across distinct species. Its two primary oxidation states, Cr (III) and Cr (VI), exhibit distinct levels of mobility and bioavailability. Generally, the mobility of Cr(III) compounds will be very low because of the formation of stationary complexes and have low solubility, whereas Cr(VI) compounds are highly mobile, soluble, and consequently more bioavailable.[7]

Chromium is an element in which different oxidation states show opposite biological behaviors:

- Cr (III) serves as an essential nutrient for the human body, playing a role in carbohydrate, lipid, and protein metabolism. Since this cation has a low solubility it’s not able to penetrate cell membranes, unless bounded to a suitable organic ligand.[8]
- Cr (VI) is unequivocally toxic due to its elevated oxidation potential and capability to breach biological membranes. The permeability of Cr (VI) through cell membranes is facilitated by its structural resemblance to anions like SO_4^{2-} or PO_4^{3-}, which are transported through specific anion exchange channels. This ability to penetrate cell membranes makes Cr(VI) 1000 times more cytotoxic than Cr(III).[8]

2.1.2. Standard methods for quantifying chromium

There are many methods to detect and quantify chromium. The United States Environmental Protection Agency (US EPA) recognizes four methods for determination of Cr (VI):[9]

- Co-precipitation

- Colorimetric with diphenyl carbazide
- Chelation/extraction
- Differential pulse polarography

One of the main powerful analytical tools available for analyzing heavy metals ions is high-performance liquid chromatography coupled with Inductively Coupled Plasma – Mass Spectroscopy (HPLC-ICP-MS). Distinction between Cr(III) and Cr(VI) can be achieved by utilizing the affinity of Cr(III) to ethylenediaminetetraacetic acid (EDTA).[10] The limit of detection (LOD) typically falls within the range of 0.04 µg/L to 0.4 µg/L[8]. Despite the low LOD, the ICP-MS technique encounters spectral interferences due to ions with identical mass-to-charge ratios as the analyte of interest. Additionally, other interferents may contribute to nebulizer clogging and accumulate on the torch and ion lens. Furthermore, it is worth nothing that water samples often contain calcium and magnesium levels up to 100 mg/L, significantly higher than the expected chromium concentration. Consequently, substantial quantities of EDTA are required for these experiments, potentially giving rise to matrix effects. Those last techniques are highly limited by their high-cost e non-portable instrumentations, sophisticated sample preparation and the needs of professional operators.

2.1.3 State of the art in novel methods for detection and quantification of hexavalent chromium

Given the toxicity and the importance of detecting chromium, the topic of finding an innovative method that lowers the limit of detection, requires simple sample preparation, and low-cost is still a relevant issue in the literature today. There are various approaches that use either electrochemical or optical methods.[11–15]

Among all, one of the most used methods for detecting hexavalent chromium is the colorimetric method using 1,5-Diphenylcarbazide (DPC). It is a redox reaction in acid conditions in which the 1,5-Diphenylcarbazide reacts with hexavalent chromium and form the 1,5-Diphenylcarbazone and Cr (III). The latter then react to form a positively charged complex that is characterized by an absorption band at 540 nm and a purple color.

$$3DPC + 2CrO_4^{2-} + 10H^+ \rightarrow 2Cr^{3+} + 8H_2O + 3DPCO$$

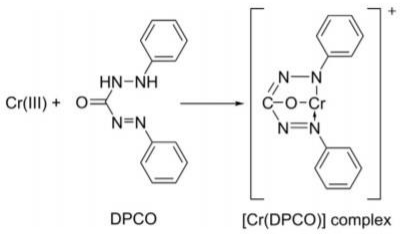

Figure 2: Equation of the reaction between DPC and Cr (VI) and the complex formation between DPC and Cr (III).

As reported in the chemical equation above, the 1,5-Diphenylcarabazide reacts exclusively with the hexavalent chromium and not with the trivalent ion, so this method is selective for the oxidized form. Since the detection of hexavalent chromium in drinking water has become highly important and of great interest, several methods have been tested that utilize the redox reaction between DPC and Cr(VI).

Over the past decade, nanomaterials such as gold nanoparticles (AuNPs), have garnered significant attention for developing colorimetric and fluorescent assay systems due to their distinctive optical properties. It has been demonstrated that properly functionalizing a nanomaterial allows the detection of a range of heavy metals such as Hg(II), Cd(II), Pb(II), Cu(II), Cr(III), and more importantly Cr(VI). One method consists in detecting Cr(VI) using DPC modified AuNPs (DPC-AuNPs).[16] In this work the gold nanoparticles were functionalized with 1,5-Diphenylcarbazide, then the Cr(VI) was added and DPC oxidized to DPCO that complexes with the in situ reduced Cr(III) as reported in the scheme in Figure 3:

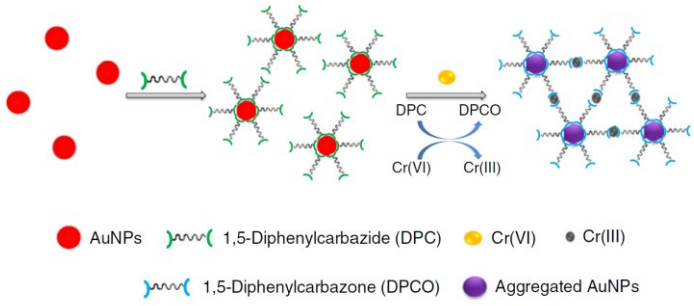

Figure 3:Schematic illustration of the in situ redox reaction based approach for the detection of Cr(VI).[16]

As reported in the scheme above, once the complexation occurs the gold nanoparticles aggregate, resulting in a color change from red wine to gray due to the shift in the SPR absorbance peak and intensity from 520 nm (DPC-AuNPs) to 630 nm (DPC-AuNP when adding Cr(VI)). This method was demonstrated to be highly selective for Cr(VI), while other cations like Na^{+}, Mg^{2+}, Hg^{2+} Ag^{2+} and $Fe^{2+/3+}$ exhibited no color changes. The limit of detection in this case was 0.3 µM, still not according to Italian Dlgs 31/2001, as the precautionary limit for Cr(VI) in drinking water is 0.02 µM. Another limitation of this work is the irreversible aggregation of the nanoparticles, which prevents them from being reused.

In an another example it was developed a colorimetric probe for chromium speciation using citrate-capped AuNPs.[17] Cr(III) ions, chelated by the citrates, form a stable Cr(III)-citrate complex, inducing the aggregation of AuNPs and changing the color from pink-red to blue. As reported in Figure 4, for

detecting Cr(VI) in water samples, it was first reduced to Cr(III) with ascorbic acid to calculate the total chromium content and then, by subtracting the Cr(III) concentration from the total chromium amount, Cr(VI) was determined. Cr(III) can bind with the surface citrate and trigger the aggregation of citrate-capped AuNPs changing color from red to blue.

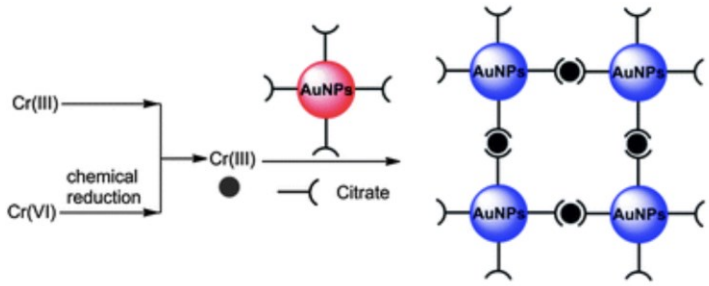

Figure 4:Schematic illustration of the colorimetric speciation con chromium with an AuNP-based probe.[17]

The major limitation of this method is not only that the LOD, 0.3 µM, is higher than the one requested by the Italian Dlgs, but more importantly is not specific to Cr(VI).

Another method involves functionalizing AuNPs with 1,4-dithiothreitol (DTT) for selectively detecting nanomolar Cr(VI) in aqueous solution.[18] Even in this method the functionalized gold nanoparticles aggregates once adding the Cr(VI) solution causing a notable red-shift (from 520 nm to 650 nm) of the SPR peak as shown in Figure 5b.

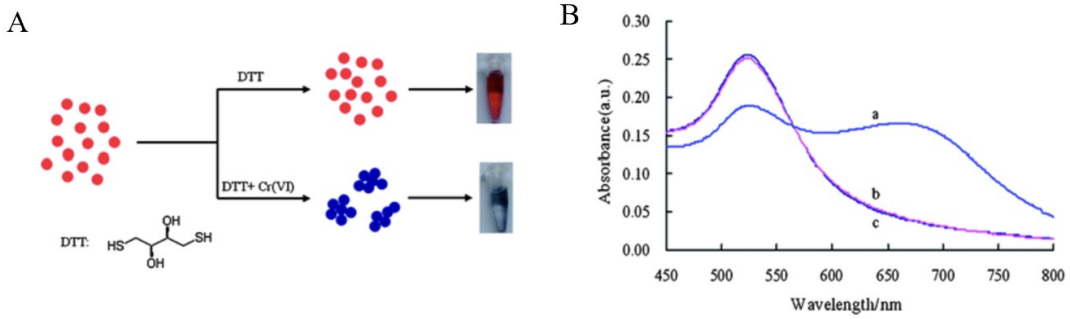

Figure 5: A) Schematic illustration of the colorimetric speciation con chromium with an DTT-AuNPs based probe.[18] *B) UV-vis absorption spectra of the nanoparticles. a) DTT-AuNPs + 0.5 µM Cr(VI), b) AuNPs + 0.5 µM Cr(VI), c)DTT-AuNPs .*[18]

Regarding the Cr(VI) selectivity, this method showed to be affected by other metal cations like Hg^{2+}, Cu^{2+}, Pb^{2+} and Cu^{2+}. The LOD is 0.6 µM.

To create reusable sensors, methods utilizing SERS (Surface Enhanced Raman Scattering, as better presented in the next chapters) have been proposed for detecting Cr(VI), employing nanostructured substrates. For example, a sensitive SERS sensor was developed using hollow sea urchin-like TiO_2@Ag nanoparticles functionalized with glutathione (GSH), with a LOD for Cr(VI) of 1.45 nM.[19] Another way to detect Cr(VI) was to use a octahedral Cu_2O@Ag nanocomposites as a

SERS substrate with a detection limit of 0.028 μg/L.[20] SERS enables the detection of lower quantities of Cr(VI) and allows for the reuse of the substrates. Unlike previous colorimetric techniques, SERS does not result in nanoparticle aggregation, thus maintain substrate integrity for multiple uses.

Part of this thesis project is to develop a gold nanoparticle sensor fabricated via drop casting for detecting hexavalent chromium by SERS using the redox reaction between Cr(VI) and 1,5-Diphenylcarbazide, with the aim to reach lower concentration than 0.01 μM.

2.2 Electrochemical methods

The electrochemical techniques concern a chemical transformation initiated, or influenced, by an electrical stimulus, such a as current or potential. These processes rely on transfer of electrons between an electrode and a molecule or ion, resulting in a change in its oxidation state. This electron transfer process (ET) can occur spontaneously, driven by the release of chemical energy (as in batteries), or non-spontaneously, requiring an externally applied voltage or current (as in an electrochemical cell). Both spontaneous and non-spontaneous ET processes involve redox reactions, where the oxidation states of reactants change due to the transfer of electrons. In an electrochemical cell, an external stimulus, typically a potential difference, drives the ET process at the electrode surface. This results in the reduction (gain of electrons) or oxidation (loss of electrons) of the analyte species.

2.2.1 Cyclic Voltammetry

Cyclic voltammetry (CV) is one of the most used electrochemical techniques for the study of electroactive species. In a common CV experiment the working electrode's potential is scanned linearly with time, until reaching the so-called switching potential, where the potential is reversed, returning the electrode to its initial state (more information will be provided later, in this paragraph). The resulting current response at the working electrode is plotted against the applied voltage to generate a cyclic voltammogram (i vs V graph). This technique is widely used to investigate the electrochemical properties of analytes in solution, or molecules adsorbed onto the electrode surface.

To perform a cyclic voltammetry, a three-electrode cell must be used in which the three electrodes are:

- A working electrode (in which the differential voltage is applied and the current passing through is recorded)
- A counter electrode (needed to measure the current)
- A reference electrode (needed to control and measure the applied potential)

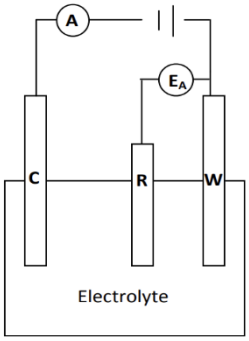

Figure 6: Simple scheme of a three-electrode configuration where EA is the applied voltage and C, W and R are the counter, working and reference electrodes. A stand for the amperometric circuit.[21]

The working electrode acts as the site for the electrochemical reaction. A schematic representation of a common three-electrodes cell is reported in Figure 6.

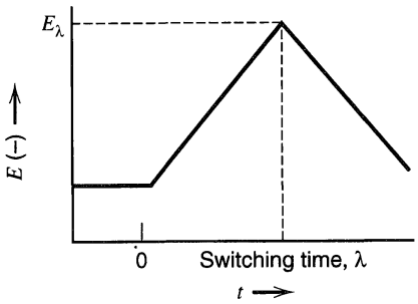

Figure 7: Trend of potential over time in a cyclic voltammetry experiment.[23]

$$0 < t \leq \lambda \qquad E = E_i + vt$$

$$t > \lambda \qquad E = E_i + 2v\lambda - vt$$

As previously discussed, cyclic voltammetry (CV) involves a linear potential scan with time, followed by a reversal after reaching a defined switching potential (E_λ) as shown in Figure 7. The applied potential (E) is described by the equation E = v × t, where *v* is the scan rate (V/s) and *t* is time. During the forward scan (anodic scan), the potential increases progressively, driving the oxidation process, until it reaches the switching potential (E_λ) Subsequently, the potential is reversed according to the same equation (cathodic scan), driving the reduction, and returning the electrode to its initial potential.

When reporting CV data, two conventions are commonly used: the US Convention and the IUPAC Convention[21] as reported in Figure 8:

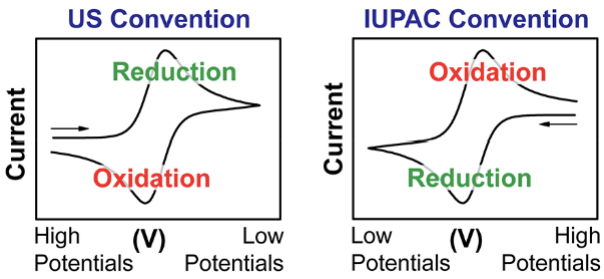

Figure 8: Voltammograms that show the two conventions commonly used.[22]

A typical cyclic voltammogram is shown in Figure 9.

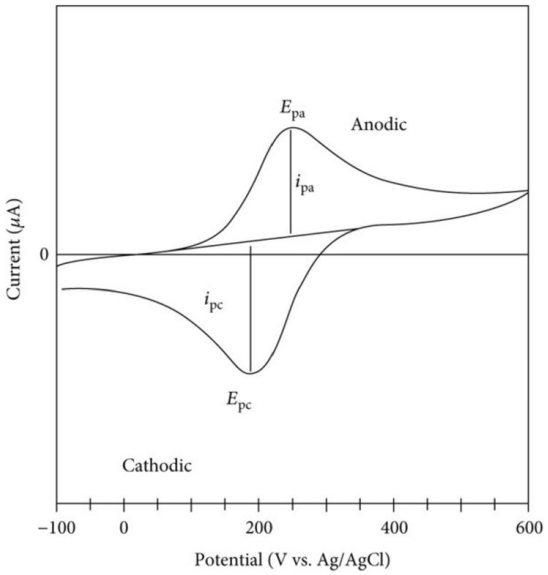

Figure 9: Common Cyclic voltammogram, with the IUPAC convention, where E_{pa} is the anodic peak, E_{pc} the cathodic peak, i_{pc} the cathodic peak current and i_{pa} the anodic peak current.

The most important features in a cyclic voltammogram:

- Peak positions (E_{pc} and E_{pa})
- Peak intensity (i_{pa} and i_{pc})
- Peak shapes
- Peak height ratios
- Peak separation

The peak positions, shapes, and separations provide valuable information about the investigated chemical species. The peak position relates directly to the formal reduction potential of the analyte. This potential reflects the tendency of the analyte to undergo reduction or oxidation, indicating its ability to act as a reducing or oxidizing agent. Peak shape offer insights into the underlying electron

transfer process. In the peak separation, the potential difference between the anodic and cathodic peaks reflects the reversibility of the ET process. Smaller peak separations suggest a more reversible process, while larger separations indicate less reversibility. Additionally, peak intensity and their ratios can provide quantitative information, such as the concentration of the analyte.

In a CV, as well as in all electrochemical experiments in general, a very important role is played by the supporting electrolyte. The supporting electrolyte serves as an inert solvent that operates as a conductive medium. It is usually ionic and present in a high concentration if compared to the reactive species to minimize the solution resistance and inhibit the migration of charged species induced by the electric field. Another very important factor is the scan rate. It controls how fast the applied potential is scanned. Faster scan rates lead to a decrease in the size of the diffusion layer; as a consequence, higher currents are observed.[21] If the process is diffusion controlled (analyte dissolved in the electrochemical solution) the peak currents are proportional to the square root of the scan rate, $v^{1/2}$, as shown in the Randles-Sevick equation (Eq. 1):

Eq. 1 $$|i_p| = 0.4463nFAC_O^*(\frac{nF}{RT})^{1/2}v^{1/2}D_O^{1/2}$$

Where n is the number of electrons transferred during the process, F is the Faraday constant, A is the area of the electrode, C_O^* is the bulk concentration of the redox-active molecule, R is the universal gas constant, v the scan rate and D_0 the diffusion coefficient of the molecule. However, if the electrochemical process involves adsorbed species, the peak current is directly proportional to the scan rate, v.

2.2.2 Differential pulse voltammetry

Differential Pulse Voltammetry (DPV) is a complementary technique in respect to CV. Indeed, a DPV experiment needs the same 3-electrodes set-up used in CV, already explained in chapter 2.2.1 The major difference between the two methods is that, in DPV, the potential is applied in one direction (anodic or cathodic) in the form of "pulses" along a linear ramp, as reported in Figure 10.[22]

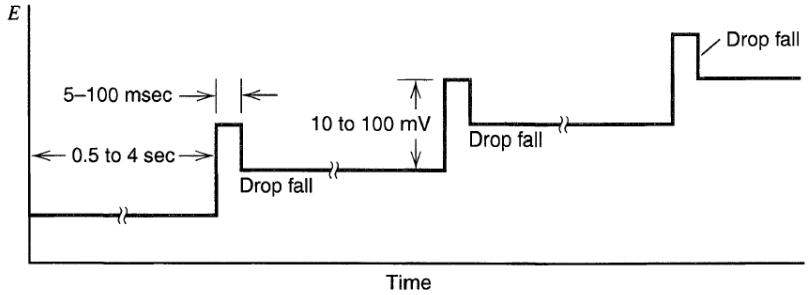

Figure 10: Scheme describing how the potential is applied during a DPV experiment, together with some common experimental parameters.[23]

In DPV, the current is measured before and after the application of every pulse (Fig. 11),[22] The difference between the currents before and after the pulse (*Δi)* is used to remove most of the capacitive current, resulting in an enhanced electrochemical response. This is very helpful especially when measuring a poorly concentrated species, or when his diffusion coefficient (D) is very low (the current intensity depends on D). Hence a differential measure of the current is achieved, resulting in a peak-shaped voltammogram.

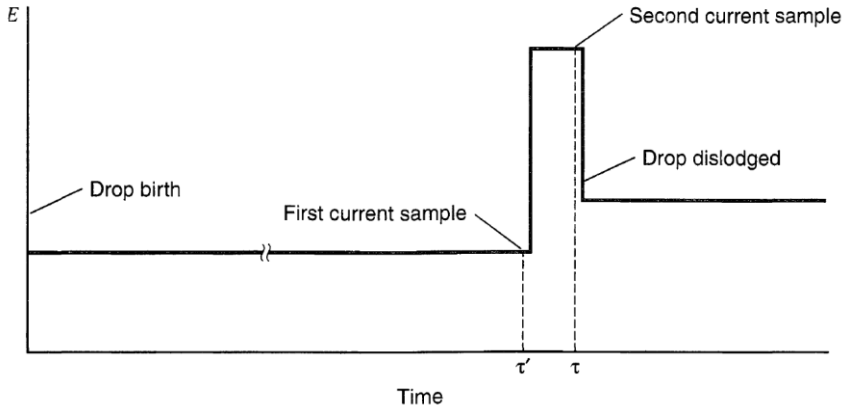

Figure 11: Scheme describing how the potential is applied during a DPV experiment, in which the time where the current is recorded underlined (τ' and τ).[23]

2.2.3. Chronoamperometry

Chronoamperometry is another prevalent electrochemical technique that measures current as a function of time, keeping constant the applied potential at the working electrode (Figure 12). To achieve complete reduction or oxidation of the target analyte, cyclic voltammetry is first employed to identify the optimal potential that drives the desired redox reaction. This information about the potential is then directly applied to design the chronoamperometry experiment. In both cases, when the analyte is diffusing in the electrochemical solution or immobilized on the electrode surface, the current recorded is proportional to the analyte concentration.

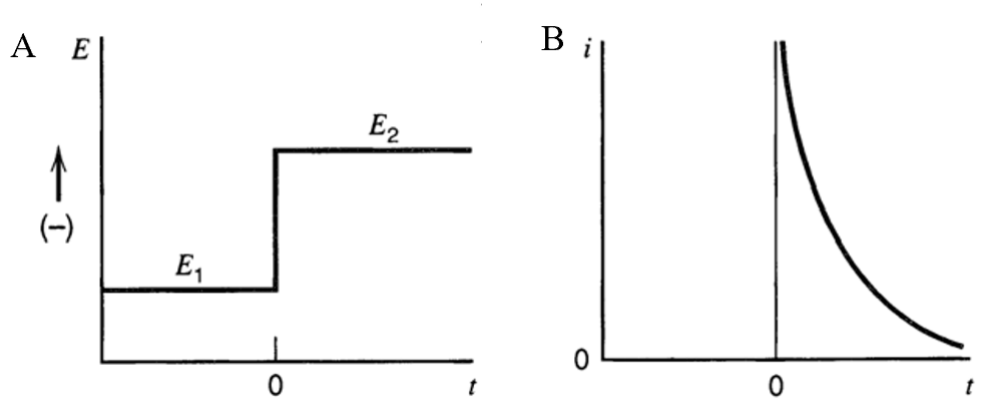

Figure 12: (A) Waveform for a step experiment in which species O is electro-inactive at E_1 but is reduced at E_2. (B) Current flow vs. time.[23]

2.3 Raman Spectroscopy

2.3.1. Raman Theory.

The Raman scattering is a phenomenon observed when studying the scattering of light by a material in gas, liquid, or solid phases.

Two different components can be observed analyzing the scattered light(Figure 13):[23]

- *Elastic components*: also known as Rayleigh scattering. In this case the scattered radiation has the same energy as the incident radiation. $\omega_S = \omega_L$
- *Anelastic components:* also known as Raman scattering. In this situation, the scattered radiation has a different frequency in respect to the incident one: $\omega_S \neq \omega_L$. The Raman scattering components are further divided into *Stokes* and *anti-Stokes* with frequency respectively $\omega_S < \omega_L$ and $\omega_S > \omega_L$.

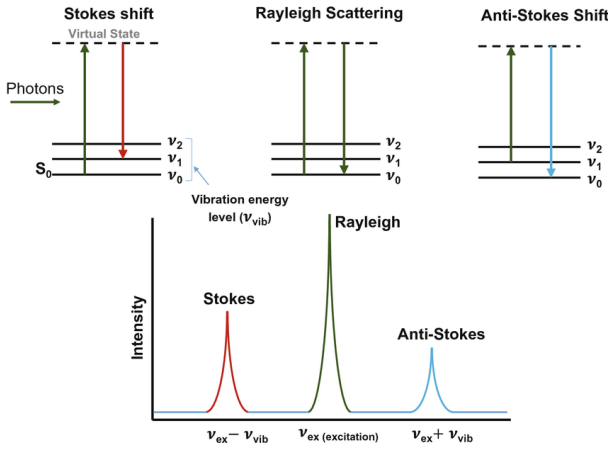

Figure 13: Raman spectra with all three components: Rayleigh, Stokes and Anti-stokes.[27]

Both scattering phenomena can be explained by the introduction of a so-called virtual state that has an intermediate energy between the ground state and the first exited state, as shown in Figure 13 via a dotted line. As shown in Figure 14, in the Rayleigh scattering the system starts from the ground state, populates the virtual state and returns to the same starting vibrational state with the same energy hv_0.[24] Whereas for the Raman scattering the starting and arrival point do not match regarding the stokes components, the system starts form the ground level with energy hv_0, populates the virtual state, and returns to the vibrational state v_1 with energy $hv_0 - hv_{vib}$. Instead for the anti-stokes components, the starting vibrational state is v1 with energy hv_0, while the destination state is the ground state with energy $hv_0 + hv_{vib}$. Since the ground state is the most populated at room temperature due to Boltzmann distribution, this event is less probable and the anti-Stokes signals are therefore less intense than the Stokes one.

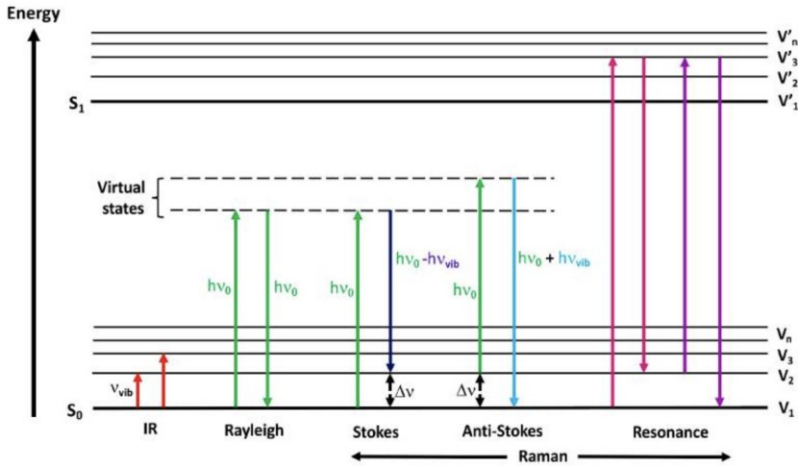

Figure 14: Jablonski energy diagram showing the transitions involved during infrared absorption, Rayleigh, Raman Stokes, anti-stokes and resonance Raman scattering.[27]

The variation energy between the incident and the scattered radiation corresponds to the energy of the vibrational states and remains unaffected by the frequency of the incident radiation. Consequently, a Raman spectrum is represented as a function of this difference (Raman shift), usually expressed as wavenumber.[25]

The Raman scattering, from a classic mechanic point of view, is described as the induced dipole oscillation (μ_{ind} Eq.2) triggered by an incident electric field on a molecule.

Eq. 2 $$\mu_{ind}(t) = \alpha\, \vec{E}\,(t)$$

The induced electric dipole moment varies over time, oscillating accordingly to the electric field $\vec{E}(t)$ (Eq.3), with frequency ω.

Eq. 3 $$\vec{E}(t) = E_0 \cos(\omega t)\ with\ \omega = 2\pi v$$

The molecular polarizability tensor accounts for the perturbation of the molecular electronic distribution under a proper stimulus. This is clearly a function of the nuclei position, that are not stationary but move around their equilibrium positions. This results in a pattern of the "bond distance" coordinates, known as normal vibrational modes, expressed in equation 4 following the harmonic oscillator approximation:

Eq. 4 $$Q_i(t) = Q_0 \cos(\omega t)$$

This nuclear motion makes the polarizability α non-constant against time.

The dependance of α by the nuclear motion can be expressed as a Taylor series expansion for each normal vibrational mode Q_i. Cutting the expansion at the first term (Eq. 5):

Eq. 5 $$\alpha(t) = \alpha_0 + (\frac{\partial \alpha}{\partial Q_i})_0 Q_i(t)$$

Combining the previous equations is obtained:

Eq.6 $\mu(t) = \alpha_0 E_0 \cos(2\pi v_0 t) + \frac{1}{2} E_0 Q_i^0 (\frac{\partial \alpha}{\partial Q_i})_0 \cos[2\pi(v_0 - v_i)t] + \frac{1}{2} E_0 Q_i^0 (\frac{\partial \alpha}{\partial Q_i})_0 \cos[2\pi(v_0 + v_i)t]$

The first term of the equation represents Rayleigh scattering, the second the stokes signals, while the third one the anti-stokes signals.

From this last equation is possible to derive the selection rule for Raman spectroscopy:

Eq. 7 $$\left(\frac{\partial \alpha}{\partial Q}\right) \neq 0$$

Therefore, it can be stated that only the vibrational modes that induce a variation on the polarizability are Raman-active.

It is worth nothing that glass (Si-O) and water (O-H) have polarizability tensors barely influenced by bond vibrations, so that they possess a low Raman scattering cross section. This is the reason why Raman measures can be easily run over glass or in wet, in respect to IR spectroscopy.

The two most important drawbacks of Raman spectroscopy are the fact that the signals are usually weak, only about one in 10^6 photons undergo Raman scattering, and the strong interference that fluorescence may cause, when present.

A generic Raman signal I at the frequency ω, is function of the molecular Raman cross-section $\sigma(\omega)$:

Eq. 8 $$I(\omega) = \sigma(\omega) N_0 I_0(\omega)$$

Where $I_0(\omega)$ is the intensity of the incident light and N_0 the population of the initial vibrational state. This is why Stokes and Anti-Stokes signals have different intensity.

The cross-section $\sigma(\omega)$ can be expressed as follows:

Eq. 9 $$\sigma(\omega) = \frac{8\pi\omega^4}{3c^4}|\alpha(\omega)|^2 = \frac{8\pi\omega^4}{3c^4}\frac{|\langle e|\mu|g\rangle|^4}{(\omega_{eg}-\omega)^2+\left(\Gamma_e/_2\right)^2}$$

Where ω is the angular frequency of the radiation, c is the light speed, $\alpha(\omega)$ the polarizability, $|\langle e|\mu|g\rangle|^4$ is the modulus of the transition electric dipole moment for a transition where e and g are the initial and final states, ω_{eg} is the difference between the angular frequency of the two states, and finally Γ_e is the damping factor for the transition. Typical values of $\sigma(\omega)$ are approximately 10^{-31} cm^2/molecule.[26] As reported in Eq. 9, when the angular frequency of the laser ω matches or is close to ω_{eg}, the denominator of the equation approaches zero, causing $\sigma(\omega)$ to reach its maximum value. Operating under resonance conditions typically involves using lasers with wavelengths in the visible range (350-780 nm) or near infrared range (780-2200 nm). When the energy of the incident radiation is near the first molecular electronic transition energy, Resonant Raman Scattering occurs. Although this significantly increases the Raman cross section, resonance excitation is not always beneficial, as it can also induce fluorescence (or even phosphorescence), which often completely masks the Resonant Raman signals.[27]

Another method to achieve a Raman spectrum with a sufficient intensity is to use highly concentrated samples, or even samples in a powder form. Additionally, nanostructured materials can enhance the Raman scattering effect.

2.3.2. SERS technique.

To overcome the weakness of the Raman signals, the Surface-Enhanced Raman Scattering (SERS) effect is used. This effect involves a relevant enhancement of the Raman signal of a molecule by several orders of magnitude. The enhancement arises from the interaction between the electromagnetic wave associated with the lase used and the metallic substrate on which the analyte is placed.

The SERS effect was discovered in 1974 by Fleischmann that found out a remarkably large enhancement of the Raman scattering of pyridine in the presence of a roughened silver electrode.[28] The two principal mechanisms that contribute to this signal enhancement are:

- *Electromagnetic enhancement (EM).*
- *Chemical enhancement (CE).*

Electromagnetic enhancement

They key contributor to SERS for what concern the metallic nanostructures is the surface plasmon resonance (SPR) phenomenon. The presence of a high density of free electrons is crucial for achieving strong SPR, generating an enhanced electromagnetic field near the surface of the metal nanoparticles that amplifies both the incident excitation light and the Raman scattering light, allowing for a significant enhancement of the Raman signal. For strong SPR in the visible to near-infrared region, a high density of free electrons is essential. When light hits metal nanoparticles (NPs) that are much smaller than the incident wavelength, the free electrons experience a polarization by the external field, causing a collective oscillation. Under this conditions, Localized Surface Plasmon Resonance (LSPR) manifests when the light frequency matches the electron oscillation frequency, creating an enhanced electromagnetic field near the NP surface (Figure 15).[29]

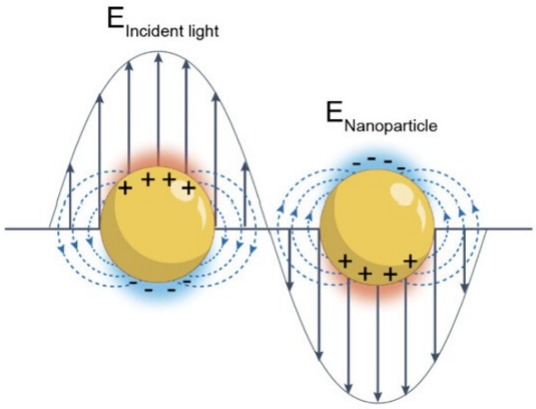

Figure 15: Localized surface plasmon resonance contributing to SERS.[30]

Considering a molecule placed at a distance *d* from a spherical nanoparticle with radius *r*, the local field E_{SP} experienced by the molecule will correspond to:

Eq.10 $$E_{SP} = \frac{\varepsilon-\varepsilon_0}{\varepsilon+2\varepsilon_0}\left(\frac{r}{r+d}\right)^3 E_0$$

Where E_0 is the electric field of the incident radiation, ε is the electric permittivity of the metal nanoparticles and ε_0 is the electric permittivity of the external environment. The closer the molecule is to the metal surface, the stronger the enhancement effect, reaching its maximum when the denominator is going to zero[30]:

Eq. 11 $$\varepsilon \approx -2\varepsilon_0$$

So, a molecule that is placed near a plasmonic system experiences a local field E_{Loc} given by the sum of E_0 and E_{SP}.

Overall, the SMEF (Single Molecule Enhanced factor) caused by the presence of a localized surface plasmon can be approximated by the equation:[31]

Eq. 12 $$SMEF\ (\omega_L, \omega_R) \approx \frac{|E_{Loc}(\omega_L)|^2}{|E_0|^2} \frac{|E_{Loc}(\omega_R)|^2}{|E_0|^2}$$

Where $E_{Loc}(\omega_L)$ represent the local electric field at the excitation frequency, and $E_{Loc}(\omega_R)$ represents the local electric field at the Raman frequency. Since the Raman shift is often quite small, it is possible to make a further approximation and assume that $\omega_L \approx \omega_R$, so the final equation becomes:

Eq. 13 $$SMEF\ (\omega_L, \omega_R) \approx \frac{|E_{Loc}(\omega_L)|^4}{|E_0|^4}$$

Chemical enhancement

On the other hand, the mechanism of *chemical enhancement* requires that the probed species strongly interacts with the SERS substrate and it is usually ascribed into three contributions: [30]

- A *resonance Raman* (RR) effect: resulting from the incident light matching an electronic transition in the molecule (contribution 10^3-10^6). This case, is strictly speaking, not about SERS as it is only about the Raman scattering of the probed molecule.
- A *charge-transfer* (CT) effect: where the incident light is resonant with a metal-molecule or molecule-metal transition (contribution 10-10^4)
- A *non-resonant chemical* (CHEM) effect: due to ground state orbital overlap between the molecule and the metal (contribution ≤ 10-100)

The chemical enhancement mechanism suggests that the interaction between the adsorbate and the metal leads to a modification of the electronic states of the adsorbed molecule or induces the creation of new states through the charge transfer between the metal and the adsorbate. The chemical mechanisms can overall amplify the signal up to a factor of 10^2-10^3, but it is strongly species-dependent, while the electromagnetic enhancement is mostly related only to the metal substrate.[32]

Enhancement factor

For certain applications, for example when detecting single molecules using SERS, it is useful to take advantage of regions where there is the maximum enhancement, as in regions where the local fields accumulated due to interferences effects (gaps, tips, edges…). Indeed it is not always effortless or reliable to find and deal selectively with these spots. For this reason, many applications usually focus

on the average enhancement factor for molecules placed randomly on the surface. As a result, most definitions of SERS enhancement factors fall into one of these two categories:[30]

- *Average EFs* which represent an average property of the substrate and can be defined as:

$$EF = \frac{I_{SERS}/N_{Surf}}{I_{RS}/N_{Vol}} \quad \text{Eq. 14}$$

Where N_{Vol} is the average number of molecules in the scattering volume for the Raman measurement, N_{Surf} is the average number of adsorbed molecules in the same scattering volume for the SERS experiment, I_{SERS} is the SERS signal intensity and I_{RS} is the Raman Scattering signal intensity.

- *Analytical EFs* that can be very useful for specific applications, but it's heavily influenced by many factors, in particular by the adsorption properties of the probe and by the concentration of the analyte. However, it is defined as it follows:

$$AEF = \frac{I_{SERS}/c_{SERS}}{I_{RS}/c_{RS}} \quad \text{Eq. 15}$$

Where c_{SERS} and c_{RS} are the concentration of the analyte on a SERS substrate and in solution. The analytical enhancement factor is particularly suitable for analyzing SERS-active liquids, like colloidal solutions, rather than film or bulk SERS substrates.[33]

Hot spots

As mentioned above, the enhancement of the SERS signal can be significantly raised when dealing with aggregates of nanoparticles. As a matter of fact, when two nanoparticles are spaced less than 5 nm apart, at the midpoint of them there is a significant amplification of the local electric field compared to when the nanoparticles are isolated.[34] The interaction between the surface plasmon resonance of the two nanoparticles creates a *hot spot*, where the electric field is amplified.

The nanoparticle's dimensions have a certain influence on the SERS enhancement factor, when two nanoparticles have a very similar size the enhancement is particularly amplified.[35] Also the shape and material of the nanoparticle is important and can give different SERS enhancements, for example not only spherical aggregates exhibit hot-spots, but also nanostars and nanorods.[36] In Figure 16 is shown a single nanoparticle and an aggregate of nanoparticles. The single nanoparticle manifests a uniform and modest EF, whilst the aggregate nanoparticles present some light blue regions, the hot spots, in which the EF is particularly high.

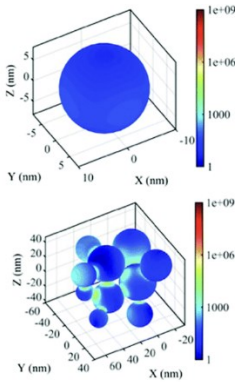

Figure 16: Representation of the EF of a single metal nanoparticle and a system of aggregated nanoparticles.[36]

2.3.3. SERS substrates and plasmonic nanostructures.

As discussed previously, the SERS technique has many advantages, above all the fact that it is possible to detect very low concentrations of material. Other benefits are the simplicity of sample manipulation and speed of analysis[37]. Nonetheless, a suitable SERS substrate is essential. It must have a roughened surface so that it can give a good enhancement as well as be reproducible and robust so that it comes to consistent results. Another characteristic that a proper substrate should have is that the surface must allow the proper absorption of the analyte. As mentioned before, SERS is a surface spectroscopy and for this reason an increase in active surface area directly correlates with an increase in the potential number of molecules contributing to SERS signal.[38]

SERS substrates can be classified into two groups:

- Metallic nanostructures fabricated on a solid substrate.
- Colloidal suspensions of plasmonic nanoparticles.

When it comes to colloidal solutions, metallic AgNPs and AuNPs are the most used, and there are two general approaches to their synthesis:

- *Top-down* methods.
- *Bottom-up* methods.

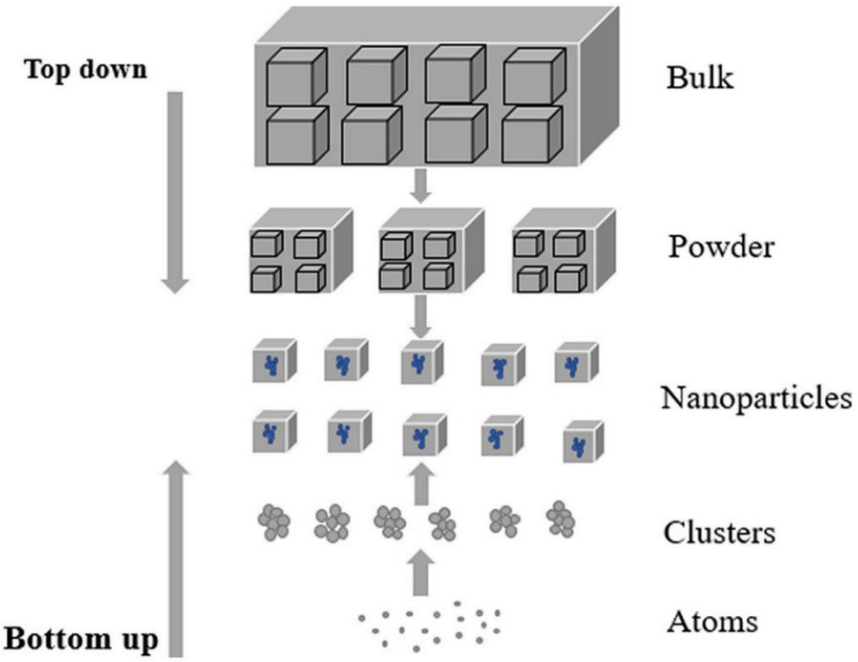

Figure 17: the top-down approach and the bottom-up approach.[39]

The ***top-down*** approach concern the production of nanoparticles starting from the bulk material as shown in Figure 17.[39] Even though top-down approaches are simple to use, it is difficult to obtain arbitrary particle size and shape. One of the most used top-down technique to produce AuNPs is the ***Laser Ablation Synthesis in Solution*** (LASiS). The ablation mechanism can be divided into several processes.[40] After passing through the solvent, the pulsed laser impacts the surface of the target resulting in the absorption of incoming photons that causes the heating of the irradiated area. Subsequently, some material can be removed from the target in form of vapors, liquid droplets, solid fragments, or as an expanding plasma plume. There are some factors that can influence the nanoparticle's characteristics such as fluency, repetition rate, pulse duration and light adsorption efficiency of the target material[39]. For this technique it is possible to use both organic and aqueous solvents. In an aqueous solvent, thanks to the excitation caused by the laser, it is possible to create superficial oxygen bridges. Ions like OH^- and Cl^- (Fig. 18), present in the aqueous environment, can open these bridges generating negative surface charges so that it is not necessary the addition of stabilizers to produce stable nanoparticles.[41]

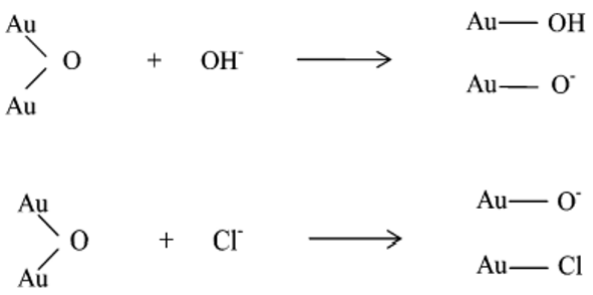

Figure 18: Creation of superficial oxygen bridges by OH^- and Cl^-.[41]

On the other hand, bottom-up methods involve synthesizing nanoparticles from smaller components like ions and molecules. The synthesis usually needs the reduction of a gold salt in the presence of a stabilizing agent to prevent an excessive growth of the formed nuclei, so that it is possible to obtain nanoparticles with a reduced size and a low polydispersity.

2.4 Innovative spectroelectrochemical methods for detecting hexavalent chromium.

Spectroelectrochemistry is a hybrid approach that combines the benefits of both electrochemical and spectroscopic techniques. Electron or photons can be used to trigger chemical transformation while the acquisition of both electrochemical and optical data offers a complete overview of the changes taking places on the electrode surface.

2.4.1. EC-SERS for detecting hexavalent chromium.

Raman-Spectroelectrochemistry is a highly promising technique because it provides unique fingerprint properties for identifying substances. Therefore, the identification and differentiation of the species is allowed. Surface-enhanced Raman spectroscopy (SERS) is more advantageous compared to normal Raman spectroscopy because of its greatly increased Raman signal and significantly reduced fluorescence. A system that combines SERS spectroscopy and electrochemistry is the *Electrochemical surface-enhanced Raman spectroscopy* (EC-SERS) where an electric potential is applied to the nanostructured working electrode in the presence of an electrolyte.[42] The goal to reach is to detect hexavalent chromium, that as said before is highly toxic, combining the electrochemical techniques and the SERS one.

This part of the thesis is inspired by the work of on the article Korshoj at al.[43], but Nile Blue, instead of methylene blue, is used to detect Cr (VI), . In the referred article, the signaling mechanism is based on the electrocatalytic reaction between Cr(VI) and surface-immobilized methylene blue (MB). What they do is to first reduce the MB at the electrode to form the leucomethylene blue (LMB)

that is the reduced form of methylene blue. Thus LMB is capable to catalyze the reduction of Cr(VI) to form Cr(III) and regenerate MB as shown in Figure 19.

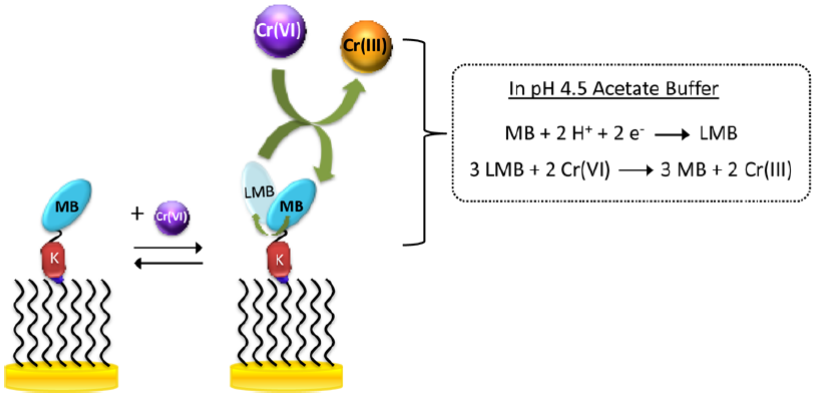

Figure 19: Design and signaling mechanism of the E-ION sensor for detection of Cr(VI).[43]

In this thesis is used Nile Blue instead of Methylene Blue, but the concept is almost the same. The point is to electrochemically reduce the Nile Blue (NB) that is anchored onto the electrode surface through a chronoamperometry. The potential at which the reduction occurs can be seen from a cyclic voltammetry. The reductive form of the Nile Blue should be able to catalyze the reduction of Cr(VI) to Cr(III) and regenerate the oxidative form of Nile Blue. The molecular form of reduction and oxidation of the Nile Blue is tracked by the SERS spectra and from the cyclic voltammetry. The implementation of an EC-SERS approach introduces novelty in respect to the work of Korshoj at al., that is indeed expected to provide a more complete description of the overall system.

2.5 Fabrication of thin films for microelectronics and SERS substrates.

Thin films are generally produced to provide special properties like electrical, optical, mechanical, and chemical to a background substrate, so that it is easy to satisfy the needs for a specific application on an inert substrate with minimal macroscopic perturbation in shape and composition. Those properties are defined by the resulting structure, which deeply relies on the chosen deposition method, film material, and substrate. There are many deposition techniques for example the Physical deposition method (PVD), vacuum evaporation, sputtering, laser ablation, Chemical deposition method (CVD)[44] and also spraycoating and inkjet printing. Another deposition method is ***drop-casting***. In this method, a drop of liquid containing a suspension of the particle is initially placed on the surface of the electrode intended for modification. [45]

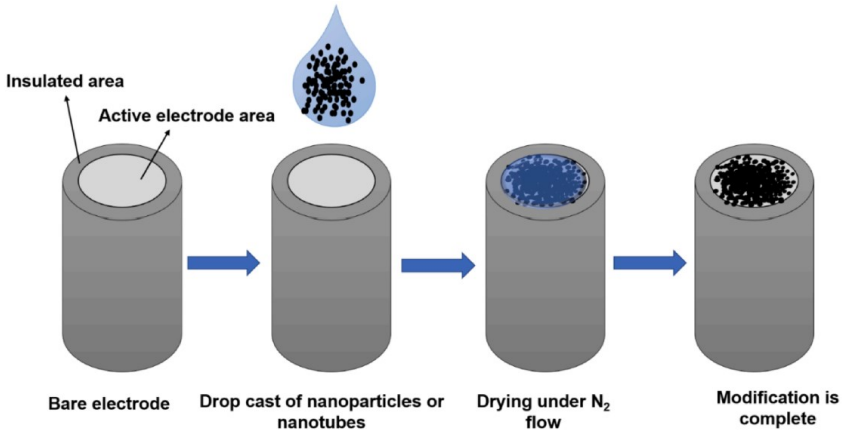

Figure 20: A schematic showing of the drop-casting technique.[45]

. Since the resulting microstructure defines the physical and chemical properties of the substrate, it is essential to carefully manage the deposition parameters, such as the substrate temperature, deposition rate and pressure. Finally, the microstructure can be amorphous, polycrystalline, or epitaxial.

Among the various properties that thin films can possess, the one of greatest interest on this work is the electrical conductivity and effectiveness as SERS substrate. A significant factor that influences the conductivity deviation in thin films compared to the bulk material, is the size effect. As a matter of fact as the material thickness decreases, the electron mean free path decreases due to the activation of additional scattering mechanism, leading to a reduction in conductivity. Microstructural defects like voids, dangling bonds, and localized defects also can decrease the conductivity.

2.5.1 Inkjet printing

This drop deposition technique is used in dozens of applications such as solar cell, fuel cells, batteries, printing polymers and ultimately also for the fabrication of thin films for chemical detection.[46] This technique involves ejecting precise amounts of ink from a chamber through a nozzle. These ink droplets fall on the substrate and form a patterned layer. After, an annealing process is required to evaporate the ink solvents, leaving a solid layer on the substrate. There are many techniques for droplet generation, but the two most used are:[47]

- Continuous inkjet (CIJ): where the flow is continuous, resulting in a steady stream of droplets. (Fig. 21a)
- Drop-on-demand (DOD): where ink is emitted through the nozzle to create a short jet, which then condenses into a drop only when it is needed for printing (Fig. 21b).

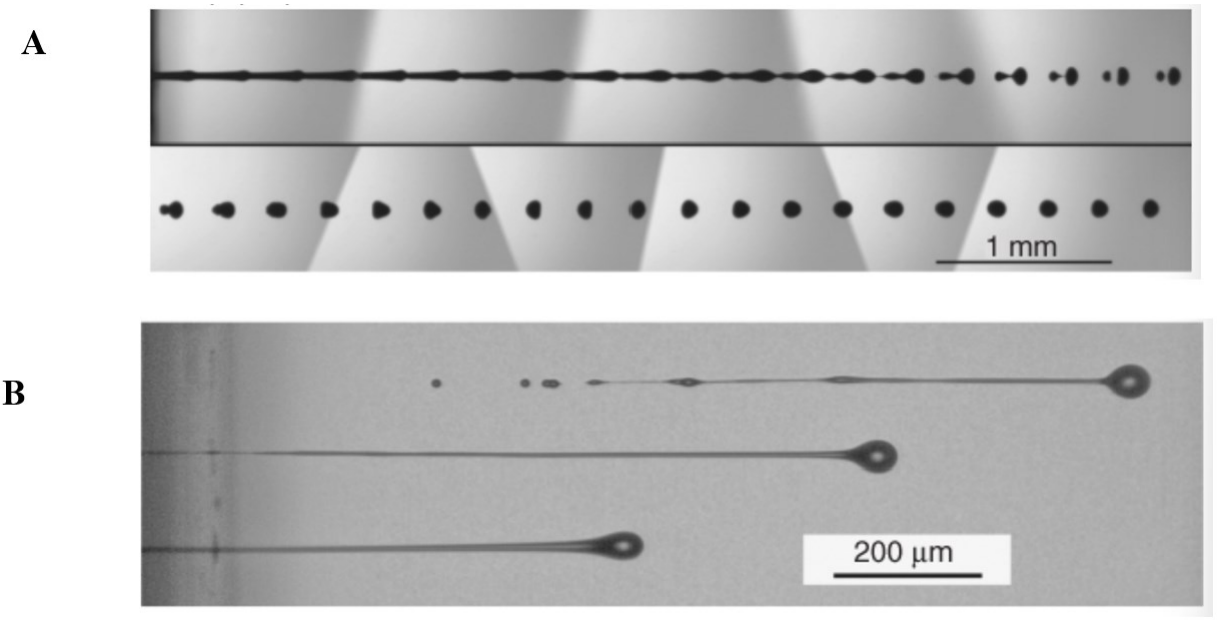

Figure 21: images of liquid jets moving from left to right, in Figure 18a is showed the CIJ, while in Figure 18b the DOD.[47]

In addition to CIJ and DOD, there are other inkjet printing technologies as reported in Figure 22:

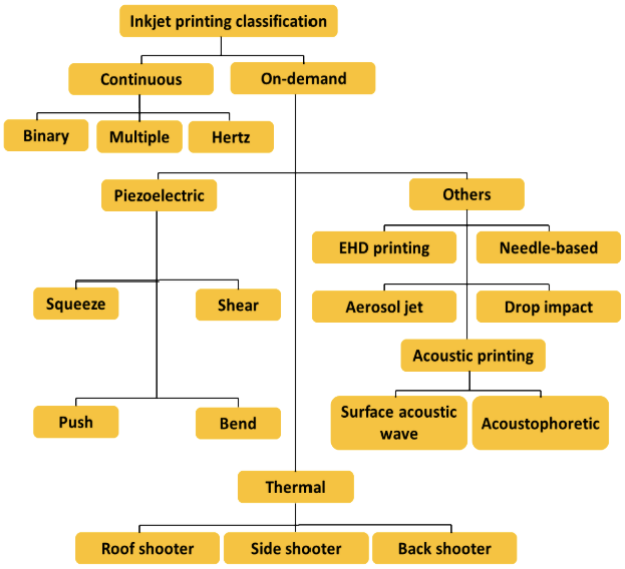

Figure 22: Classification of inkjet technologies.[48]

Among them, the piezoelectric inkjet printer is also commonly used. In a PIP (Piezoelectric Inkjet Printer), the piezoelectric transducer alters its shape when a voltage is applied. This change produces a pressure pulse within the ink chamber, causing an ink droplet to be expelled from the nozzle attached to the chamber. This kind of inkjet printer can operate in various mode, in this case the bend mode.[48]

The components of the experimental setup for this technique, represented in Figure 23a, are:

- Ink chamber.
- Printer cartridge.
- Fluid transport system from the chamber to the cartridge.
- Substrate holder.
- Alignment chamber between the substrate and the cartridge.

The cartridge is particularly important as it controls the formation and ejection of ink droplets. It must be made of a material that can withstand a wide range of solvents. The cartridge is characterized by the number of nozzles, built to expel a specific droplet volume.

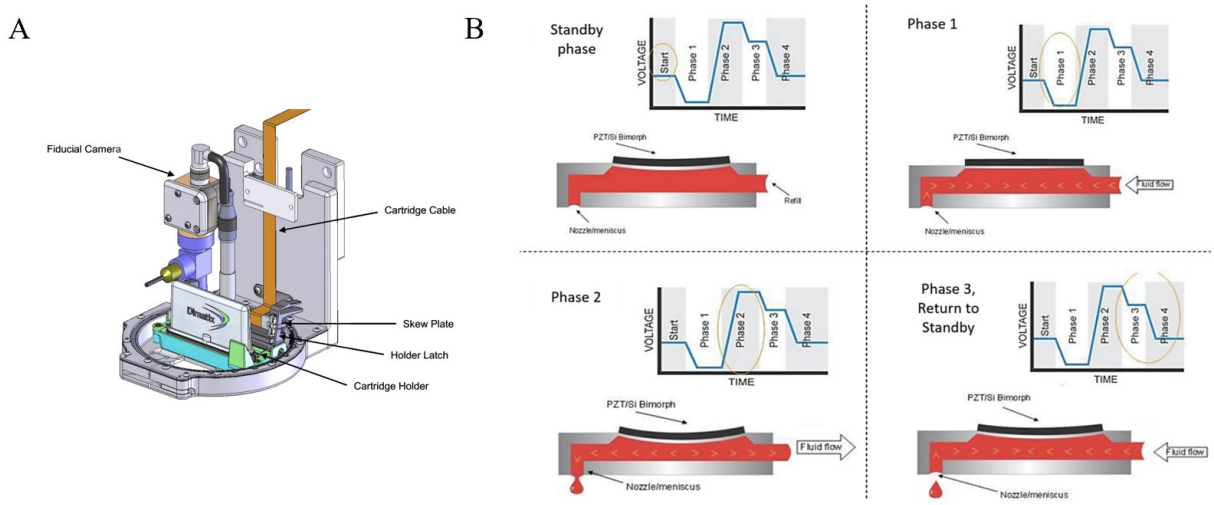

Figure 23: A) Representation of all the components that enable the operation of the cartridge in inkjet printing technique. B) Schematic representation of the operation of piezoelectric actuators during the printing process. Start: initial situation where the actuator is not deformed; Phase 1: voltage decrease allowing ink entry into the cartridge chamber; Phase 2: rapid voltage increase causing ink ejection from the chamber and droplet formation; Phase 3 voltage decrease causing droplet ejection and deposition.[49]

The system enabling droplet formation inside the cartridge is governed by piezoelectric actuators. These actuators can deform mechanically in response to applied voltage, thereby regulating the amount of ink entering the cartridge and the ejection of droplets. The voltage applied to the piezoelectric material over the deposition time (waveform) is a critical parameter to manage for achieving uniform printing. Specifically, the waveform is divided into four phases reported in Figure 23b above.[49]

The choice of the appropriate waveform to use during the printing process depends on the physical characteristics of the ink. Specially, three fundamental parameters are used to characterize the ink:

- Surface tension. (γ)
- Dynamic viscosity. (η)
- Density of the fluid. (ρ)

From these quantities, an experimental parameter Z has been identified to indicate the suitability of a particular liquid for inkjet printing. It also considers the diameter of the nozzle used α and is defined as the inverse of the Ohnesorge number Oh.

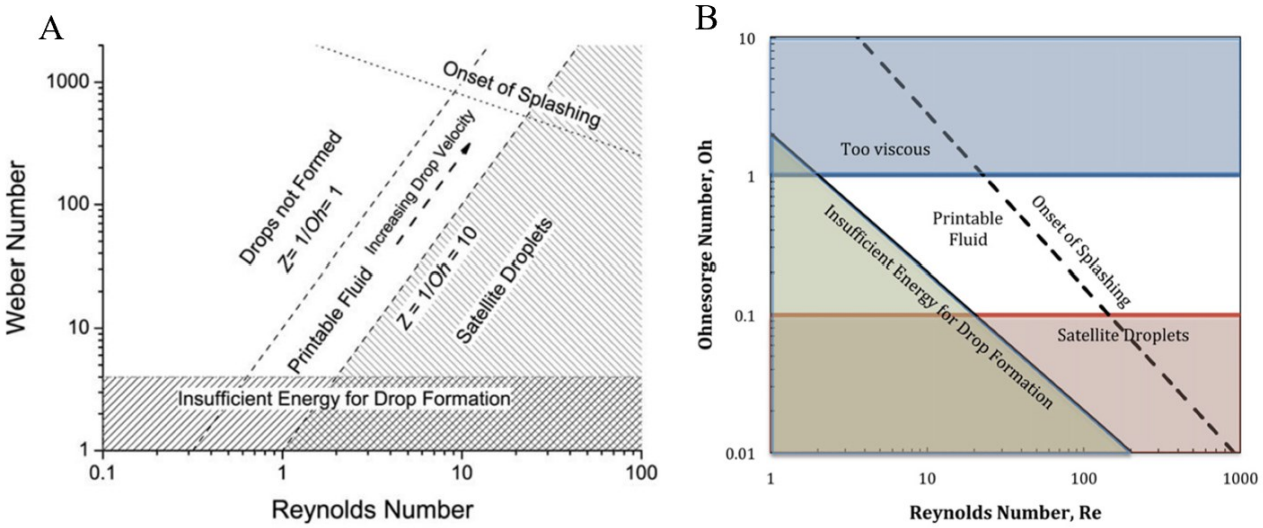

Figure 24: Operating regimes of inkjet printing in the control parameter space of A) Weber number We vs Reynolds number Re, and B) Ohnesorge number Oh versus Reynolds number Re.[50]

As reported in Figure 24a, the suitable range for generating stable droplets is $10 > Z > 1$, while when $Z < 1$ viscous dissipation prevents droplets from ejection. Contrarily for $Z > 10$, ink is expelled smoothly from the nozzle, but the droplet possesses too much kinetic energy, leading to satellite droplets.[50] The printability of a fluid can be assessed by its Onhesorge number as shown in Figure 24b, but there are other factors influencing droplet formation, such as the fluid-air surface tension barrier at the nozzle. Indeed, to eject the droplet, a minimum ejection velocity must be attained to overcome this barrier. This minimum velocity is given by:

Eq. 16
$$v_{min} = \left(\frac{4\gamma}{\rho\alpha}\right)^{1/2}$$

The ink and printing specifications required for this work are given in the further section "Material and methods".

2.5.2 Spray Coating

Spray Coating is a liquid phase deposition technique, where the substrate is treated by an aerosol flow of the solution to be deposited. There are two general spray coating techniques:

- *Single-pass technique*: the nozzle moves across the substrate just once. Full surface coverage is achieved efficiently with high deposition rates, as droplets merge.
- *Multiple-pass technique*: the nozzle makes multiple passes over the substrate. The layer is formed by several groups of droplets that evaporate independently of each other.

The parameters that control the morphology of the film are diverse, like:

- Air pressure.
- Solution viscosity.
- Solvent properties.
- Nozzle tip geometry.
- Distance between needle and substrate.

In general, the spray coating technique offers several advantages. It allows for the modulation of film thickness, is possible to cover large surfaces, and this method is not influenced by the type of substrate onto which the metal is deposited. The only drawback is the potential production of irregular films. Therefore, it is crucial to control the parameters carefully.

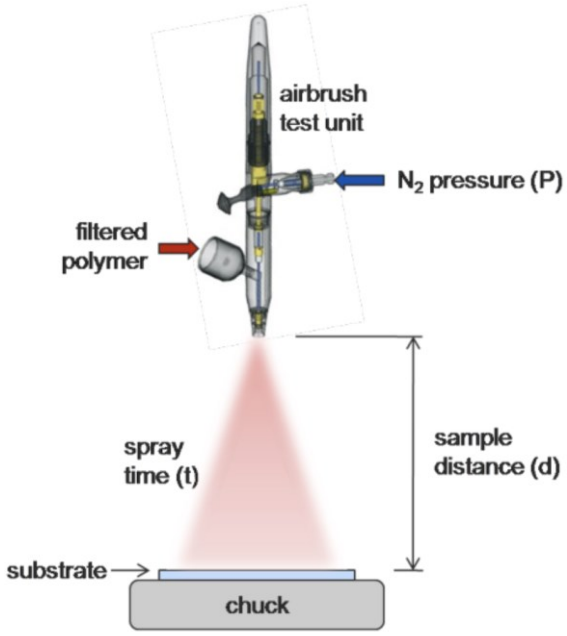

Figure 25: Illustration of the implemented airbrush coating system.[53]

In this work, the *airbrush spray deposition* is used. In several articles, has been demonstrated that this technique is very simple and rewarding, and that is capable of producing devices comparable to those prepared with other techniques like spin coating[51]. Spin-coating is one of the most used methods, but despite the simplicity and effectiveness of this technique in producing high quality thin films, it lacks several aspects necessary for large-scale production.[52] One promising deposition technique is ***spray-coating*** that can operate at high production speeds and is adaptable to various substrates because the droplets sprayed from the nozzle are transferred to the substrate without direct contact with its surface. Furthermore, the spray process enables the patterning of coated films on a sub-millimeter scale using shadow masks. Additionally, it can accommodate much more dilute solutions compared to the spin-coating method.[53]

The greatest advantage of using an airbrush is that is possible to use small amount of materials in dilute solution, in contrast, for example, in the case of inkjet printing where highly concentrated inks are needed. Moreover, it is possible to cover large-area deposition of controlled device thickness and can be performed under ambient conditions.

3. Materials and methods

3.1 Material and instruments

All the compounds used for the different solutions that were prepared in milli-q water. It was used 1,5-diphenylcarbazide ($C_{13}H_{14}N_4O$) (CAS 140-22-7) , Chromium(VI) oxide (CrO_3) (CAS 1833-82-0), Potassium Ferrocyanide ($K_3[Fe(III)CN_6]$) (CAS 13746-66-2), Sulfuric Acid (H_2SO_4) (CAS 766-93-9), PEG-SH 5000 units (CAS 134874-49-0), Sodium Phosphate ($NaH_2PO_4 \cdot H_2O$) (CAS 10049-21-5), Dibasic Sodium Phosphate (Na_2HPO_4) (CAS 7558-79-4), Sodium Chloride (NaCl) (CAS 7647-14-5), Ethylene Glycol (CAS 107-21-1), Tween 20 (CAS 9005-64-5), Nile Blue A functionalized with lipoic acid (LipNB), 6-mercapto-1-hexanol (C_6OH) (CAS 1633-78-9). All the reagents were purchased from Merck, except for LipNB that was synthesized in a previous work.[54]

The instruments used in this work are:

- *Raman spectrometer*.
- *UV-Vis-NIR Spectrometer*.
- *Potentiostat*.
- *Inkjet printer*.
- *3D printer*.
- *Spray coating airbrush*.

Raman Spectrometer.

The instrument used to record Raman and SERS spectra is an InVia model by Renishaw, featuring three laser sources with varying wavelengths:

- An Argon laser emitting radiation at 488 and 514 nm.
- A He-Ne laser emitting at 633 nm.
- A diode emitting laser radiation at 785 nm.

The instrument is equipped with a Leica DM-LM confocal optical microscope, and includes Leica objectives of 5x, 20x, 50x, 100x and a long focal length 20x objective from Olympus.

The laser beam is attenuated by filters of varying optical densities and, after passing through a series of entrance mirrors, encounters a beam expander, transforming the radiation from a point source to parallel rays of 6mm diameter. The beam then traverses a beam splitter, directing in onto the sample through the microscope. The scattered light passes through an edge filter, removing elastic scattering, with a cut-off capability of approximately 80 cm^{-1}. The inelastic component then reaches a diffraction grating with 1200 or1800 lines/mm, before passing through a lens and a slit, and finally reaching the detector, a 400-pixel CCD (Charge-Coupled Device). All the process[55] is showed in Figure 26:

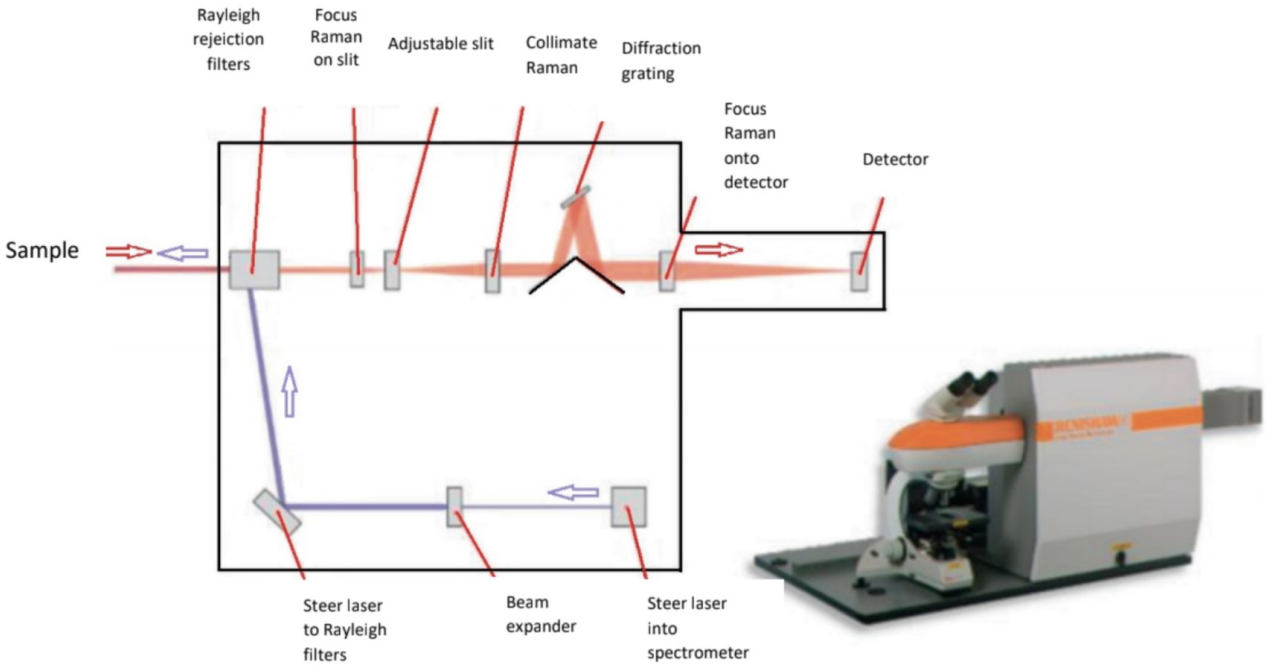

Figure 26: schematic representation of Raman instrument where violet arrows describe the path of the laser source while the red ones indicate the path of the scattered light.[54]

The CCD camera is constructed using a silicon diode array with a sequence of pixels, each measuring $22\mu m \times 22\mu m$ in dimension. Every pixel is responsible for capturing photons at a particular wavelength and utilizes the photoelectric effect to produce an electronic signal. Moreover, the CCD camera is equipped with air cooling for temperature regulation.

UV-Vis-NIR Spectrophotometer.

For the characterization of the gold nanoparticles the Agilent Technologies Cary 5000 spectrophotometer was utilized. The technique is based on the principle of passing light at a known wavelength through a sample and recording the amount of light that has been absorbed. This is achieved by comparing the intensity of the incident light to the intensity of the transmitted light.

As shown in Figure 27 the light source is directed onto a dispersion device via a slit, where the dispersed light interacts with the sample. The light transmitted through the sample is then gathered by a detector[56].

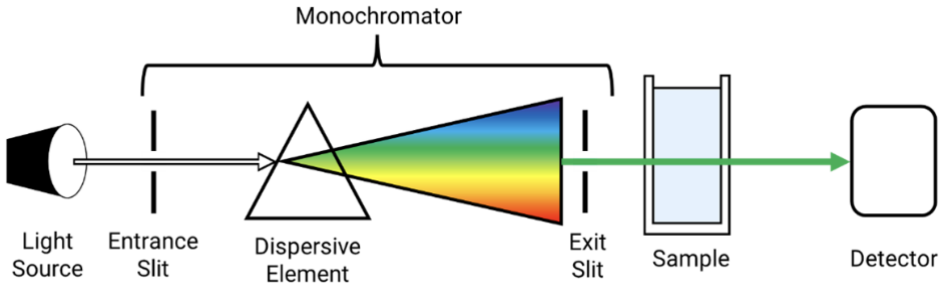

Figure 27: A basic block diagram of the elements in a single beam UV-Visible spectrometer.[55]

Potentiostat.

The electrochemical measurements were performed with a 660D model potentiostat by CH Instruments. This particular model combines several functionalities into one unit, making it suitable for various electrochemical techniques including sweep techniques, step techniques, stripping techniques, controlled-current techniques and amperometric detection techniques.Also it has a potential control range of ±10 V and a current range of ±250 mA and it has a very high sensitivity, in fact is capable to measure currents down to tens of picoamperes ensuring that even subtle electrochemical processes can be detected and analyzed. Another interesting feature is that the instrument supports the simultaneous recording od electrochemical data and external signals, such as spectroscopy signals. This capability facilitates comprehensive experimental analysis by allowing researchers to correlate electrochemical measurements with other experimental parameters.

The inkjet and resin printer will be discussed in detail in chapter 3.4.1 and 3.5.1 respectively.

3.2 AuNPs synthesis.

The gold nanoparticles (AuNPs) are prepared via Laser Ablation Synthesis in Solution technique (LASiS). A gold target is immersed in an aqueous solution with NaCl 50 µM onto which the laser (Nd: YAG, 1064 nm, approximately 1 J/cm^2, pulses form 9 ns to 20 Hz) will be focused. The ablation process will be terminated when a nanomolar concentration of gold nanoparticles is reached. This concentration value is determined by measuring the UV-Vis absorbance during ablation.

3.3 Preparation of Cr(DPCO) complex

A solution of Cr(DPCO) is prepared as follows:

Initially it is necessary to prepare the DPC solution in ethanol. The Cr(VI) solution was prepared by melting the CrO_3 in MilliQ water. The resulting stock solution is therefore at a concentration of 10^{-3} M and is composed of 300 µL of DPC, 200 µL of Cr(VI), and 250 µL of H_2SO_4.

3.4 Sensor preparation techniques.

3.4.1 Inkjet printing

For printing the substrates, the Dimatix Materials DMP-2831 inkjet printer, manufactured by Fujifilm, was used. The cartridge used was DMC-11610 (10 pL). The printer management software utilized was Drop Manager.

Ink formulation

Once the gold nanoparticles have been prepared through ablation, the following steps are followed:

1. Functionalization of nanoparticles with PEG-SH.
2. Concentration of nanoparticles.
3. Ink preparation.

Functionalization of nanoparticles with PEG-SH

A solution of 0.7 mg/ml of PEG-SH (5000 Da) is prepared in water, and then 12 ml of this solution is deposited into the 270 ml AuNPs batch. The solution should be left under agitation overnight before being centrifuged. The quantity of PEG-SH is calculated based on the concentration of ablated AuNPs (obtained from the UV-Vis spectrum using the published procedure[57]), in such a way as to have a sufficient amount to fully functionalize the particles, since each particle is capable of binding several hundred molecules of PEG-SH.

Nanoparticle concentration

To concentrate the nanoparticles, 24 Eppendorf tubes must be filled with 1 ml of AuNP-PEG solution and then multiple centrifugation cycles are performed:

1. Centrifuge the solution for 30 minutes at 3000 rcf, and then discard the supernatant and set it aside.
2. Refill the Eppendorf tubes with the AuNP-PEG solution to further concentrate the particles and centrifuge again at 3000 rcf for 30 minutes, then discard the supernatant and combine it with the previous one. This step must be performed twice.
3. Once all the supernatants are collected centrifuge for 30 minutes at 5000 rcf.

4. Combine all the precipitates.

To determine the concentration of the precipitate and the extent of aggregation, a UV-Vis spectrum of the diluted ink product must be obtained, followed by spectrum fitting using the above-mentioned procedure. For optimal printing, a concentration of at least 50 nM is required.

Ink preparation

For a volume of approximately 0.5 ml of concentrated particles, it is necessary to add 10% ethylene glycol and 20-30 µL of 1 mM Tween 20. Then, it is recommended to filter the ink, with a 0.44 µM cutoff, before proceeding with printing.

Cartridge Care

Before proceeding with printing, it is necessary to perform a cleaning cycle. The cartridge tank must be filled with IPA and then attached to the printhead. It is very important to remove all air bubbles that may for in the channel. Then, some air must be blown to verify that IPA comes out from the nozzles. After that the cartridge must be positioned on the printer and it is necessary to choose the correct waveform, in this case the cleaning waveform. The vacuum must be activated and then selected the desired pattern to print.

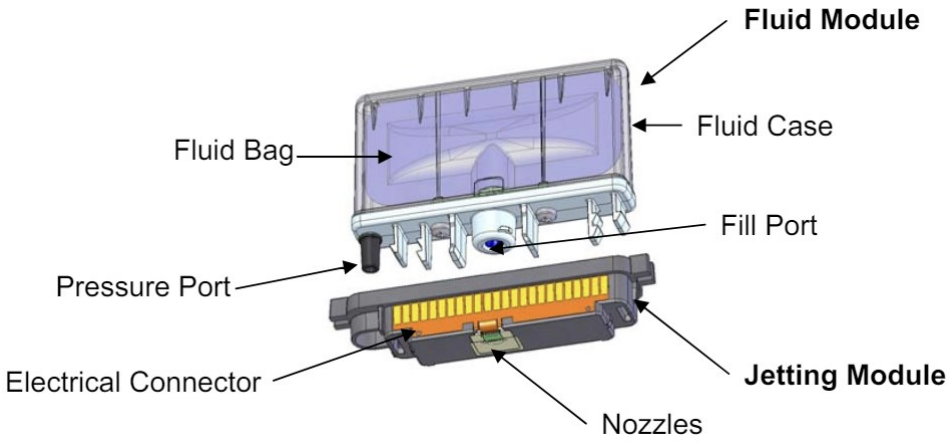

Figure 28: a representation of the cartridge components.

Printing

Once the cleaning is finished, one can proceed printing. The previous cartridge is removed, and a new cartridge tank is this time filled with ink ensuring that both the tank and the channel are full and that there are not air bubbles that could prevent a good printing.

Figure 29: a schematic representation explaining how to fill a cartridge. (from left to right)

When the cartridge is settled on the printer, it is important to observe how the ink is expelled from the nozzle using the drop watcher function. For a good print it is necessary that the ink droplet expelled from the nozzle is straight and symmetrical as shown in Figure 30. In case the nozzle does not expel ink properly, the waveform (namely a program of pulses used to manage the piezoelectric membranes for ink expulsion) must be adjusted. After that, the sensor can be positioned on the printer plate and the vacuum can be activate. The last thing to do before start printing is to position the start of the sensor with the fiducial camera.

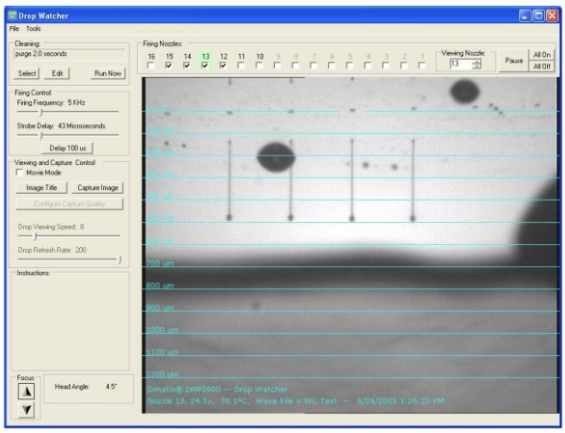

Figure 30: Drop watcher function, the droplets expelled from the selected nozzles are straight and symmetrical.

After printing is finished, is important to immediately disassemble the printhead and perform the IPA cleaning cycle again. Meanwhile, the ink-containing tank must be washed with aqua regia and then rinsed with water and finally IPA to prevent aggregates from forming inside.

3.4.2 Spraycoating

The spraycoating technique was realized with the Double Action Airbrush BEL-AIR004 by Belkits.com shown in Figure 31.

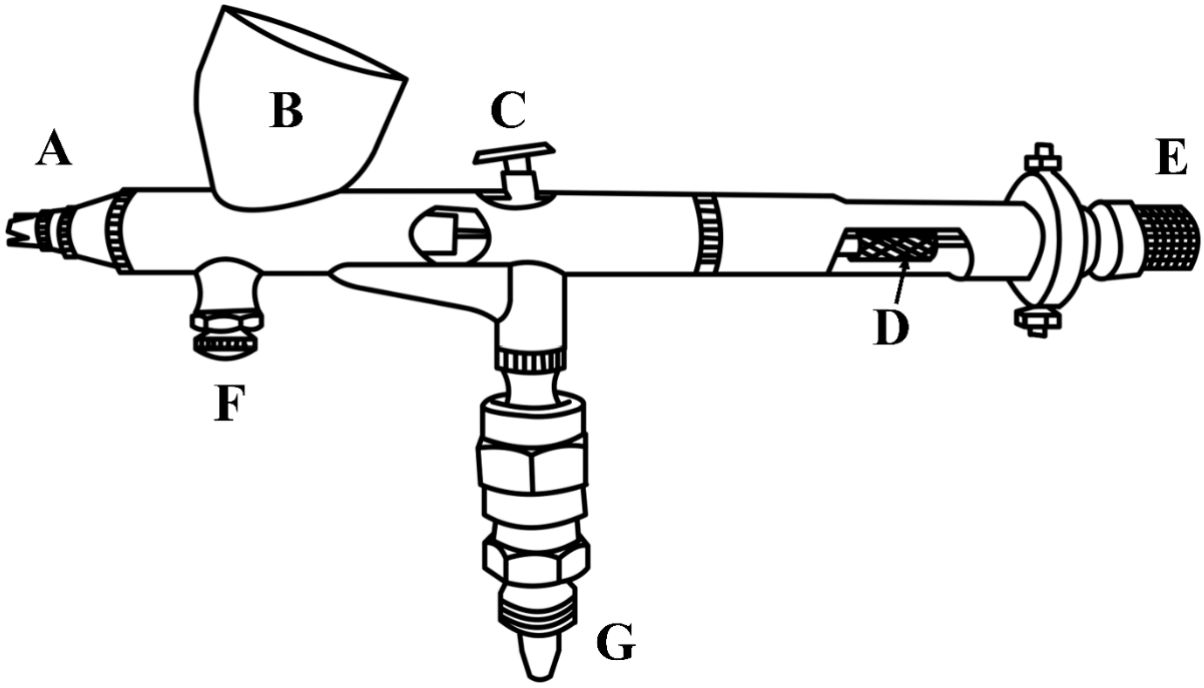

Figure 31: Representation of the Airbrush. A is the nozzle group, B the reservoir, C the ink trigger, D the needle lock ring, E the ink flow adjustment ring, F the N_2 flow adjustment ring and G the N_2 flow inlet.

When using the airbrush is important to clean it carefully before every use. There are 3 steps to follow:

1. Load approximately 1 ml of isopropyl alcohol (IPA) into the reservoir and perform the spray coating procedure. This guarantees an initial cleanse of the device, preventing the formation of bulky nanoparticle aggregates that are challenging to remove.
2. Ensure that the spray-coater is disconnected from the nitrogen flow, that the reservoir is empty, and that the ink flow adjustment ring (E) is completely unscrewed.
3. It is now important to separate every airbrush component and clean them with optical paper and IPA, and after that the airbrush can be reassembled.

Once the airbrush is cleaned and reassembled is ready to spray-coat.

To obtain thin, homogeneous, and effective plasmonic films for SERS measurements is important to follow some exact parameters during the spray-coating procedure. The *distance* of the device from the substrate must be 20 cm, the *nitrogen pressure* of 3.0 bar and the *plate temperature* over to 120°C. The *sprayed volume* depends on the desired transparency/thickness of the film and on the substrates

size, and usually goes from 5 to 20 mL. Regardless of the volume used, the substrates must exhibit sufficient conductivity. Moreover, the trigger (C) must be held in the open position by securing a rubber band from the trigger itself to the copper ring near the ink flow adjustment ring (E). The latter should be opened only to the extent necessary to prevent droplets from forming on the substrate during spraying, usually requiring half gear revolutions. The last parameter to check is the *nitrogen adjustment ring* (F) setting that should be opened all the way.

3.5 Construction of the spectroelectrochemical cell.

The electrochemical cell is 3D printed using a photo-polymerizable acrylic-based acrylic resin on a Formlab 3D printer. For this purpose, a cell is constructed where substrates and electrodes are inserted, and the cavity is filled with buffer solution. This is then covered by a cover slip to prevent the formation of meniscus, which would hinder laser focusing.

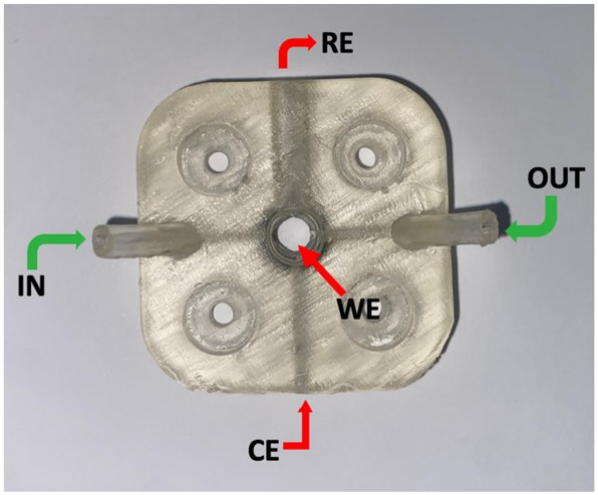

Figure 32: Photo of the printed spectroelectrochemical cell.

3.5.1 Resin Printer.

Resin printers include a range of printers in which the most common processes are *stereolithography* (SLA) and *digital light processing* (DLP). Resin 3D printers are ideal for creating high-precision parts and prototypes, especially compared to objects made with fused filament fabrication technology. Furthermore, resin-printed items are isotropic, waterproof, and have a smooth surface finish. In both SLA and DLP a liquid resin is selectively exposed to a light source: a laser in SLA technology and a light display in the DLP one. The resin has the characteristic of being photosensitive, it is a photopolymer and therefore undergoes chemical and physical changes when exposed to a light source. In the case of resin for 3D printers, this polymer hardens upon exposure to light. During the

printing process, the exposure forms very thin solid layers, which overlap to create a single solid object.

The 3D resin printer used in this project works through the top-down technique, in which the resin lies on top of a movable build platform as shown in Figure 33.

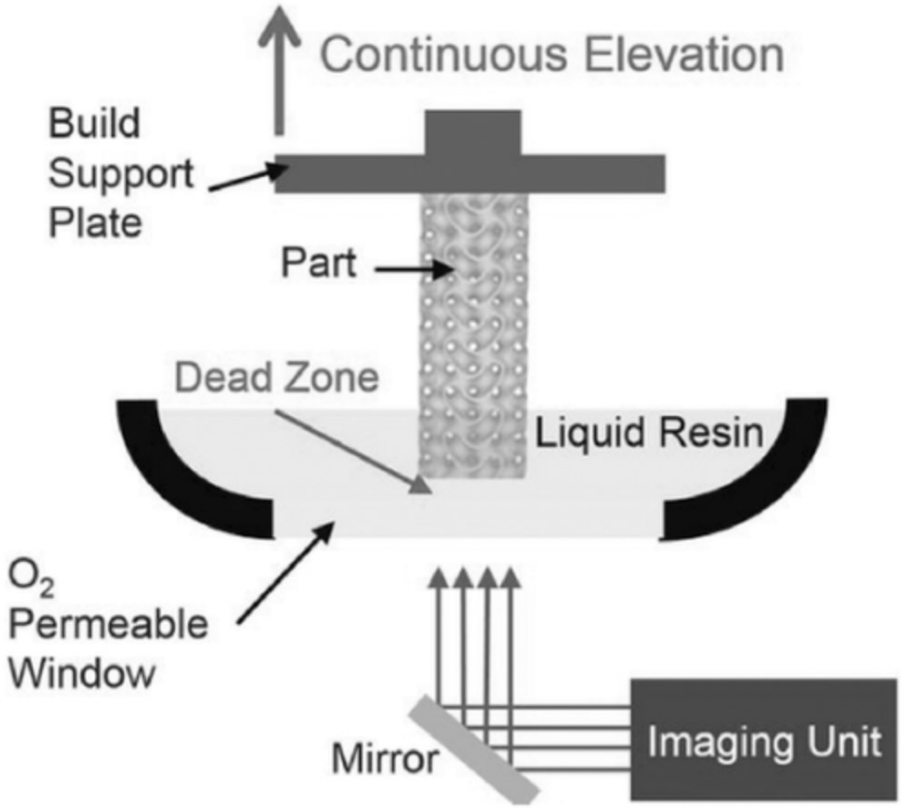

Figure 33: representation of the top-down technique in the 3D resin printer.[57]

The top-down approach utilizes a laser scanning from the bottom of the reservoir. The building platform is placed near the reservoir's bottom, with only a thin layer of liquid resin beneath it. This layer gets exposed to the laser for photoactivation, then the platform rises, allowing the liquid resin to fill the space between it and the reservoir.[58] The top-down approach offers several advantages like:

- Safe to use because the laser is confined within the printing device.
- The curing process occurs in a sealed environment, preventing oxygen interference during photopolymerization.
- No need for roller-based liquid resin recoating since refilling happens automatically with the aid of gravity.
- Generation of smoother printed parts due to the full contact between the liquid resin and the smooth bottom surface of the reservoir.

The spectroelectrochemical cell model printed with the resin 3D printer is shown in Figure 32.

In this cell the substrate and the electrodes are inserted inside, and the cavity is then filled with the buffer solution (details provided in the next chapter below). The cavity is then covered by a glass coverslip to prevent the formation of a meniscus, which hinders laser focusing. The cell features two channels of approximately 1 mm in diameter for the inlet and outlet of solutions, and a chamber with a 4 mm diameter and 5 mm height.

3.5.2 Electrodes preparation, buffer solution, Cr (VI) solutions.

Electrodes preparation

A silver wire in a saturated KCl was used as reference electrode (RE). It is separated from the solution by a septum. Reference electrodes like this are called pseudo reference electrode. A platinum wire served as the counter electrode (CE). The working electrode (WE) is the substrate of gold nanoparticles deposited by spray coating on a glass surface, details on the electrode preparation will be provided in chapter 4.1.2. Conductive copper tape was used at the edges of the sensor to enable the electrical connection to the potentiostat.

To functionalize the working electrode, the following procedure is followed: first 40 µL of Nile Blue thiolate 10^{-4}M are diluted in 6 mL of Methanol, then the sensor is dipped in the solution under agitation for one day. The day after the sensor is rinsed with deionized water and the success of the functionalization is verified through a Raman analysis. Therefore, a spectrum is acquired through a 10 second extended acquisition, with a Raman Shift ranging from 200 cm^{-1} to 2000 cm^{-1}, using a 785-line laser with a laser power of 0.06mW.

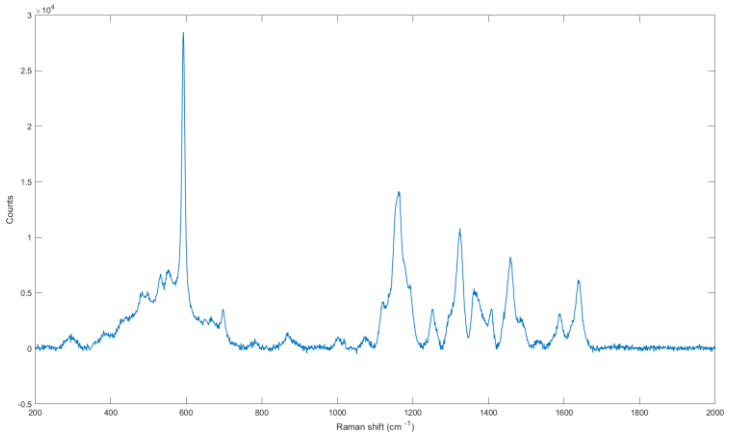

Figure 34: Raman spectrum of the functionalized sensor. The sensor was produced via spraycoating.

The characteristic peak of Nile Blue at 591 cm^{-1} is observed, indicating that the sensor is successfully functionalized.

Buffer and Cr (VI) solutions

The phosphate buffer 0.1 M at pH 5 is used as the buffer and electrolyte solution. Then the Cr(VI) solutions were prepared by diluting a 10^{-3} M stock water solution of $NaCrO_4$ as: 0 µM, 0.01 µM, 0.05 µM, 0.1 µM, 0.5 µM, 1 µM, 5 µM and 10 µM.

3.5.3 Procedure for measurement using the spectroelectrochemical cell.

To assemble the spectroelectrochemical cell, several steps are needed to be followed. First, place the working electrode beneath the O-ring, then gently close the cell with the screws without tightening too much to avoid breaking the substrate. Finally, insert the reference and counter electrodes and cover the cavity with the glass cover slip. A silicon-based glue is used to seal all components.

The complete measurement used to detect hexavalent chromium combines electrochemistry and Raman spectroscopy. The cell is filled with the buffer solution and connected to the potentiostat, following the order of reference, counter and working electrodes, then positioned under the Raman microscope. Initially, an extended spectrum from 200 to 2000 cm^{-1} Raman shift is acquired to verify the correct functionalization of the sensor. Subsequently, continuous spectra acquisition (lasting 1 second per spectrum) is performed throughout the duration of the test to monitor changes in Nile Blue on the sensor. After one minute, a chronoamperometry at the reduction potential of hexavalent chromium is set at -0.39 V vs Fe(III)/Fe(II) (100 mV more negative of the reduction peak at -0.29 V) and left for one minute. After the minute, there is a two-minute pause followed by setting a chronoamperometry at the first reduction potential of Nile Blue at -0.49 V for one minute, followed by another 2-minute pause. Finally, a last chronoamperometry at the second reduction potential of Nile Blue at -0.66 V is performed for another minute. At the end of the test, the continuous Raman spectrum acquisition is stopped, and the cell is filled with the next hexavalent chromium solution to repeat the procedure.

4. Results and Discussion

4.1 Substrates

Surfaces play a fundamental role both on electrochemistry (as electrodes) as well as in Surface Enhanced Raman Spectroscopy. Hence, few approaches were evaluated along this thesis work to establish the most suitable technique for robust substrate fabrication with high performance. Three methods were adopted hereafter, all of them have in common the nature of the starting material, namely a colloidal dispersion of Au nanospheres obtained by Laser Ablation. These are further used *as it is* in case of films obtained by *drop casting* and by *spray coating*, while further formulated with additives when used as ink for the *inkjet printer*. All of them use common glass slides as substrate. The procedure, and the results obtained by *inkjet printing* and *spray coating* will be discussed in detail in the following.

4.1.1 Sensors printed via inkjet printing.

To print the sensor using inkjet printing technique, it is necessary to add ethylene glycol to the ink in an amount corresponding to 10% of the total ink volume and 5% of 1mM TWEEN 20. Ethylene glycol is added to increase the viscosity of the ink to ensure it is sufficiently viscous for good printing, while TWEEN 20 is a non-ionic surfactant that helps to keep the nanoparticles dispersed and prevent their aggregation. Following the procedure described in Chapter 3.4.1, approximately 0.5 ml of ink is obtained, to which 50 µL of ethylene glycol and 25 µL are then added. After preparing the gold nanoparticle ink, it is placed in the cartridge and loaded into the inkjet printer to produce the conductive sensor on a glass substrate, as explained in chapter 3.4.1.

Before using the ink, a UV-Vis spectrum is performed to check if there are some aggregates. It is important to ensure that there are no aggregates in the ink to prevent clogging the cartridge printhead during printing. From the spectrum in Figure 35 below, the characteristic plasmon peak of AuNPs is observed at 520 nm.[59] Given that the peak is narrow and sharp, and there are no shifts to longer wavelengths, the absence of aggregated nanoparticles can be assumed.

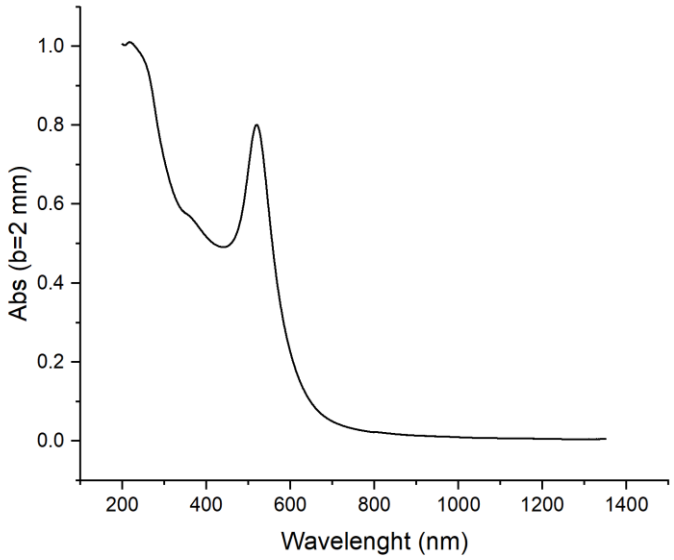

Figure 35: UV-Vis spectrum of the AuNP ink 0.2 µM 1000x diluted

The pattern of the sensor was created using the program INKSCAPE and the geometry is showed in Figure 36:

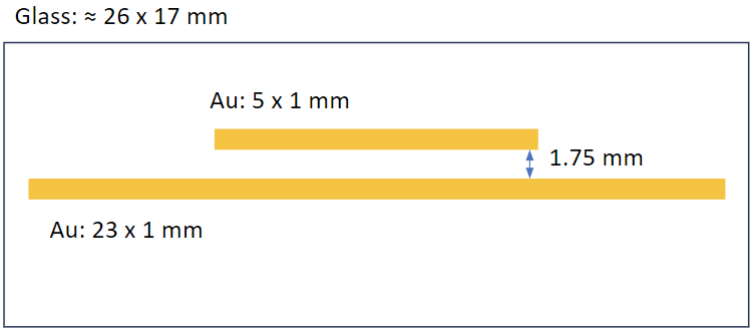

Figure 36: Geometry of the substrate.

This pattern design was chosen to evaluate the print quality and the ink formulation.

Once the substrate is printed it needs to be cured at 500 for 3h in a tubular furnace under an air atmosphere. This thermal treatment is mandatory to enhance electrical conductivity because it induces additive degradation and nanoparticle fusion. Once the substrate is cured, its resistance is measured with a tester. This substrate showed an electrical resistance of about 117 Ω once connected at the two edges of the longest strip. This value is in line with similar electrodes produced using inkjet printing technique but with a different ink formulation, such as PVA or L-cysteine instead of PEG-SH.[60]

To understand the morphology of the printed substrate, SEM (Scanning Electron Microscopy) and SNOM (Scanning Near-field Optical Microscopy) characterizations were performed and are reported in the Figures below.

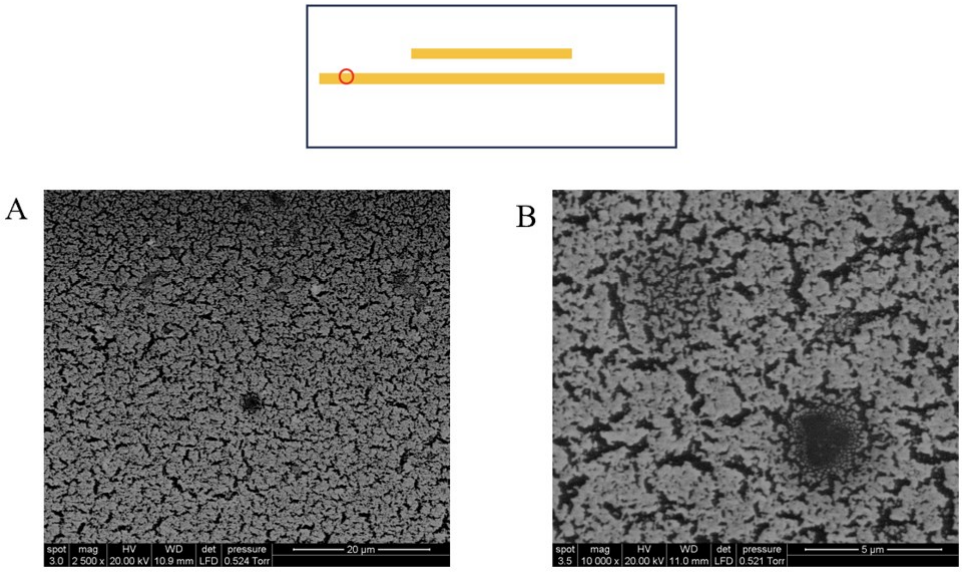

Figure 37: A) SEM image of an inkjet-printed sensor.
B) Zoom on the cavity.

As shown in the Figure above, there are some cavities in the sensor. Despite being a structural defect, these cavities can be very useful for sensor functionalization, as molecules can penetrate inside them, and the overall active area of the thin film is greatly increased. Is it of worth noting that the gold film is not very homogeneous, as it exhibits some cracks as shown in Figure 38. In case of these defects would be too much or too wide, they may potentially cause breaks in the electrical circuit and must be therefore carefully controlled.

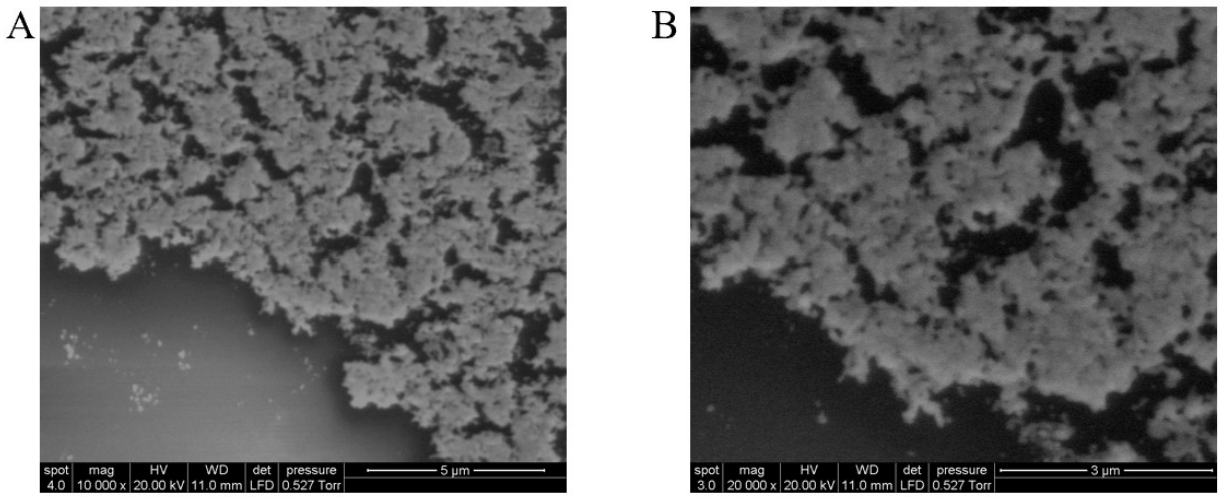

Figure 38: A) SEM image of an inkjet-printed sensor.
B) Zoom on the cracked area.

Using the Scanning Near-field Optical Microscopy it is possible to investigate the film surface at the nanoscale. The instrument performs near field excitation at 522 nm through a 100 nm aperture over a metalized optical fiber, acting as probe, and collect the far field light both in transmission and in reflection (about 30 to 45° from the normal). The reflected light (Figure 31b) is used to study the scattering properties of the sensor, while the transmitted light (Figure 31c) is useful to investigate the absorption of the light passing through the thin film. From the SNOM measurements, it was possible to measure the thickness of the substrate, which was found to be approximately 250 nm, consistent with measurements on other substrates produced using the same inkjet printing technique but with different ink formulations.[60]

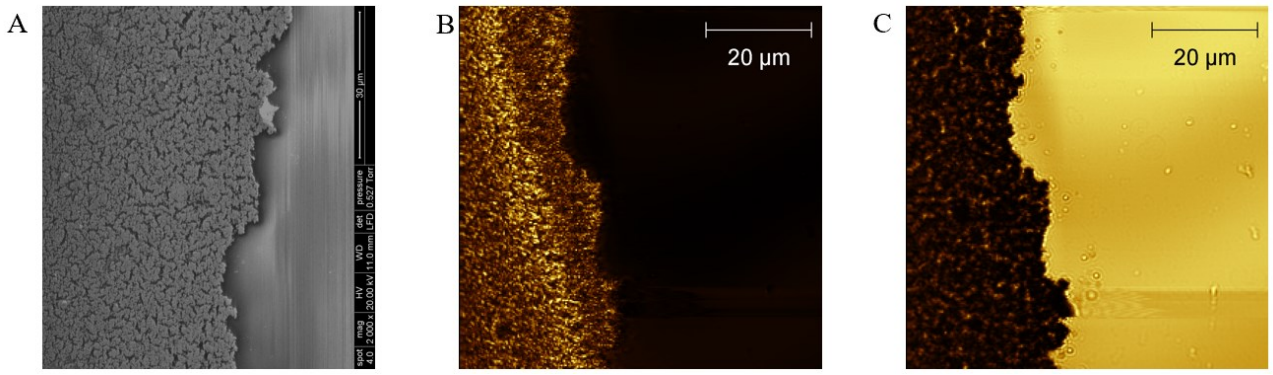

Figure 39: A) Section of the inkjet-printed sensor.
B) SNOM image of the reflected light.
C) SNOM image of the transmitted light.

For this thesis work, inkjet-printed sensors weren't utilized due to several reasons. Although it is one of the best techniques for producing sensors, capable of creating micrometer-resolution substrates with patterns of any geometry, it has been set aside due to resource constraints in terms of time and materials. For instance, the ink production requires extensive time. It involves generating a nanomolar

solution of gold nanoparticles through laser ablation, which could take up to 6 hours to produce a batch of 270 mL. Following this, as outlined in Chapter 3.4.1, the correct amount of PEG-SH needed to be added to the AuNPs solution, which was then centrifuged. PEG is used prior centrifugation as a stabilizer to prevent nanoparticle aggregation.[61] However, before centrifugation could begin, it was necessary to wait a night for PEGylation of AuNPs. Subsequently, to obtain the ink, three centrifugation cycles were required, each lasting half an hour resulting in a final volume of concentrated nanoparticles of about 0.5 ml, to which ethylene glycol and TWEEN 20 were finally added. Therefore, to produce 0.5 mL of ink, 72 mL of ablated gold nanoparticles and many hours of work were required. Despite the use of PEG-SH to prevent nanoparticle aggregation, it may occur anyway during centrifugation, necessitating filtration through a cellulose filter with 0.44 μm pores to eliminate aggregates and prevent clogging of printer nozzles. To produce a print, at least 1 ml of ink is needed, part of which is used during the printing startup to ensure the proper functioning of the printer cartridge nozzles. It is evident that the preparation of even a few milliliters of ink involves significant time and material, which is why faster techniques such as spray coating have been preferred for producing thin films for this project.

Figure 40: example of an inkjet-printed sensor. It can be noted that the surface is very uneven and thin, making the conductivity of the sensor impossible.

4.1.2 Sensors produced via spraycoating.

The colloid dispersion of Au nanoparticles used for the spray coating technique is prepared through LASiS synthesis as explained in chapter 3.2. Once the ablation is completed, a UV-vis spectrum of the solution is performed to verify the absence of aggregates and to assess the concentration.

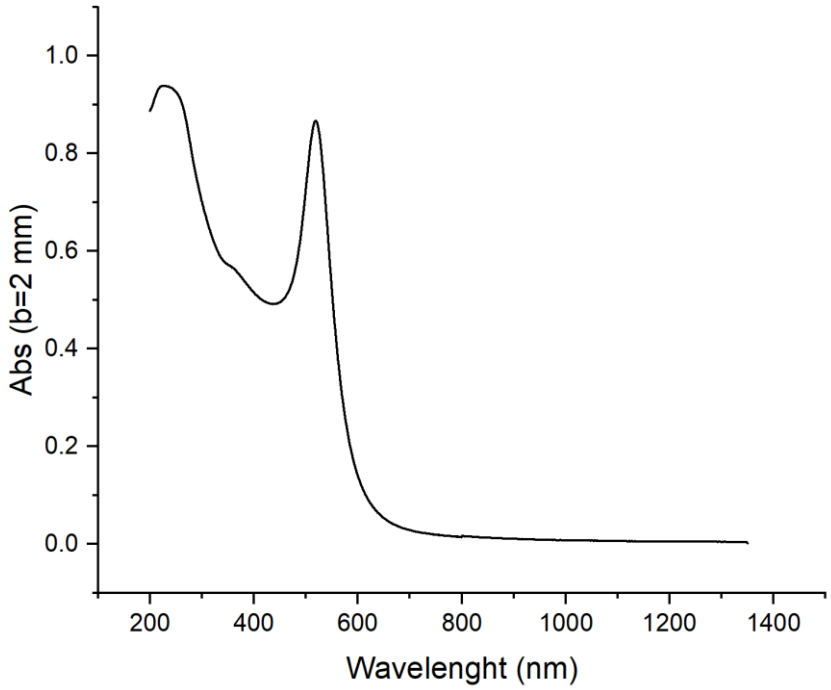

Figure 41: UV-Vis spectrum of the ablated gold nanoparticle solution after 2h 30.

From the spectrum represented in Figure 33, it can be observed that the characteristic peak of gold nanoparticles is present at around 520 nm. Since the peak is narrow and the curve is steep, it can be confirmed that there are no aggregates present.

The MATLAB program,[57] developed within the hosting laboratory, offers a method to determine the concentration of particles in solution by fitting the extinction spectrum. It employs BEM (Boundary Elements Methods) simulations, which calculate the interaction between electromagnetic radiation and nanoparticles, adopting a finite element approach that considers only the physical boundaries between different materials (gold and water in this case). This approach not only allow the estimation of particles concentration, but also facilitates the monitoring of their aggregation status. Figure 34 illustrates the insights provided by this software concerning nanoparticle aggregation and concentration.

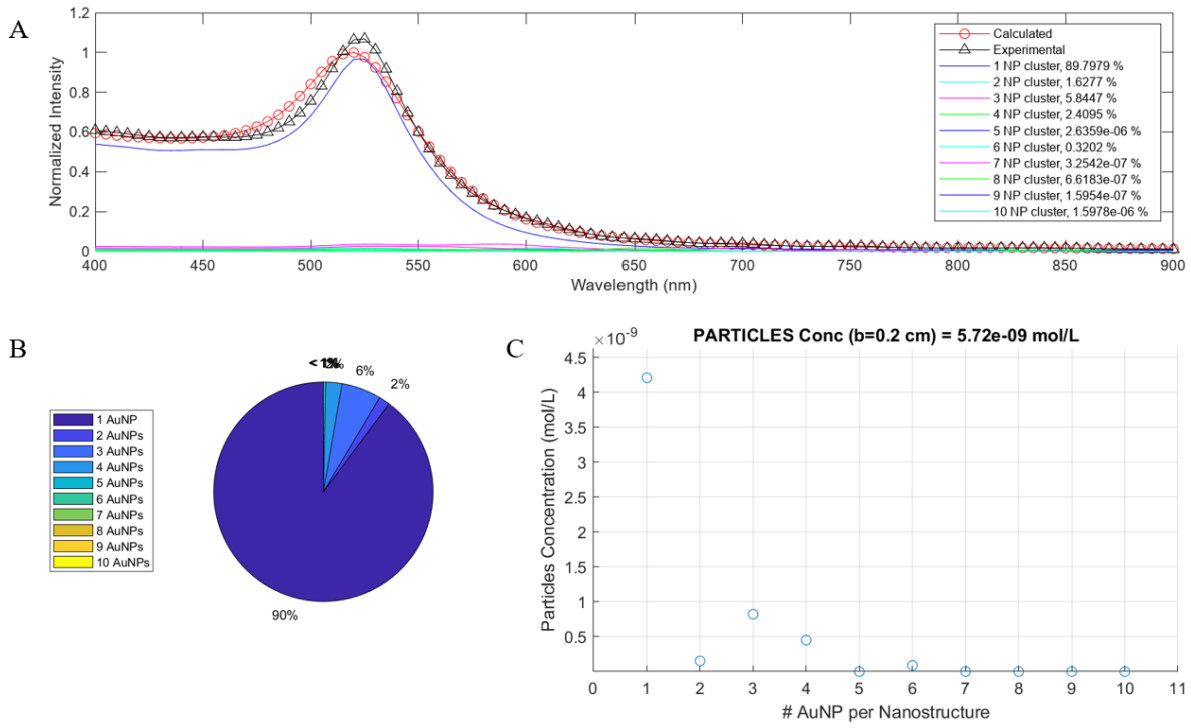

Figure 42: information obtained through the FitSpettri MATLBAB program. The upper part (A) displays the adsorption spectrum of AuNPLasis alongside the fit processing. In the lower-left section (B), a pie chart illustrates the proportion of aggregated nanostructures within the solution. At the bottom-right corner (C), the concentration of nanoparticles is expressed in mol/L.

From the Figure above, it can be stated that there are no aggregates present in the solution, and the concentration is $5.72x10^{-09}$ mol/L.

20 ml of AuNP solution were therefore sprayed onto a glass slide using an airbrush to produce the sensor reported in Figure 43. The glass slide was placed on a heated plate at 125°C, and spraying was done from a distance of 20 cm. To produce the sensor's geometry when performing the spraycoating technique a metal mask should be used. In this work was used a mask that reproduced a bar measuring 1 cm x 2mm, attached to the glass using magnets. The edges of the sensor are not sharp, likely due to the mask not perfectly adherent to the glass despite the use of strong magnets.

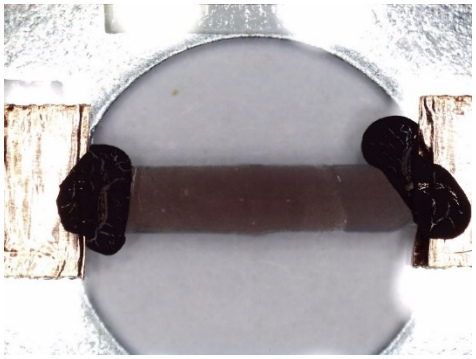

Figure 43: Image of the spray coated AuNP thin film.

As it is possible to see from the image above, the thin film is far more uniform in comparison to the one produced via inkjet printing and reported in Figure 40. It Indeed show a lower electrical resistance of about 60 Ω once connected at the two edges of the strip (about 1 cm distance). To thoroughly study the surface of the sensor produced with the airbrush, it was subjected to a SNOM inspection. As shown in Figure 44, the center of the sensor is scratched to obtain an accurate measurement of the thickness, since the edges of the sensor are not sharp enough.

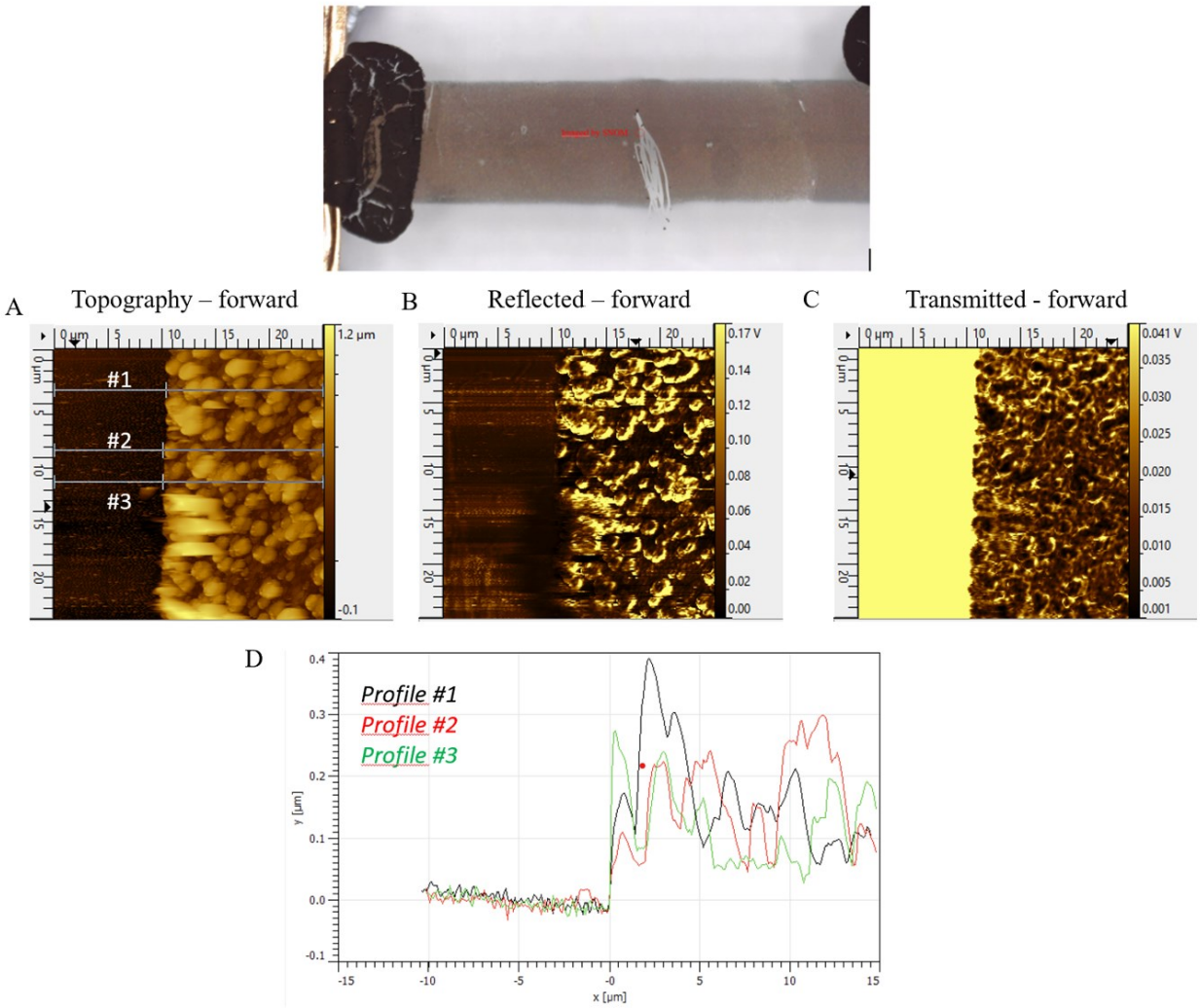

Figure 44: SNOM images. 522 nm exc – 25x25 µm – 3 µm/s – interacting. A) Topography B) Reflection C) Transmission D) Thickness of the three profiles.

In Figure 44, the topography of a section of the sensor is shown, selecting an area of 25x25 µm. From the topography, it is possible to see the edge between the AuNP film and the glass, and therefore the surface roughness. The resolution of the SNOM technique in topography is not sufficient to resolve a single particle and determine its size, but it does reveal a nanometric roughness resulting from the deposition of individual AuNPs. Three profiles were then selected in different positions to observe

how the surface thickness varies, as shown in the diagram. On average, there is a gold layer approximately 0.15 µm thick, with heights reaching up to 0.4 µm.

Another interesting observation that can be made from the transmission image of the sensor, as well as from the reflection image, is that the centers of the nanoparticles appear dark because they absorb light, while the edges are bright. This could be due to the hot-spot effect of the gold nanoparticles.

Surface Enhanced Raman Scattering characterization

It is also important to estimate the SERS Enhancement Factor of this spray coated substrates because it is one of the most important feature for characterizing the SERS effect. Usually, average SERS EFs are of the order of 10^4-10^6, and the EF strongly depend on the exact SERS conditions such as the substrate, the analyte and the excitation conditions.[31] To calculate the Enhancement Factor, aspray coated sensor was used on under two different measuring conditions (namely under 633 and 785 nm excitation). For Raman measure was used a sample of MBA powder, whereas for SERS experiment a drop of 4-MBA solution (about 1 mM) was cast over the substrates and left to react for three hours without letting the drop dry. Afterwards, they were rinsed with water and dried gently under N_2 flow. The surface variability was accounted by mapping the thin film over 99 spectra in a grid of 10x10 µm, so that the final result does not represent just a specific point, but an avarage. To calculate the EF was used the procedure below already published:[60]

$$EF = \frac{I_{SERS} \times N_{BULK}}{I_{BULK} \times N_{SERS}} = \frac{I_{SERS} \times N_{BULK}}{I_{BULK} \times \frac{Spot\ Area \times Ironed\ Surf}{Geometrical\ sampled\ area\ \times Surf\ HINDR\ (MBA)}}$$

Where I_{SERS} is the surface-enhanced signal intensity of the probe at a specific band, I_{BULK} is the corresponding Raman intensity of the MBA powder for the same band, N_{SERS} and N_{BULK} are the numbers of molecules probed, for SERS and Raman measurements.[31] Both the intensities (I_{BULK} and I_{SERS}) referred to the peak at about 1580 cm^{-1}.

To determine N_{BULK} it was assumed that the entire focal volume contributes to the measured signal. The first step involves measuring the effective sample volume irradiated by the laser. The confocal volume is: $V_{confocal} = \pi^{3/2} \cdot w_0^2 \cdot z_0$ where w_0 is the probe volume radius and z_0 is the half-height. Knowing the density of the 4-MBA (1.5 g/cm^3), and thus, the number of molecules of 4-MBA probed by the Raman measure on the powder sample was accordingly calculated:

$$N_{BULK} = \frac{density_{\ MBA} \cdot V_{Confocal}}{MW_{MBA}} \cdot Avogadro's\ Number$$

To calculate the N_{SERS} was used the sample surface under the laser spot. Z_0 was measured experimentally by acquiring Raman spectra of the printed sample along the z-direction and, consequently, w_0 was calculated. The area of the laser spot (A) was then given by: $A = \pi \cdot w_0^2$. Ideally, it was considered that a monolayer of 4-MBA formed on the surface of the printed sample. However, the geometric area under the laser irradiation does not precisely match the actual area accessible to the 4-MBA molecules due to the roughness and nanostructured surfaces of the samples. To achieve a reliable estimation, the roughness measured by probe microscopy (SNOM) was used and the real surface area was calculated. Using the known surface hindrance of 4-MBA molecules, which is 0.348 nm^2, N_{SERS} value was determined.[62]

$$N_{SERS} = \frac{Real\ Area\ under\ laser\ spot\ x\ ironed\ surface}{Geometrical\ sampled\ area\ x\ Surface\ hindrance_{MBA}}$$

Where the known values and the experimental values are listed respectively in table 1 and 2 below:

	NBULK	**IBULK**	**Spot Area (µm^2)**
633, 50x, 6mW	1.61x10^{12}	49	2.58
785, 50x, 30mW	2.05x10^{12}	123	4.24

Table 1: known values

Conditions	**I(sers) avg.**	**N. spectra**	**Grid (µm x µm)**	**Geom sampled area µm^2**	**Ironed surface (µm^2)**	**Real area under spot (nm^2)**	**NSERS**	**EF**
633, 50x 1.5mW, 1x1s	3807.2	99	10x10	25	30.39	275x10^4	7x10^6	**6.23x10^6**
785, 50x, 0.6mW, 1x1s	171.1	99	10x10	25	30.39	515x10^4	1.3x10^7	**2.10x10^5**

Table 2: experimental values

So with these spray coated substrates, enhancement factors ranging from 10^5 to 10^6 are obtained. Although the substrates using the 633 nm line showed a higher enhancement factor, the measurements in this work were performed with the 785 nm line as the Nile Blue molecule has a partial resonance with the last. This provides a further advantage by the resonant-Raman of the Nile Blue with the 785 nm excitation.

Electrochemical characterization

In addition to optical characterization, an electrochemical characterization of the sensor produced via spray coating, without any functionalization, was also conducted. The electrochemical cell was composed by a substrate, as working electrode, a Pt wire as counter electrode and an Ag wire in a saturated solution of KCl as pseudo-reference. $K_3[Fe(CN)_6]$ is used to calibrate potentials relative to the used pseudo-reference (Fig. 45a), so from now on, all the potentials are shifted by -0.195 V. A pH 5 Phosphate buffer is used in any electrochemical experiment hereafter, as electrolyte.

First, it is important to perform an Open Circuit Potential that is an electrical quantity that measures the potential difference between two electrodes immersed in an electrolytic solution when there is no current flowing between them, hence when the circuit is open. It represents the equilibrium potential of an electrochemical system and serves as the starting point for any cyclic voltammetry, for instance. It was found an equilibrium potential of -0.545 V vs Fe(III)/Fe(II). After that, a cyclic voltammetry is conducted to study the sensor.

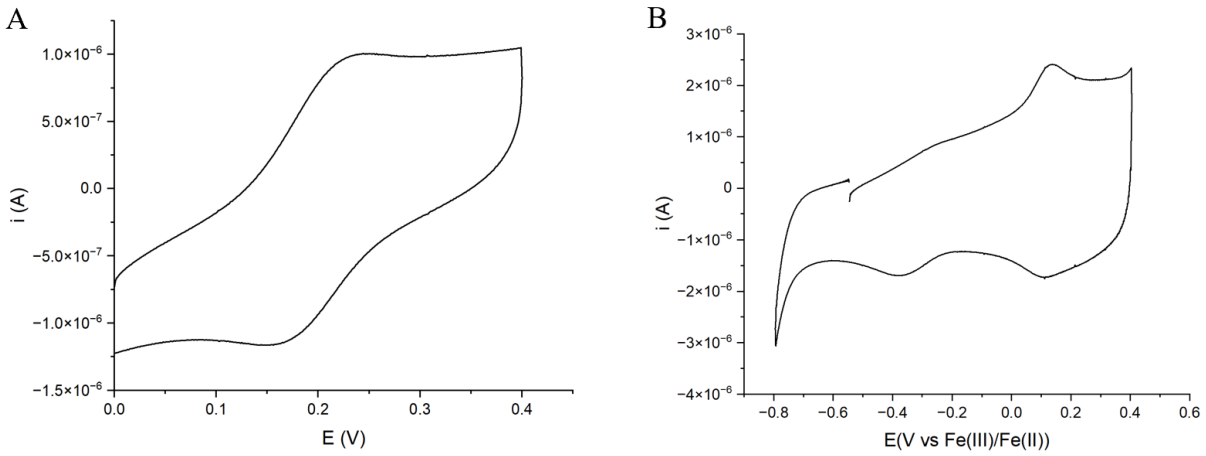

Figure 45:A) Cyclic voltammetry of the spray coated sensor with Ferrocyanide, scan rate of 0.1 V/s. In this measure the potential are referred to our pseudo-reference electrode. B) Cyclic voltammetry of the bare spray coated sensor, for this measure the potential are calibrated with Ferrocyanide.

In order to study the sensor, a quite large potential window is monitored, in this case ranging from -0.8 to 0.4 V vs Fe(III)/Fe(II). The peak at -0.37 V is attributed to oxygen that is likely trapped inside the gold nanoparticles, as it disappears by performing multiple cyclic voltammetries and flushing

with argon. It can be also observed a reversible peak at a potential of approximately 0.13 V vs Fe(III)/Fe(II).

To better visualize this last peak, it is useful to perform a Differential Pulse Voltammetry (DPV) both in reduction and oxidation as reported in the Figure below (Fig. 46):

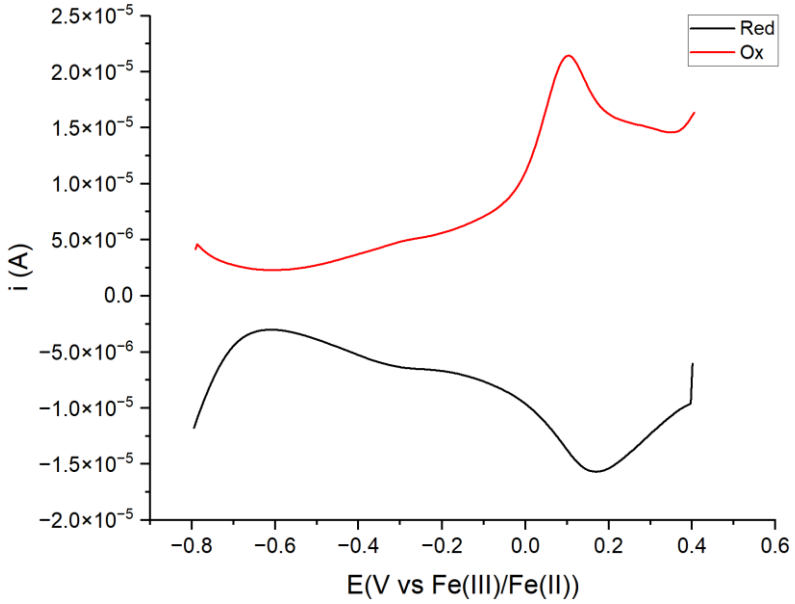

Figure 46: DPV in reduction (in black) and DPV in oxidation (in red).

The DPV confirmed the reversible peak, this redox process is characteristic of our sensor and is observed on every sensor tested.

The characterization of the thin film continues by performing multiple cyclic voltammetries at decreasing scan rates, ranging from 0.5 V/s to 0.01 V/s, to understand the nature of these peaks. (Fig 47). The relationship between the peaks intensities and the scan rate is used to establish whether a species are adsorbed on the electrode, instead of free to diffuse away into the bulk of the electrolyte (Figure 48a and 48b). The first case (adsorption) is evidenced by a linear dependence between the peaks intensities and the scan rate. While a direct linearity between peak intensities and the square root of the scan rates describes a diffusion-controlled process.[6]

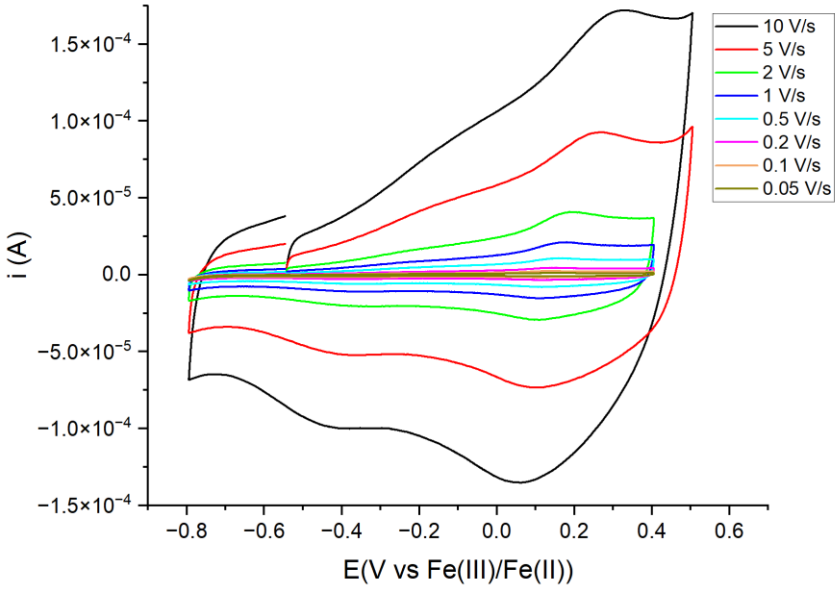

Figure 47: CVs at different scan rates.

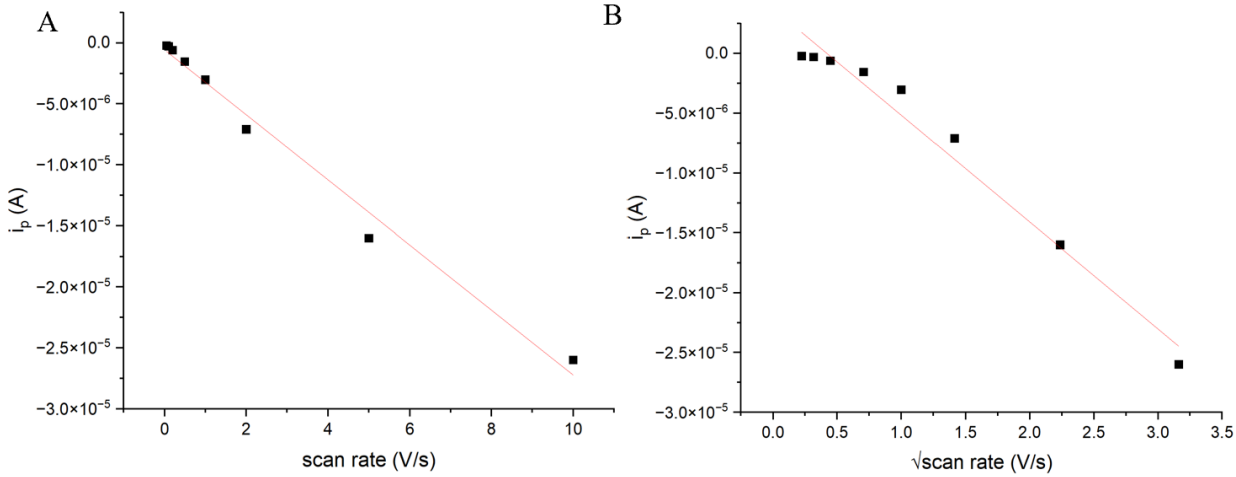

Figure 48: A) peak current at -0.13 V vs Fe(III)/Fe(II) vs scan rate. B) peak current vs the square root of scan rate.

From the two graphs above, it seems that Figure 48a exhibits greater linearity. Therefore, it can be confirmed that those peaks are due to something adsorbed on the gold nanoparticles. Later in this chapter, it will be shown that the presence of an adsorbed specie on the sensor, whose nature is still under investigation, does not pose a problem when the sensor is functionalized with Nile Blue molecules, as the redox process will no longer be observed (Fig 58). Regarding the use of the sensor without functionalization, having an electroactive species absorbed on the surface could interfere with the investigated process.

4.2 Response of the Cr(DPCO) complex to different concentrations of Cr(VI)

As explained in chapter 2.1.3, an established colorimetric assay for hexavalent chromium is by using the DPC (1,5-Diphenylcarbazide) ligand. This ligand forms the Cr(DPCO) complex when it reacts

with hexavalent chromium. Hereafter, we investigate the opportunity to run SERS measures on the last with the aim to achieve a greater sensitivity. The procedure foresees that, after the DPC and chromate reaction, the complex is then deposited onto a substrate of gold nanoparticles. Subsequently, the Surface Enhanced Raman Spectroscopy (SERS) technique is employed to analyze the data. DPC is oxidized by hexavalent chromium in an acidic environment, resulting in the formation of the DPCO (1,5-diphenylcarbazone) complex and Cr(III). It is noteworthy that Cr(III) complexes with DPCO, the final product is characterized by an absorption band at 540 nm (Fig. 42) and a violet color.

Through this analysis, a calibration curve for the Cr(DPCO) complex is established to determine the presence of hexavalent chromium. It's important to remember that the legal limit for hexavalent chromium in drinking water is $2x10^{-8}$ M.[6]

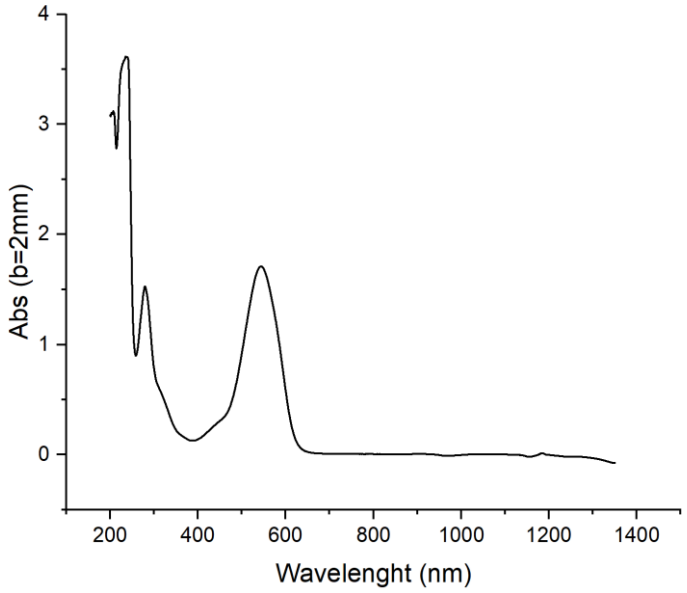

Figure 49:UV-vis spectrum of Cr(DPCO) complex 10^{-3} M, the characteristic band is shown at 548 nm.

First of all, a solution of Cr(DPCO) was prepared by mixing DPC and CrO_4^{2-} at a known concentration, then gradually diluting to obtain a calibration curve. Sulfuric acid with a pH of 2 was used as the acid. The resulting stock solution is therefore at a concentration of 10^{-3} M and consists of 300 µL of DPC, 200 µL of Cr(VI), and 250 µL of H_2SO_4. The stock solution is then diluted with MilliQ water to obtain solutions as the following concentrations: 10^{-4} M, 10^{-5} M, 10^{-6} M, 10^{-7} M, $5x10^{-8}$ M, 10^{-8} M, $5x10^{-9}$ M, 10^{-9} M, 10^{-10} M, 10^{-11} M, 10^{-12} M. Once the solutions are prepared, they are deposited onto the sensor for analysis by Raman Spectroscopy. It is essential to prevent the Cr(DPCO) solution droplet from drying out, so wells have been created around the center of the sensor, into which 40 µL of solution is deposited. The objective chosen is an Olympus 20x operating at long working distance.

The first spectrum for each dilution was taken in the spectral range between 200 cm^{-1} and 2000 cm^{-1}, to verify the presence of the characteristic peaks of the Cr(DPCO) compound, which are approximately at 841 cm^{-1}, 1292 cm^{-1}, 1352 cm^{-1}, and 1592 cm^{-1} as reported in a previous work.[63] Then, a series of equally spaced spectra was acquired (total of 120 spectra, 100 µm spaced in both x and y directions)(Fig. 53). The same conditions of objective magnification and laser power are used for each sample, with only the acquisition time varying, namely increasing time as the concentration decreases. A blank map is also measured, representing the absence of the Cr(DPCO) analyte, using a solution composed by 300 µL ethanol, 200 µL MilliQ water and 250 µL sulfuric acid pH 2.
In the tables below, the specific parameters are reported for laser power of 3 mW and 6 mW (Tab. 3). Two laser powers are used to achieve the best compromise for obtaining a good signal without compromising the sample.

Concentration	**Acquisition Time (laser power 3 mW)**	**Acquisition Time (laser power 6mW)**
10^{-3} M	1x1s	1x1s
10^{-4} M	1x1s	1x1s
10^{-5} M	1x5s	1x2s
10^{-6} M	1x6s	1x4s
10^{-7} M	1x10s	1x7s
$5x10^{-8}$ M	1x5s	1x5s
10^{-8} M	1x5s	1x5s
$5x10^{-9}$ M	1x10s	1x10s
10^{-9} M	1x10s	1x10s
10^{-10} M	1x10s	1x10s
10^{-11} M	1x10s	1x10s
10^{-12} M	1x10s	1x10s
Blank	1x4s	1x2s

Table 3: acquisition times for each concentration for a laser power of 3 mW and 6 mW are reported.

A MATLAB algorithm was implemented and used to analyze the maps obtained for both laser power settings

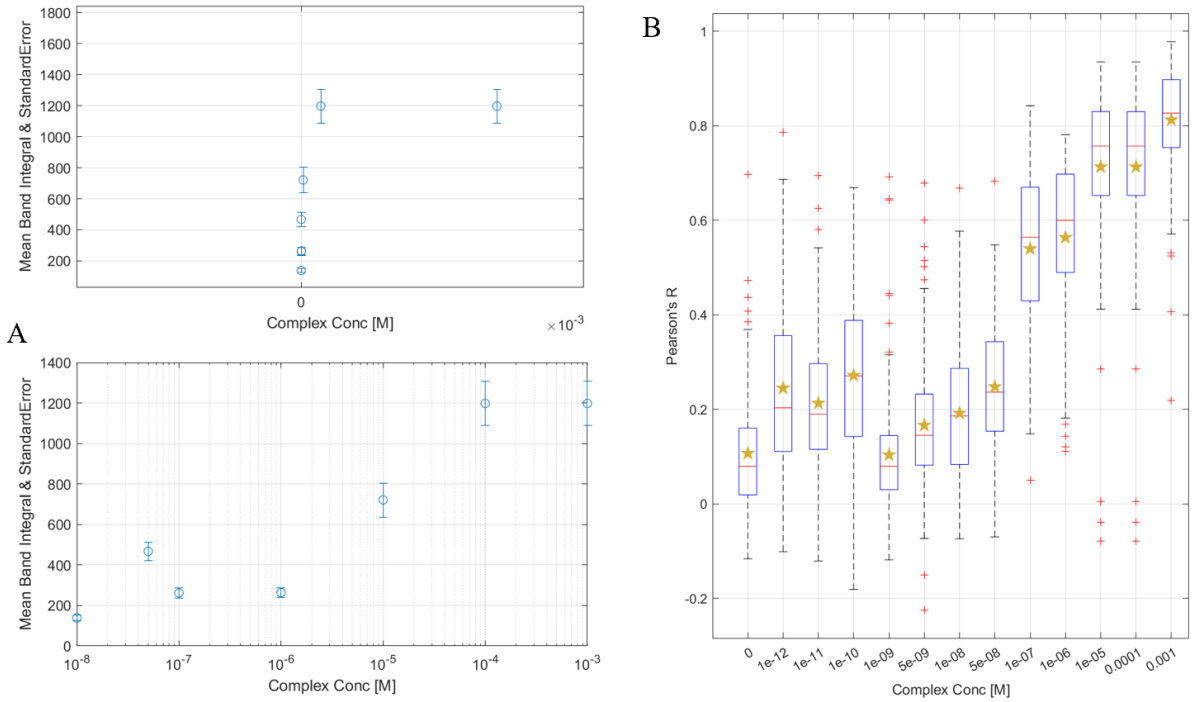

Figure 50: A) calibration curve for the laser power of 3 mW.

B) Pearson coefficients for each concentration value with laser power of 3 mW.

Figure 50a displays the calibration curve obtained by the maps acquired for each concentration at a laser power of 3 mW, while in Figure 50b, Pearson coefficients can be evaluated for each concentration. The Pearson coefficient *R* is a statistical indicator used in this case to correlate the reference spectrum of the Cr(DPCO) complex with each spectrum acquired from the map. If the correlation has a value that is too low for a given spectrum, then it can be confirmed that this spectrum cannot be attributed to Cr(DPCO). Similarly, if the distribution of all spectra acquired from the map at a certain concentration has low R values, it means that, on average, the map has a low presence of the characteristic peaks of Cr(DPCO) (Fig. 54d). Comparing the calibration curves and the Pearson coefficients obtained for both laser powers, it is evident that better results are achieved using the higher laser power. Therefore, only the data obtained from the maps acquired with a laser power of 6 mW are analyzed in detail, as shown in Figure 51.

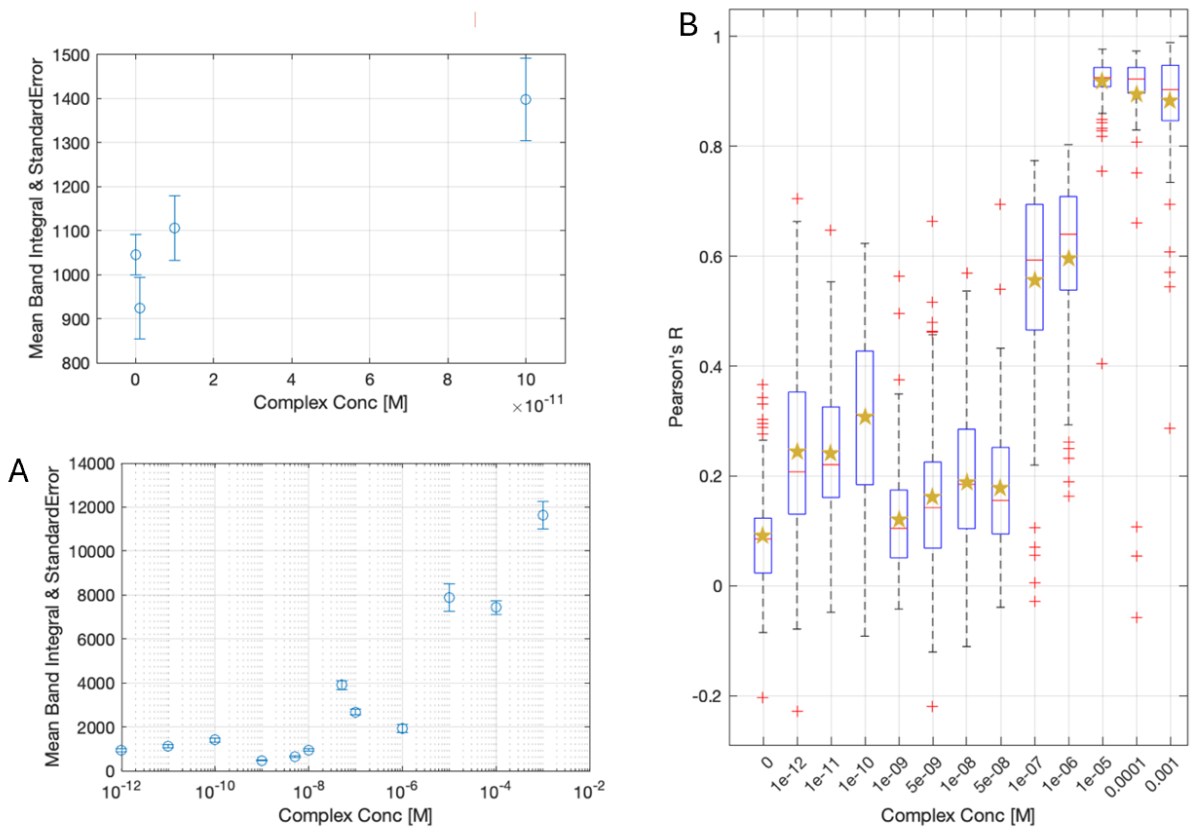

Figure 51: A) calibration curve for the laser power at 6 mW.

B) Pearson coefficients for each concentration value with laser power at 6 mW.

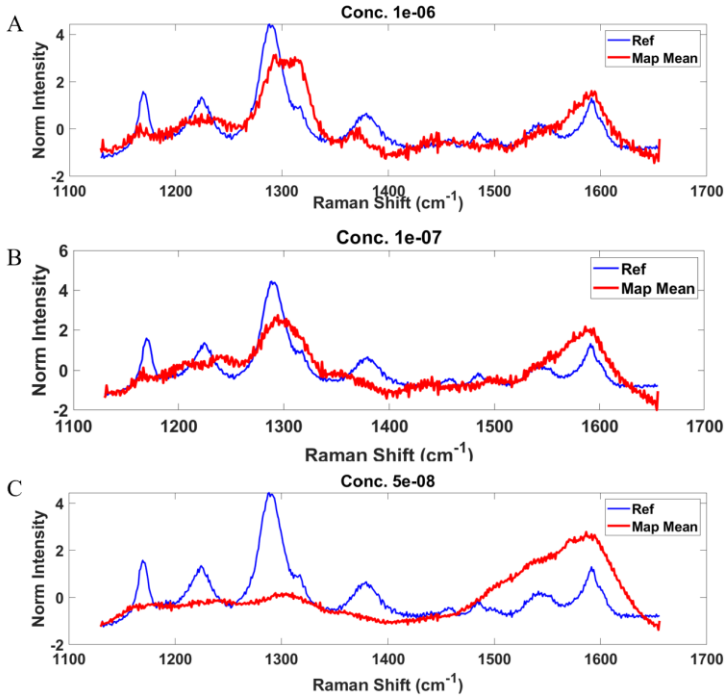

Figure 52 A) Raman spectrum of the map acquired versus the reference spectrum of the Cr(DPCO) compound at a concentration of $1x10^{-6}$ M.
B) Raman spectrum of the map acquired versus the reference spectrum of the Cr(DPCO) compound at a concentration of $1x10^{-7}$ M.
C) Raman spectrum of the map acquired versus the reference spectrum of the Cr(DPCO) compound at a concentration of $5x10^{-8}$ M.

To determine the LOD of the sensor, it is important to closely examine the spectra corresponding to the low concentrations, shown in Figure 52. The spectra of the Cr(DPCO) complex at concentrations of $1x10^{-6}$ M, $1x10^{-7}$ M and $5x10^{-8}$ M, are compared with the reference spectrum of the same. It can be noted that while for the concentrations $1x10^{-6}$ M and $1x10^{-7}$ M (Figures 52a and 52b), although slight, the characteristic peaks of the complex at 1352 cm^{-1} and 1292 cm^{-1} are still present, for the concentration $5x10^{-8}$ M, the peaks are no longer present, or rather, they are not as intense as to be identifiable, as clearly seen in Figure 52c.

From the calibration curve in Figure 51A, it may appear, except for some anomalous values, that there is linearity up to concentration values of $5x10^{-9}$ M. However, upon the closer inspection of the spectrum obtained at a complex concentration of $5x10^{-8}$ M compared to the reference spectrum, it becomes apparent that the compound is no longer identifiable. For this reason, the limit of detection of this AuNPs sensor produced via dropcasting is $1x10^{-7}$ M.

The dispersion of Pearson coefficients for each spectrum acquired from the map at every concentration is then analyzed in detail (Figure 53, 54):

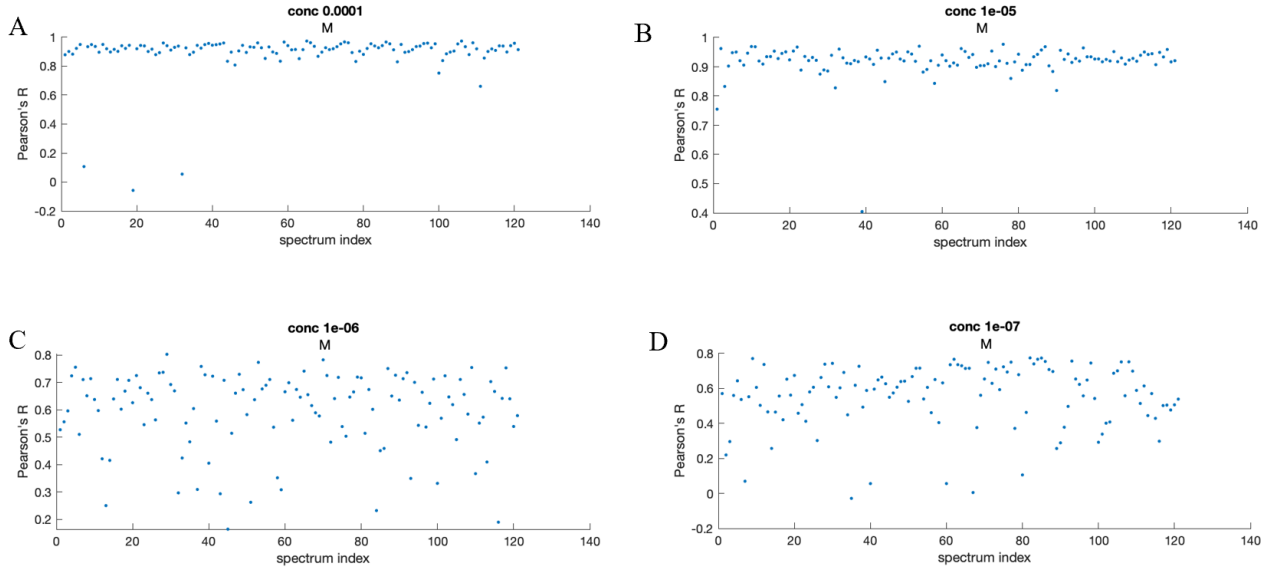

Figure 53: Dispersion of Pearson coefficients at high concentrations of the Cr(DPCO) complex.
A) Concentration complex of $1x10^{-4}$ M.
B) Concentration complex of $1x10^{-5}$ M.
C) Concentration complex of $1x10^{-6}$ M.
D) Concentration complex of $1x10^{-7}$ M.

From the spectra shown in Figure 53, it can be observed that as the concentration decreases, the Pearson coefficients become more scattered. However, since they still maintain a value above 0.5, they are considered acceptable. In fact, for concentration values of 10^{-4} M and 10^{-5} M, R (Pearson

coefficient) is approximately equal to 1 (Fig. 53a and 53b), while for values of 10^{-7} M, R is around 0.5 (Fig. 53d).

The Pearson coefficients for concentration lower than 10^{-7} M are analyzed in the same way and are reported in Figure 54:

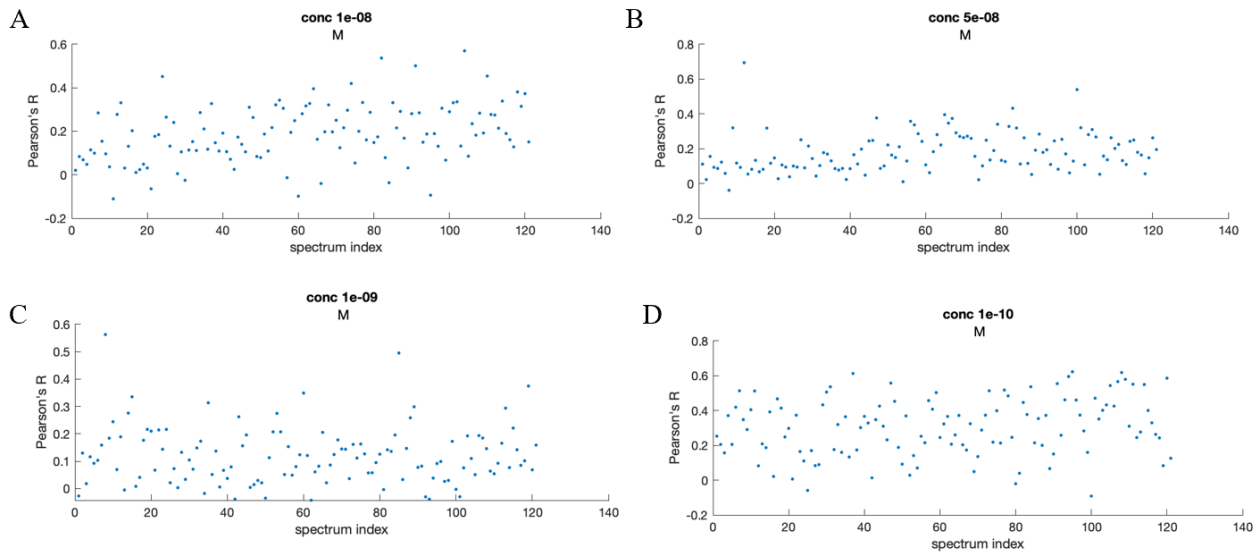

Figure 54: Dispersion of Pearson coefficients at low concentrations of the Cr(DPCO) complex.
A) Concentration complex of 1x10^{-8} M.
B) Concentration complex of 5x10^{-8} M.
C) Concentration complex of 1x10^{-9} M.
D) Concentration complex of 1x10^{-10} M.

As observed in Figure 47, at concentrations lower than 10^{-7} M, the Pearson coefficients are less than 0.5, as in the case of the concentration at 5x10^{-8} M. Indeed, upon examining the average spectrum of the corresponding map, the characteristic signals are not present, and thus, it is not possible to attribute the presence of the analyte Cr(DPCO).

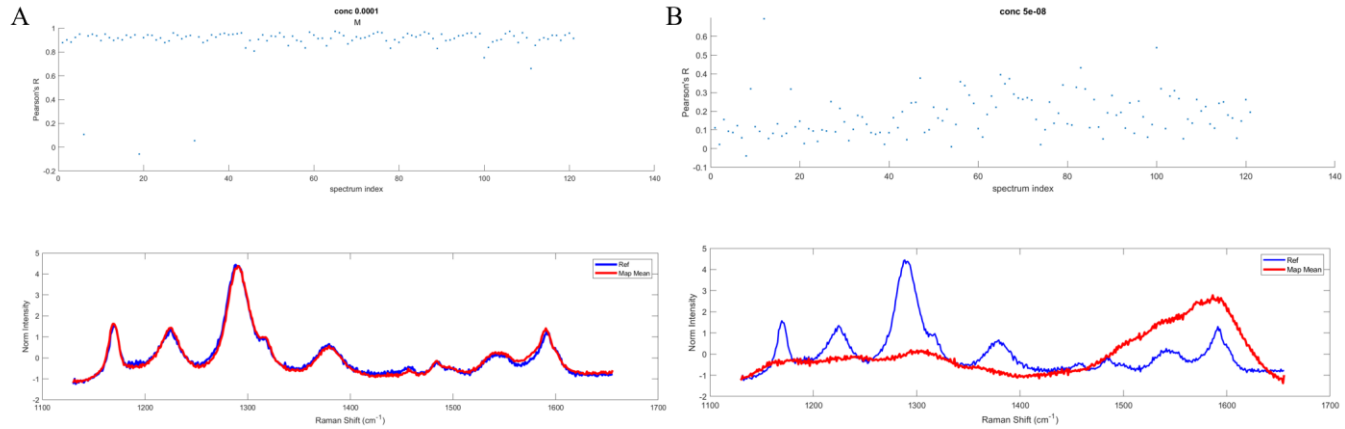

Figure 55 A) Average spectrum of the map at a concentration of 1x10^{-4} M and Pearson coefficient ranging between 0.8 and 1
B) Average spectrum of the map at a concentration of 5x10^{-8} M and Pearson coefficient ranging between 0 and 0.2.

It can therefore be said that R provides an indication about qualitative attribution of a spectrum in respect to a given reference. For high values of R (Fig. 48a), it is observed that the average spectrum of the map is almost coincident with the reference. The same cannot be said for Figure 48b, which has an average R value of approximately 0, and the average spectrum of the map does not contain the characteristic signals.

In conclusion, it can be stated that this method is effective for detecting concentrations of hexavalent chromium only up to $1x10^{-7}$ M. However, the legal limit for hexavalent chromium in drinking water is $2x10^{-8}$ M. Therefore, this method cannot be used for this purpose. Compared to our LOD , other studies utilizing DPC via traditional methods, such as the colorimetric one, achieve higher limits of detection of 0.3 μM.[16,17] On the other hand, there are other studies achieving lower LODs (1.45 nM) using nanoparticle substrates to detect hexavalent chromium through SERS techniques.[19]

4.3 Nile Blue A – functionalized electrodes and SERS substrates.

In this work was used the Nile Blue A perchlorate already functionalized with lipoic acid (lipNB) from a previous work.[54]

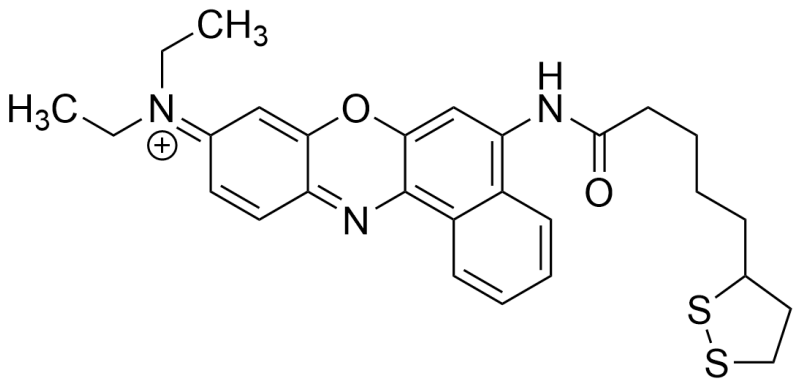

Figure 56: Chemical structure of Nile Blue functionalized with lipoic acid.

Following the procedure described in section 3.5.2, the substrates produced via spray coating were functionalized with lipNB because in its reduced form, it catalyzes the reduction of Cr(VI) to Cr(III) and regenerates in its oxidized form. To achieve this, a EC-SERS spectroelectrochemical cell (already described in chapter 3.5, Fig. 32) is used for all measurements, allowing for analysis from both an optical and electrochemical perspective.

4.3.1 Spectroscopic and electrochemical characterization

First of all, it is important to verify the successful of sensor functionalization. Raman spectroscopy was used on this purpose using a 785 nm laser line, in a range from 200 cm^{-1} to 2000 cm^{-1}, with a 10x

objective and a laser power of 0.06 mW. This low power setting was used to avoid sample damage when analyzed without any solution above that may help to dissipate the heat generated by the laser.

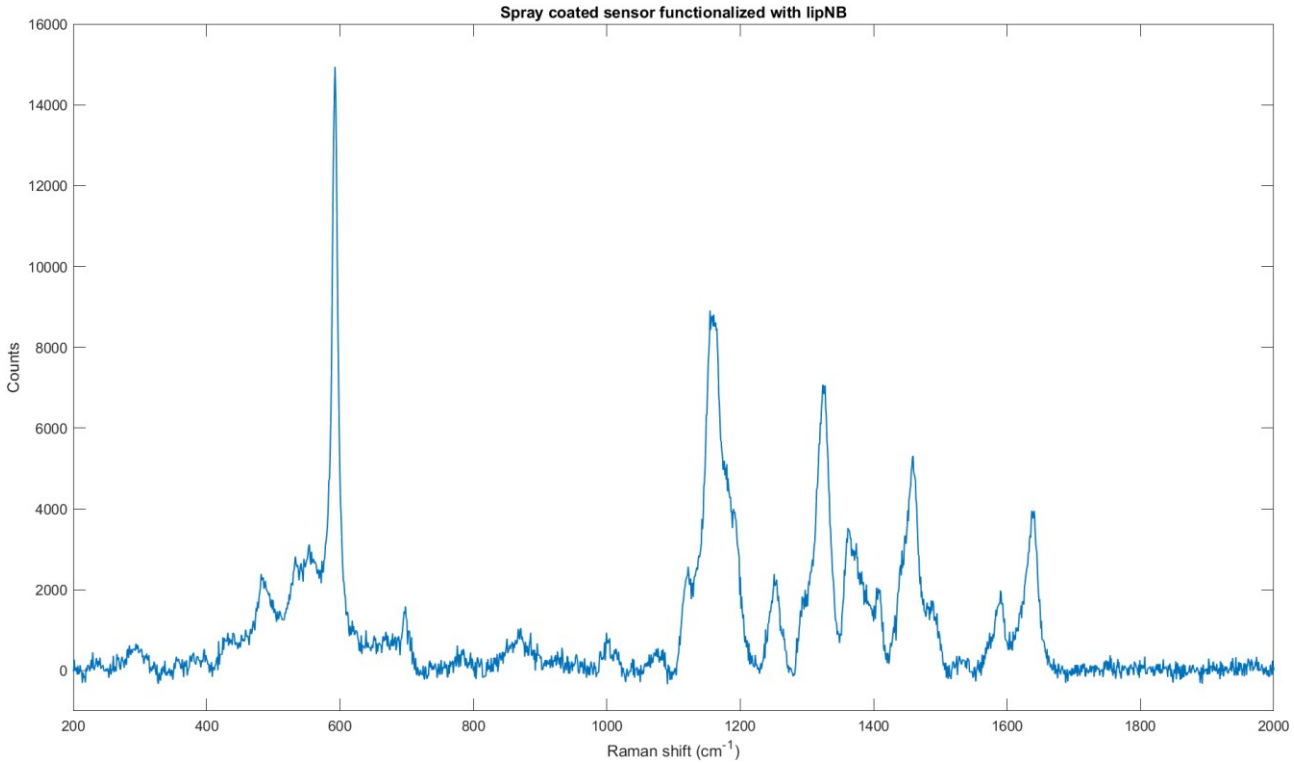

Figure 57: Raman spectrum of the lipNB functionalized sensor.

It can be confirmed that the sensor has been functionalized, as the characteristic peaks of Nile Blue are clearly visible at 591 cm^{-1}, 1150 cm^{-1}, 1250 cm^{-1}, 1320 cm^{-1}, 1360 cm^{-1}, 1490 cm^{-1}, 1590 cm^{-1}, and 1640 cm^{-1}.[64]

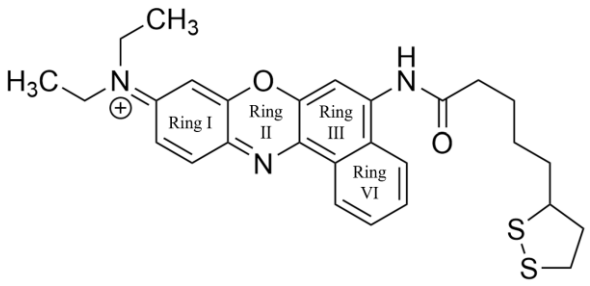

592 cm^{-1}	***1490 cm^{-1}***	***1640 cm^{-1}***
C=N(2)-C and C-O-C (2^{nd} ring)	*C=N (2)*	*C=N (1)*

Table 4: The strongest peaks of the Nile Blue (represented on the left) are reported.

In table 4, the most important and characteristic peals of Nile Blue are reported. The most prominent peak at 592 cm^{-1} is entirely related to the vibrations of the second ring, as shown in the Figure next to the table.

After confirming the presence of lipNB on the surface of the sensor using Raman spectroscopy, electrochemical characterization proceeds with cyclic voltammetry at 0.05 V/s,

followed by differential pulse voltammetry (DPV). For electrochemical characterization, the sensor is placed into the spectroelectrochemical cell along with the pseudo-reference and counter electrodes. All characterization tests were conducted using a phosphate buffer solution at pH 5 as the electrolyte.

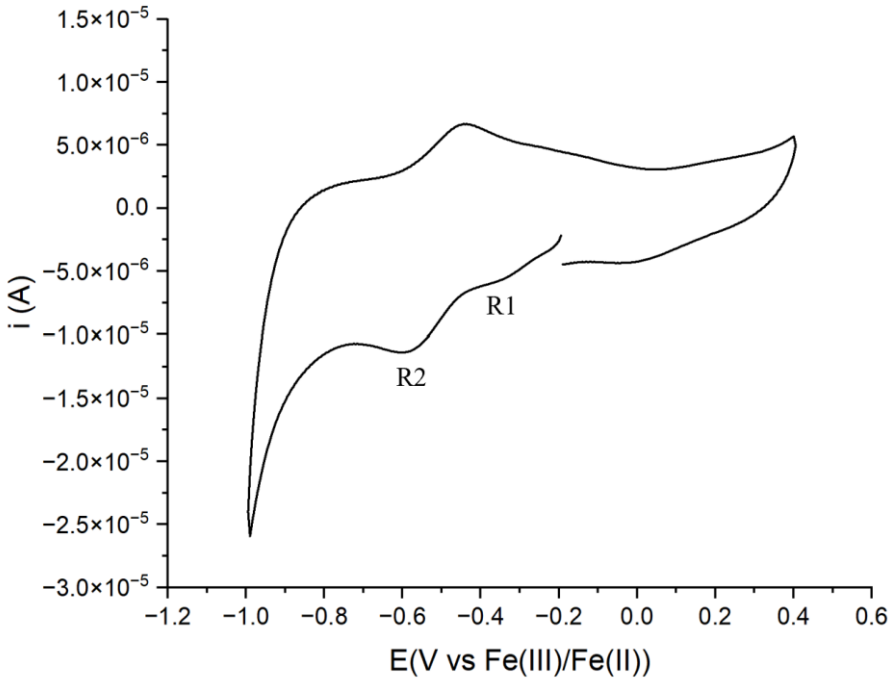

Figure 58 Cyclic voltammetry of the functionalized sensor. Scan rate is 0.05 V/s.

In the cyclic voltammetry shown in Fig. 51, two peaks can be observed, although they are weak at around -0.32 V (R1) and -0.56 V (R2) V vs Fe(III)/Fe(II). The fact they are not very prominent is due to the low amount of Nile Blue on the sensor. Therefore, to see the peaks more clearly, it is necessary to perform a DPV.

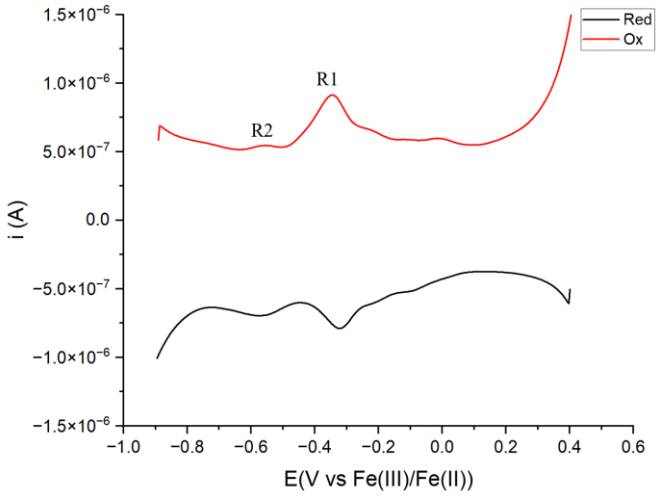

Figure 59 Differential Pulse Voltammetry of the functionalized sensor, in black the reduction while in red the oxidation.

A DPV is performed both in reduction and oxidation, as shown in Figure 52. The peaks are now much more prominent, and two can be identified, one at -0.32 V (R1) and the other at -0.56 V vs Fe(III)/Fe(II) (R2), which represent the two reductions of Nile Blue.[65] One of the advantages of using the EC-SERS spectro-electrochemical cell is that it allowed us to study the behavior of Nile Blue adsorbed on the gold nanoparticle sensor by analyzing how its structure changed during cyclic voltammetry performed at a scan rate of 0.001 V/s, as shown in Figure 60:

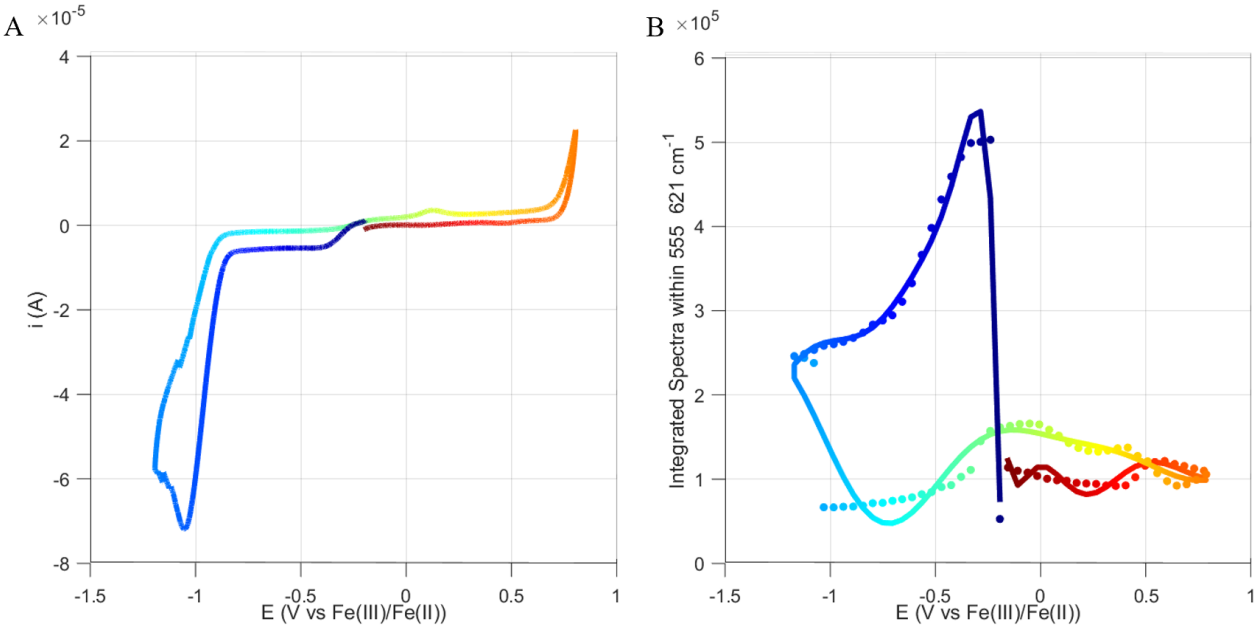

Figure 60: A) A cyclic voltammetry with a scan rate of 0.001 V/s.
B) Trend of the intensity of the characteristic Nile Blue peak at 592 cm^{-1} against potential and time, the color scale goes in chronological order from blue to red.

As seen in Figure 60a, a very wide potential window was used, ranging from -1.195 V to 0.805 V vs Fe(III)/Fe(II), allowing the entire sensor to be studied, namely processes in charge of the Nile Blue, the solvent and the Au electrode itself. All of these are correlated to their influence to the Nile Blue SERS signals by the spectro-electrochemical setup. The peak observed at around -1 V, likely represents the reduction of oxygen present in the aqueous electrolyte solution. From Figure 60b, it can be observed the changes in the intensity of the characteristic Nile Blue peak at 592 cm^{-1} during cyclic voltammetry. As the cyclic voltammetry progresses from negative to positive potentials, it can be seen that before reaching the Nile Blue reduction peak at -0.32 V vs Fe(III)/Fe(II), the signal intensity is very high. However, once the reduction peaks are surpassed, the intensity drops drastically. Following the cyclic voltammetry trend, as the potential returns towards positive values, the Nile Blue peak intensity increases, highlighting the reversibility of Nile Blue in its oxidized and reduced forms. The fact that the intensity is much weaker at the end, compared to the initial state, is

probably due to sensor degradation, as Au oxidation may happened due to the highest positive potentials reached.

Subsequently, the functionalized sensor was studied at different scan rates to prove whether Nile Blue is adsorbed onto the sensor, in Figure 61. To understand whether the species is adsorbed on the sensor or whether we are dealing with diffusion, the peak current should be plotted against the scan rate or the square root of the scan rate.

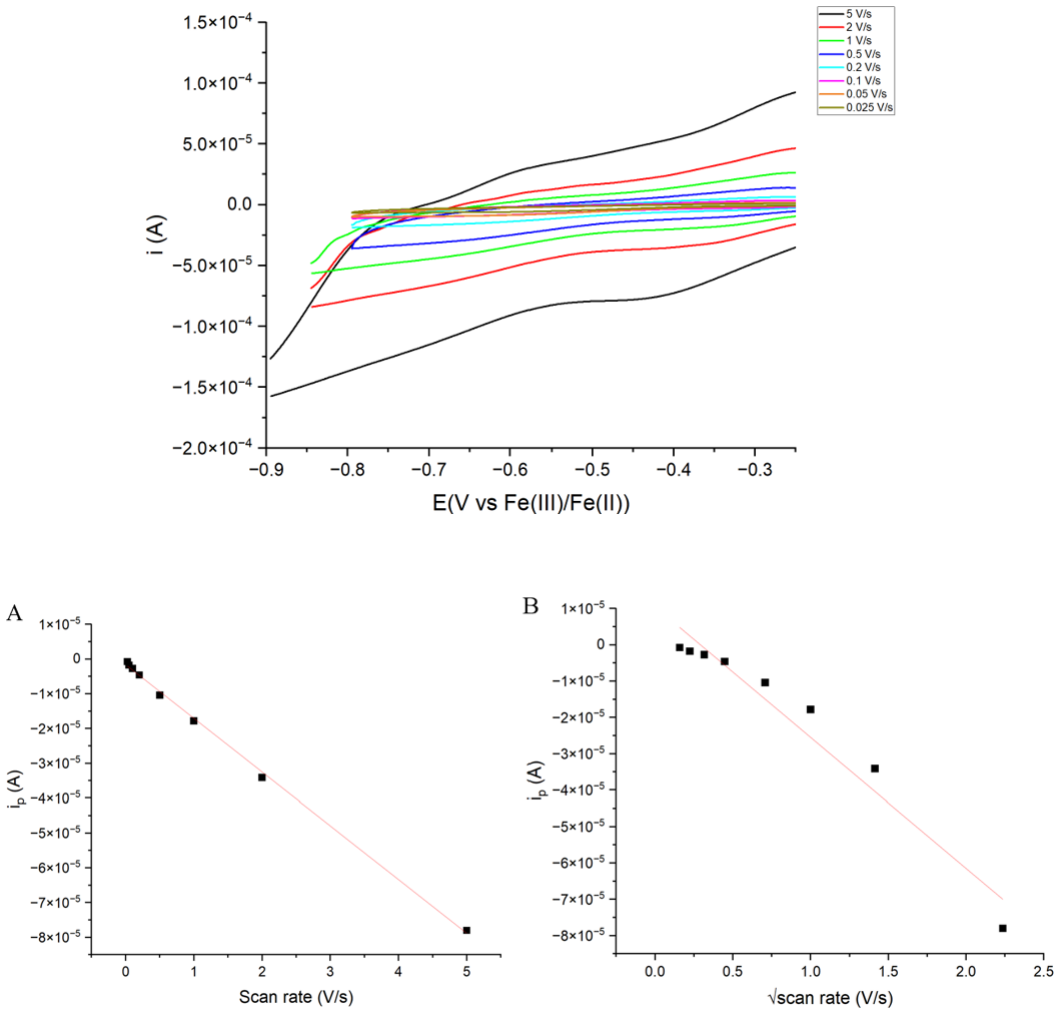

Figure 61 Cyclic voltammetry of the functionalized sensor at different scan rates.
A) peak currents vs scan rate.
B) peak currents vs square root of scan rates.

From Figure 61a, it can be confirmed that the species is adsorbed because i_p vs scan rate is linear.

4.3.2 Electrochemical reduction

After studying and confirming the presence of lipNB strongly adsorbed on the sensor surface, we aim to proceed with the electrochemical reduction of the molecule as it is present in its oxidized form.

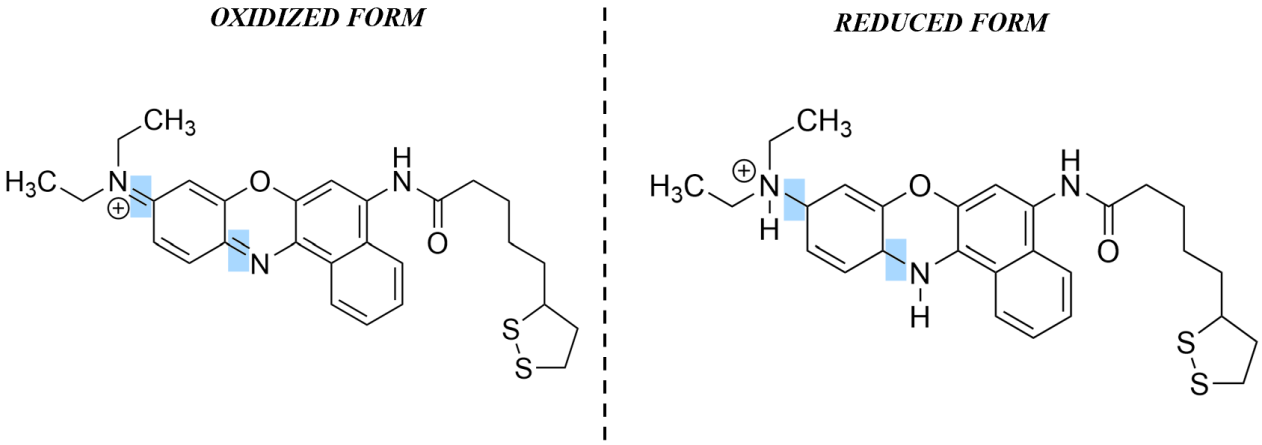

As we can see from the molecular structure, once the Nile Blue is reduced, the double bonds at the nitrogen atoms are lost, while the charge and the rest of the molecule remain unchanged.

The purpose of reducing Nile Blue is to subsequently re-oxidize it with hexavalent chromium, as shown in Figure 62. This process ensures that the higher concentrations of Cr(VI) will result in more pronounced Nile blue peaks, or in an higher current when performing a chronoamperometry.

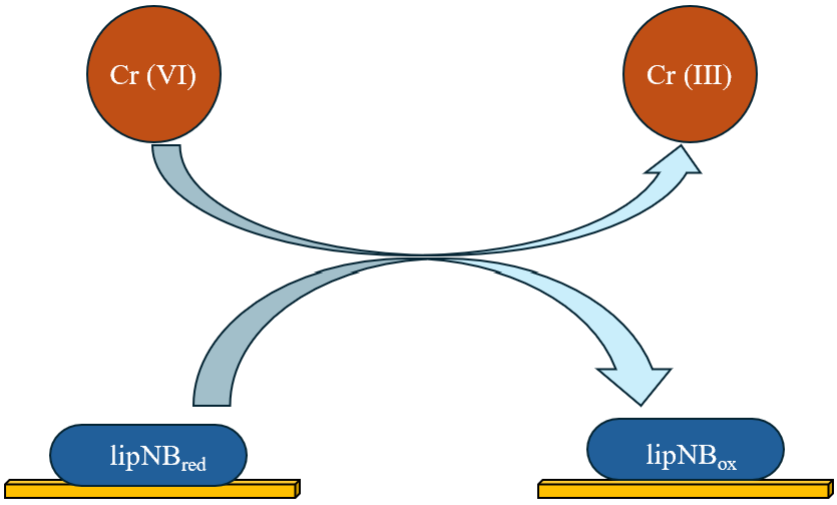

Figure 62: A schematic oxidation of reduced Nile Blue by hexavalent chromium, which is in turn reduced to trivalent chromium.

To electrochemically reduce the oxidized lipNB, an electrolysis of at least 60 seconds is required (Figure 63). For this purpose, a potential approximately 100 mV more negative than the second reduction peak potential is chosen, so that at -0.66 V vs Fe(III)/Fe(II) all the Nile Blue molecules are reduced.

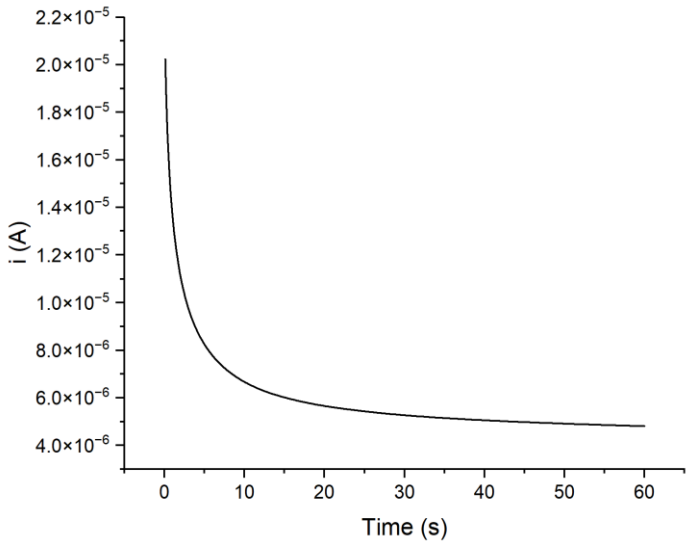

Figure 63: Chronoamperometry of the functionalized sensor at a reduction potential of -0.66 V for a duration of 60 s.

In Figure 63 above, it can be observed that the current takes only a few seconds to reach the plateau, and, consequently, the molecule is reduced in a very short time. To confirm that the molecule is reduced, it is also necessary to acquire a Raman spectrum during and immediately after the chronoamperometry, to see whether the characteristic peaks of Nile Blue are still present or not.

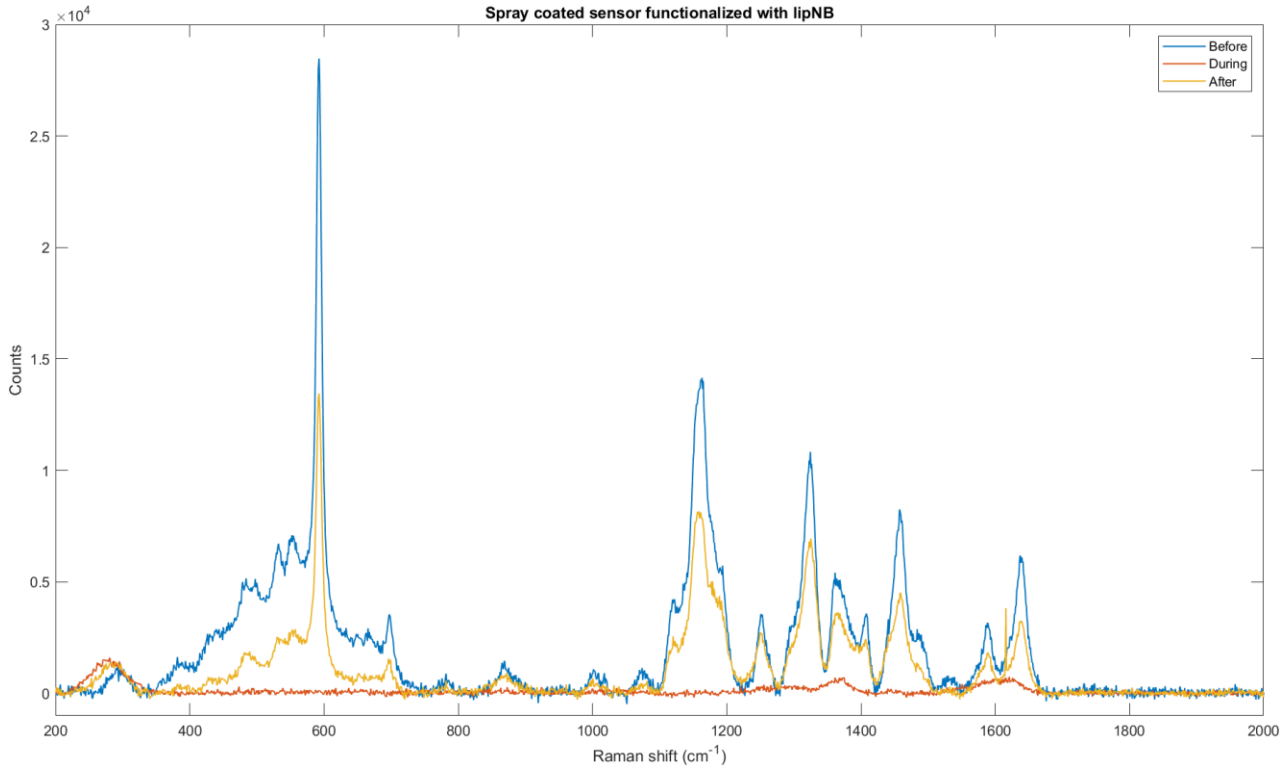

Figure 64: Raman spectra in extended mode for 10 seconds, using a 785 nm laser line, ranging from 200 to 2000 cm^{-1}, with a 10x objective and laser power set at 6 mW.
In blue is the spectrum taken before the chronoamperometry, in orange during the chronoamperometry and in yellow immediately after the chronoamperometry.

In Figure 64, it can be observed that while there are no peaks present during the chronoamperometry, indicating that all the Nile Blue adsorbed on the sensor has been reduced, the Nile Blue immediately returns to its oxidized form as soon as the chronoamperometry is stopped, as all the characteristic peaks of Nile Blue re-appear. By comparing the blue spectrum (before the chronoamperometry) with the yellow spectrum (after the chronoamperometry), it is evident that the peaks are the same, although less intense, probably due to sensor, or Nile Blue, degradation.

4.3.3 Sensor stability.

Once it has been verified that Nile Blue can be reduced via chronoamperometry at -0.66 V vs Fe(III)/Fe(II) for 60 seconds, it is important to understand how long the Nile Blue molecule adsorbed on the sensor remains reduced once the chronoamperometry is finished, namely at open circuit.

This evaluation was achieved by a continuous monitoring of Nile Blue SERS signals during subsequent cycles of chronoamperometry in a Spectro-Electrochemical setup. The final aim is to check how long Nile Blue takes to return to its oxidized form.

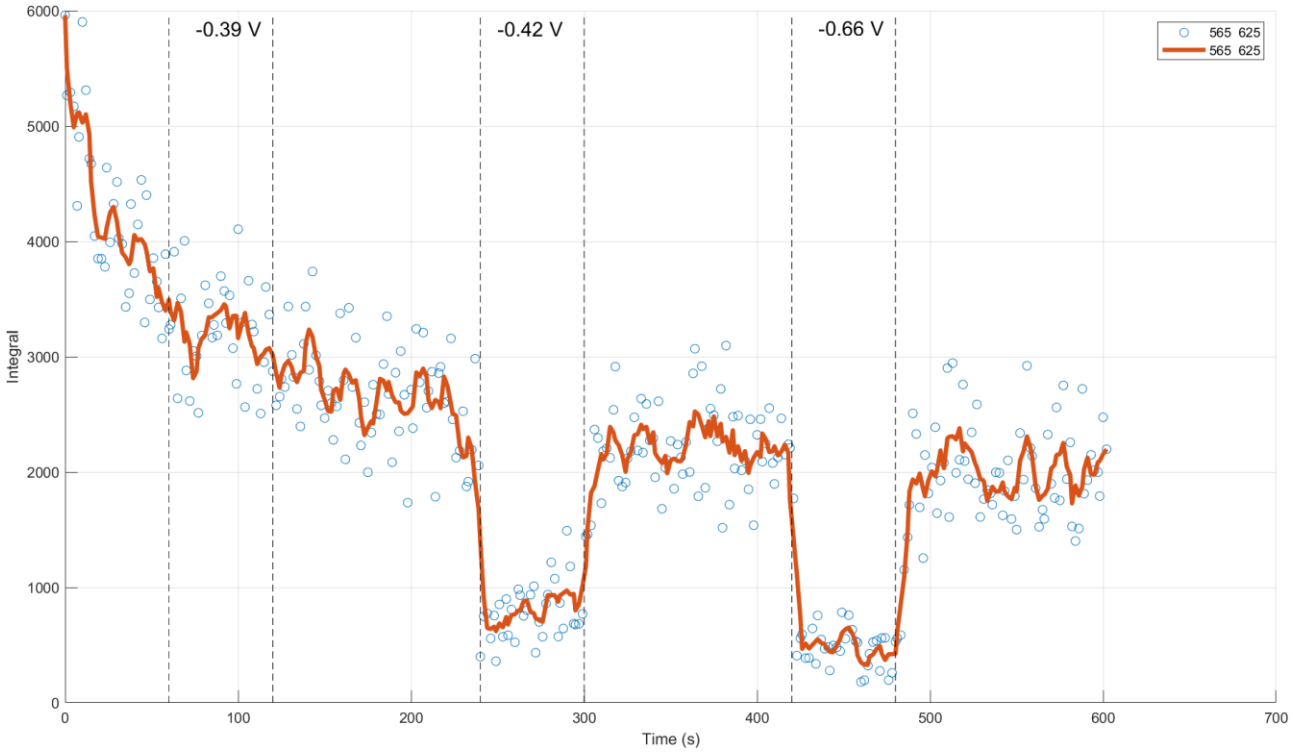

Figure 65: Raman spectra taken in 600 s. The acquisitions were static centered in 590 cm^{-1}, one spectrum each second, 785 nm line laser, 10x objective, laser power set at 6 mW. The acquisitions were taken while the chronoamperometries at different potentials were applied.

In Figure 65, the timing measurement is reported, lasting approximately 600 seconds. The measurement was carried out as described in paragraph 3.5.3, resumed in the following: initially, only the Raman measurement was present, and spectra were acquired every second at the Raman shift of 592 cm^{-1}, which corresponds to the characteristic peak of Nile Blue. A 785 nm laser line, 10x objective, and 6 mW laser power were used. Sixty seconds after the start of the test, a chronoamperometry was applied for one minute at a potential of -0.39 V vs Fe(III)/Fe(II), which corresponds to the reduction potential of hexavalent chromium, used as reference as it must not influence the Nile Blue. Subsequently, there were two minutes of spectra acquisition at open circuit, followed by another one-minute chronoamperometry, this time at a potential of -0.42 V vs Fe(III)/Fe(II), which refers to the first reduction of Nile Blue. Then, following the same procedure, a final chronoamperometry was performed at -0.66 V vs Fe(III)/Fe(II), representing the final reduction of the molecule. Once the chronoamperometry is finished, spectrum acquisition continues until the end of the measurement. Since the goal is to study the stability of the molecule in its reduced form, this experiment is conducted using only the phosphate buffer solution at pH 5 to avoid interference from the presence of chromium.

From the graph, it is quite evident that as soon as the chronoamperometry begins, the Nile Blue immediately reduces. In fact, for both the Nile Blue reduction potentials, there is an immediate zeroing of the intensity of the peak at 592 cm^{-1}. However, as soon as the sensor is no longer under forced reduction by the chronoamperometry, there is a very rapid, albeit gradual, increase in the characteristic peak of the molecule in question. This means that the Nile Blue promptly returns in its oxidized form.

The fact that the sensor, in its reduced form, is not stable over time makes much more challenging to detect hexavalent chromium in a solution. The reason why the Nile Blue molecule does not remain reduced after stopping the chronoamperometry, still remaining adsorbed, were postulated. The two most reasonable hypothesis are that chemical reoxidation is caused by the presence of oxidizing agents in the solution, such as oxygen, or that an electron transfer from Nile Blue to the gold nanoparticles happens, since the molecule is directly attached to the metal nanoparticles. Since the experiment was conducted with degassed aqueous solutions, the electronic transfer of Nile Blue to the gold nanoparticles sounds the more reasonable.

4.3.4 Response of functionalized sensor to solutions at different concentrations of Cr(VI)

After demonstrating that the reduced Nile Blue molecule is not stable over time, it was decided to keep it reduced using chronoamperometry at a potential of -0.66 V to ensure that all the Nile Blue adsorbed on the sensor was reduced.

From this point onward, only amperometric evaluation will be conducted using several solutions at different hexavalent chromium concentrations in the spectroelectrochemical cell. The measurement was carried out as follows: initially, the electrodes were placed inside the spectroelectrochemical cell, which was then filled with the electrolyte solution, in our case, phosphate buffer at a pH 5, and then covered with a coverslip. Once the cell is assembled, the electrodes are connected to the potentiostat, and the chronoamperometry is performed. inspired by Korshoj at al.[43], the sensor has been passivated with 6-mercapto-1-hexanol so that it is more difficult for chromium to directly reduce at the electrode, and the mediation through Nile Blue should result as the only way to electrochemically convert Cr(VI) to Cr(III). To verify that the passivation has been successful, chronoamperometries are performed even at chromium reduction potentials where NB should not react.

Both the blank sensor, without any adsorbed molecules on the surface, and the sensor functionalized with Nile Blue and subsequently passivated with 6-mercapto-1-hexanol were tested. The measurement is also performed on the blank sensor to observe how the gold nanoparticle responds to different concentrations of chromium, thus verifying its sensitivity without any adsorbed molecules. In this case, chronoamperometry is conducted at the reduction potential of hexavalent chromium. When measuring with the functionalized and passivated sensor, chronoamperometries are conducted both at -0.39 V and at -0.66 V vs Fe(III)/Fe(II).

Before performing the chronoamperometries both sensors, the blank and the functionalized one, were subjected to a cyclic voltammetry:

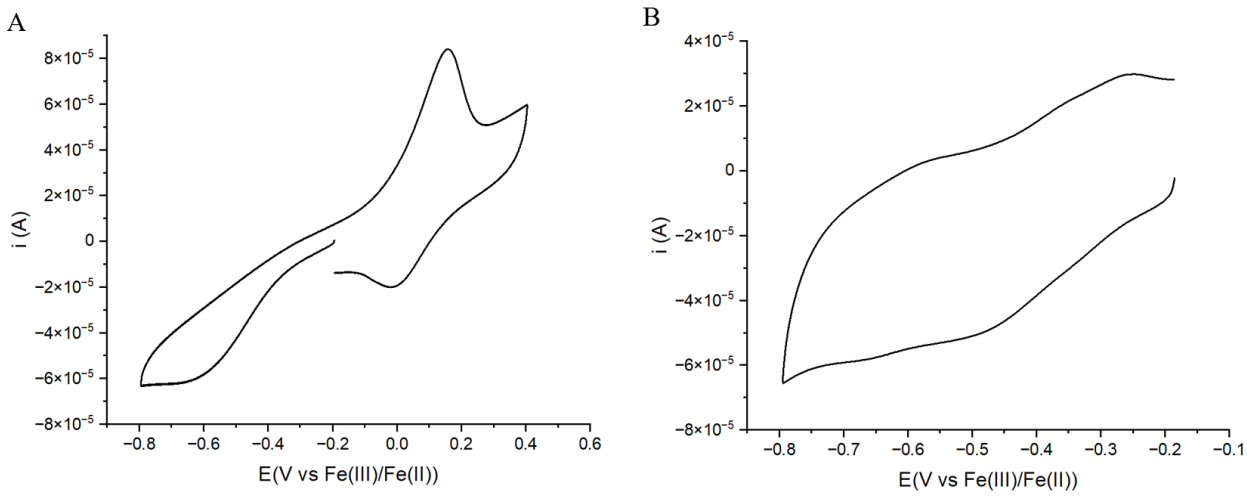

Figure 66: A) cyclic voltammetry of the blank sensor performed in the spectroelectrochemical cell at a scan rate of 0.1 V/s. B)) cyclic voltammetry of the functionalized and passivated sensor performed in the spectroelectrochemical cell at a scan rate of 0.1 V/s.

From Figure 66, it can be observed that for both sensors, the cyclic voltammetries appear to be tilted with a very high capacitive current, especially for the functionalized one in Figure 66b. This could occur due to the solution that may wets the contacts of the working electrode, resulting in an imprecise measurement and making it more difficult to identify the characteristic peaks. The behavior read by the potentiostat tends to increasingly resemble a resistor, meaning that the current becomes linearly dependent with the potential.

Given this issue, an attempt was made to perform a cyclic voltammetry of the same sensor first using a buffer solution and then a 0.1 M hexavalent chromium solution.

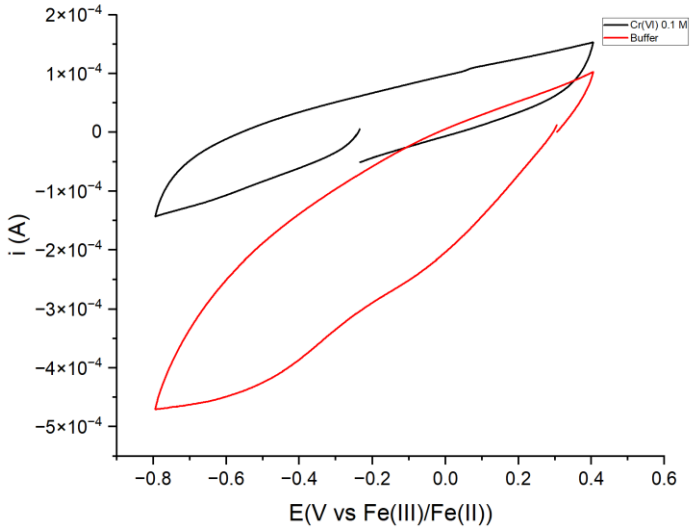

Figure 67: Cyclic voltammetry of the same sensor in buffer solution (in red) and in Cr(VI) 0.1 M solution (in black). Scan rate of 0.1 V/s. Both performed in the EC-SERS spectroelectrochemical cell.

From Figure 67, it can be observed that despite using the same sensor and the same electrolyte solution (buffer phosphate at pH 5) for both solutions, the currents are extremely different. The two voltammograms are severely distorted and the overall measure clearly invalidated. The reason for that is, probably, mainly attributed to hardware defects on the spectro-electrochemical cell, that properly works for the spectral acquisition, while it needs some adjustments about the stability of the electrical contacts for electrochemical measurements.

At this point, it was decided to proceed using a standard electrochemical setup, a three-electrode closed cell, as the values obtained using the spectroelectrochemical cell could not be considered reliable. The electrodes used in this setup are the same: a gold nanoparticle sensor produced via spray coating as the working electrode, a platinum wire as the counter electrode, and a silver wire in a saturated KCl solution as the pseudo-reference electrode. Before starting the chronoamperometric tests, a cyclic voltammetry was performed on both the bare sensor and the one

functionalized with Nile Blue and passivated with 6-mercapto-1-hexanol to see if there was an improvement in the signal using a conventional electrochemical cell.

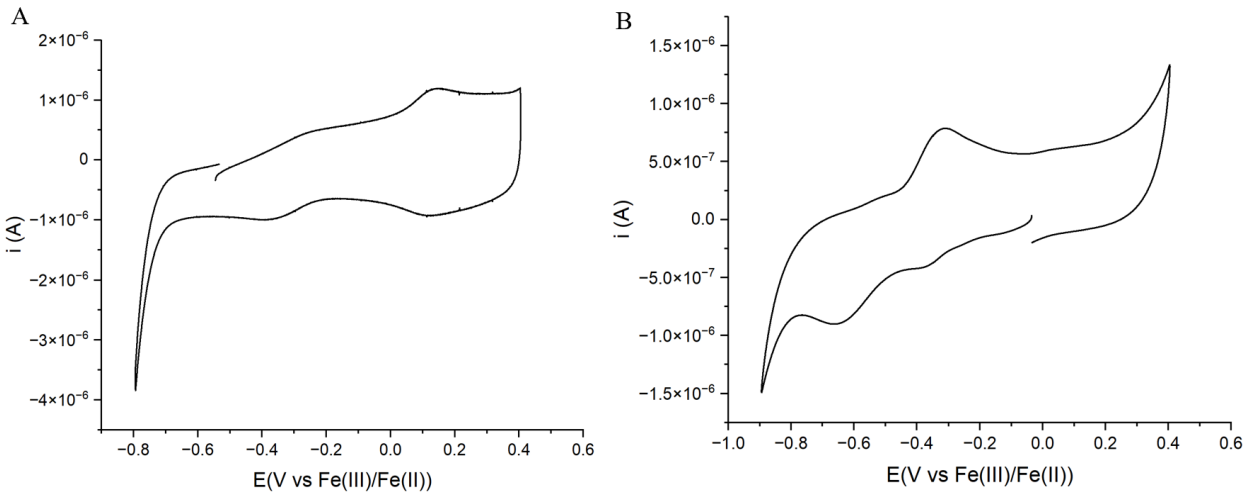

Figure 68: A) Cyclic voltammetry of the blank sensor performed in a conventional electrochemical cell, scan rate of 0.05 V/s. B) Cyclic voltammetry of the functionalized and passivated sensor performed in a conventional electrochemical cell, scan rate of 0.05 V/s.

Comparing the cyclic voltammograms shown in Figures 66 and 68, it is evident that the CVs performed inside the electrochemical cell (Fig. 68) are much less distorted, and the Nile Blue peaks reported in Figure 68b are significantly more pronounced.

Bare sensor

To determine the reduction potential of Cr(VI) for our AuNPs sensor, a DPV was performed in a Ferrocyanide solution to which a 1mM Cr(VI) solution was added (Fig 69).

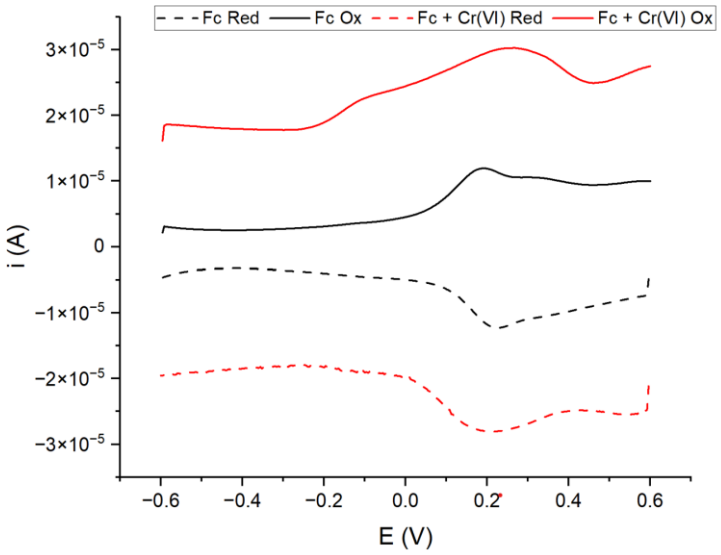

Figure 69: DPV of the bare sensor in a Ferrocyanide solution and in a Ferrocyanide solution adding Cr(VI) 1mM. The potentials are referred to our pseudo-reference electrode.

From Figure 69, it can be seen that the potential of Cr(VI) is at -0.1 V, which is -0.29 V vs Fe(III)/Fe(II), and that the peak is present only when scanning in the oxidation direction, while in the reduction one, the two DPVs are identical.

Initially, chronoamperometries are conducted for each chromium concentration on the bare sensor (namely not functionalized with Nile Blue) to study its sensitivity. The analyzed solutions have the following concentrations of Cr(VI): 0 M (Buffer solution), 0.01 µM, 0.05 µM, 0.1 µM, 0.5 µM, 1 µM, 5 µM, and each chronoamperometry was performed at a potential of -0.39 V vs Fe(III)/Fe(II) for 60 seconds.

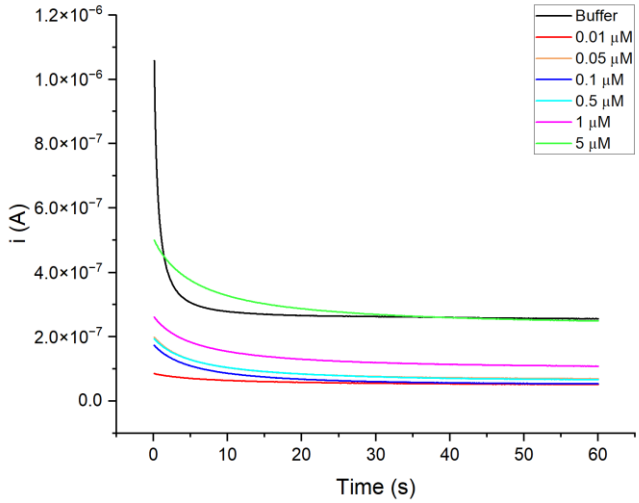

Figure 70: Chronoamperometries performed at -0.39 V for 60 seconds.

Following the procedure outlined in the reference article, [43] the current values were recorded for each concentration after 10 seconds from the start of the chronoamperometry:

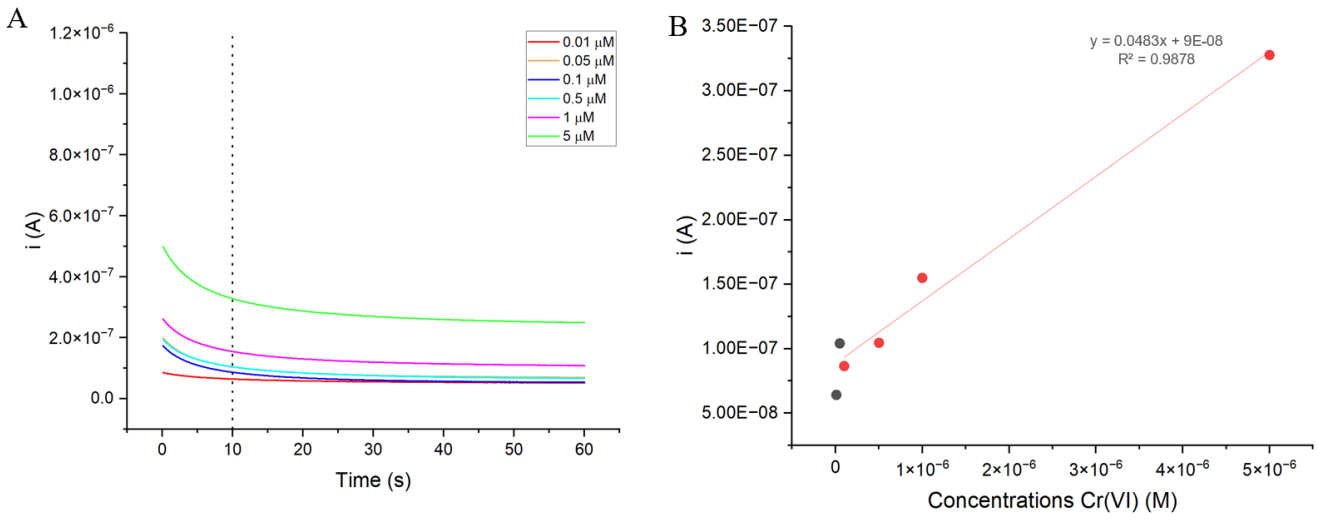

Figure 71: A) Chronoamperometries performed at -0.39 V vs Fe(III)/Fe(II) lasting 60s, buffer solution was not considered. B) response curve for Cr(VI) obtained using CA and by analyzing the change in the current after 10 seconds. Concentration above 10^{-7} M were considered.

As seen from the chronoamperometries shown in Figure 71a, the buffer solution has not been included as it appears to be an outlier, showing a current value that is too high to be compared with those of the other solutions. Upon careful examination of the values taken after 10s from the start of the chronoamperometries, a certain linearity can be observed up to concentrations of 0.1 µM, while for lower concentrations, the points appear to be too scattered. As reported in the red plot in Figure 71b, for concentrations up to 0.1 µM, the trend is linear with a R^2 value of 0.98.

Nile blue functionalized and passivated sensor

To see if the Nile Blue molecule leads to an improvement in sensor sensitivity, the measurement is repeated using a sensor functionalized with lipNB 60 µM and then passivated with 6-mercapto-1-hexanol 60 µM. Before connecting the sensor and placing it inside the electrochemical cell, it was examined using Raman spectroscopy with an extended spectrum and a Raman shift from 200 cm^{-1} to 2000 cm^{-1} to see if there was still any Nile Blue present or if the thiol replaced it by occupying all the sites on the sensor.

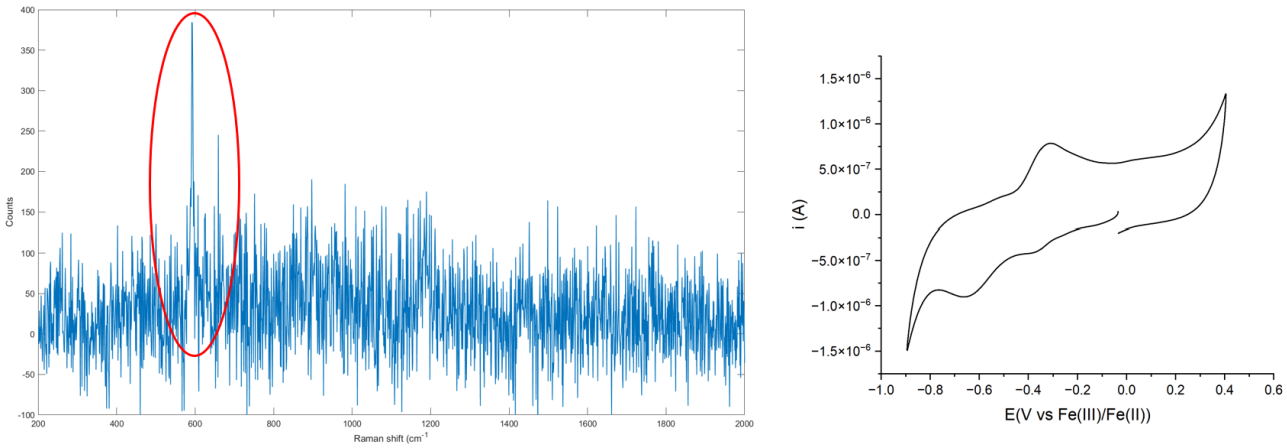

Figure 72: On the left the raman spectrum of the functionalized sensor with lipNB and then passivated with C_6OH, the line used was the 785 nm, with a laser power of 0.06 mW and a 10x objective. On the right a cyclic voltammetry of the same sensor done in a classic electrochemical setup.

As seen on the left of Figure 72, the Raman spectrum still shows, albeit at low intensity, the characteristic peak of Nile Blue at 592 cm^{-1}. Therefore, 6-mercapto-1-hexanol has not completely replaced Nile Blue. The same is also confirmed by the CV on the right of Figure 72, which clearly shows the two characteristic peaks at -0.32 V and -0.56 V vs Fe(III)/Fe(II) of the lipNB adsorbed on the sensor.

The analyzed solutions are the same as those used for the blank sensor, but this time the chronoamperometry is carried out both at the Cr(VI) reduction potential at -0.39 V vs Fe(III)/Fe(II),

to see if chromium reduces at the electrode or if the latter is isolated by the passivating layer, and at the second Nile Blue potential at -0.66 V vs Fe(III)/Fe(II).

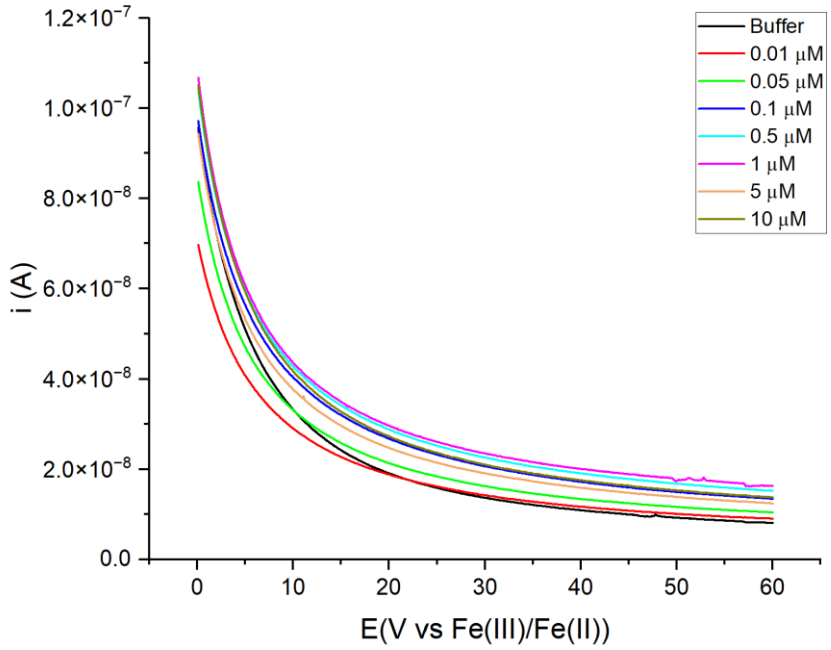

Figure 73: Chronoamperometries performed at -0.39 V vs Fe(III)/Fe(II) for 60 seconds for the functionalized sensor.

At a glance, the chronoamperometries shown in Figure 73 appear to be more similar to each other compared to those of the blank sensor reported in Figure 70. However, even in this case, to perform a more detailed analysis, it is necessary to consider the values taken at 10 seconds from the chronoamperometry.

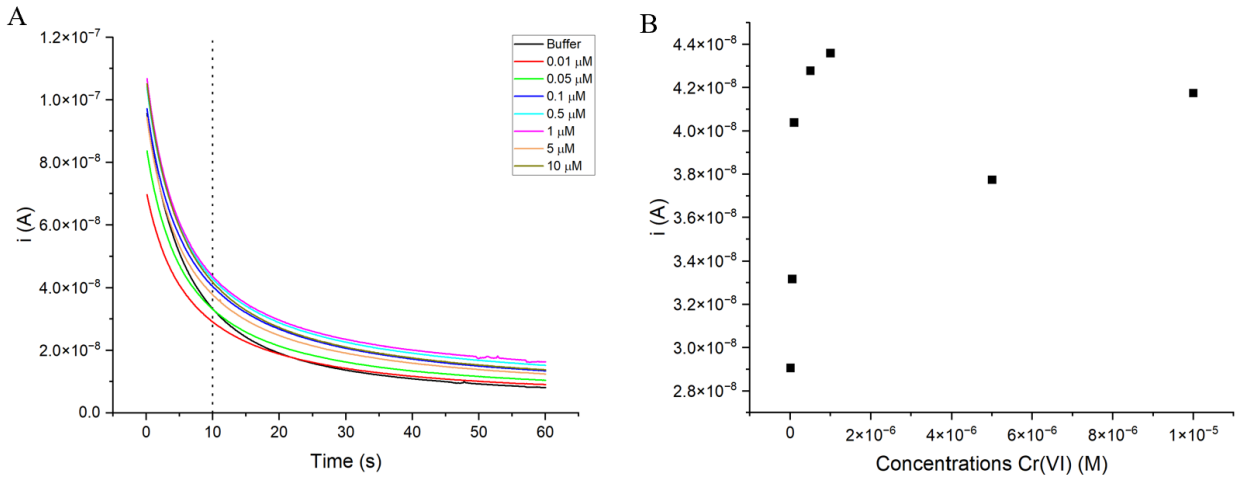

Figure 74:A) Chronoamperometries performed at -0.39 V vs Fe(III)/Fe(II) lasting 60s, buffer solution was not considered B) response curve for Cr(VI) obtained using CA and by analyzing the change in the current after 10 seconds. The buffer solution was not considered.

Also in this case, like in the previous one, the buffer solution has not been taken into account. Observing the curve shown in Figure 74b, the sensor seems to work well at low Cr(VI) concentrations

then reaches a plateau to saturation. This result could also depend on the fact that the reduction potential of chromium is not very far from the first reduction potential of Nile Blue, only a few millivolts apart (respectively -0.29 V and -0.32 V vs Fe(III)/Fe(II)), so the sensor's ability to detect such low concentrations of chromium could be attributed to Nile Blue.

Comparing the two sensors, the bare one (Fig. 71b) and the functionalized one (Fig. 74b), both subjected to chronoamperometry at -0.39 V vs Fe(III)/Fe(II), it is noticeable that the sensor functionalized with lipNB and passivated with 6-mercapto-1-hexanol shows a higher sensitivity to Cr(VI) probably because, at those reduction potentials during chronoamperometry, the Nile Blue molecule facilitates the reduction of Cr(VI) to Cr(III).

After studying how the sensor behaves by performing the chronoamperometry at -0.39 V, the experiment is repeated analyzing the sensor response to chronoamperometries carried out at -0.66 V vs Fe(III)/Fe(II), the second potential of Nile Blue.

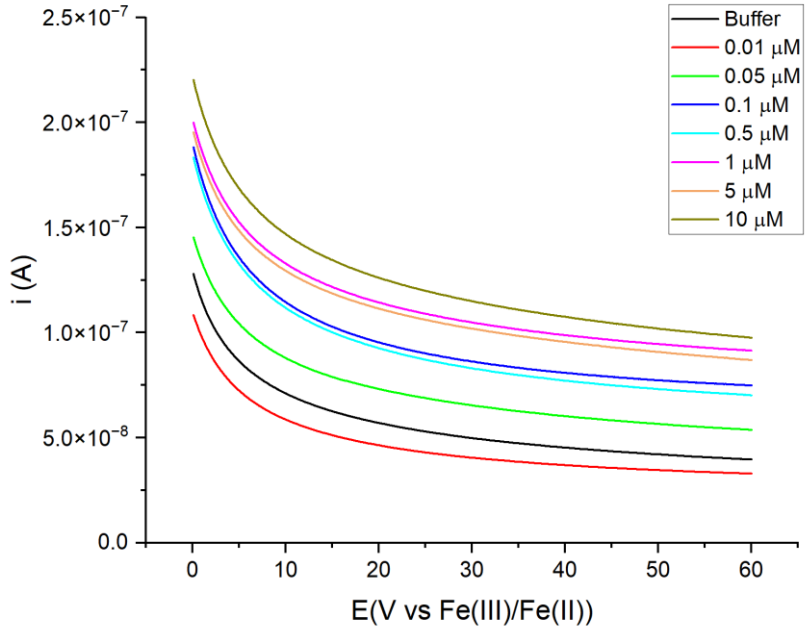

Figure 75: Chronoamperometries performed at -0.66 V vs Fe(III)/Fe(II) for 60 seconds for the functionalized sensor.

Looking at the chronoamperometries shown in Figure 75, it is noticeable that once again the buffer has an anomalous behavior and that for low values of Cr(VI) there seems to be a trend.

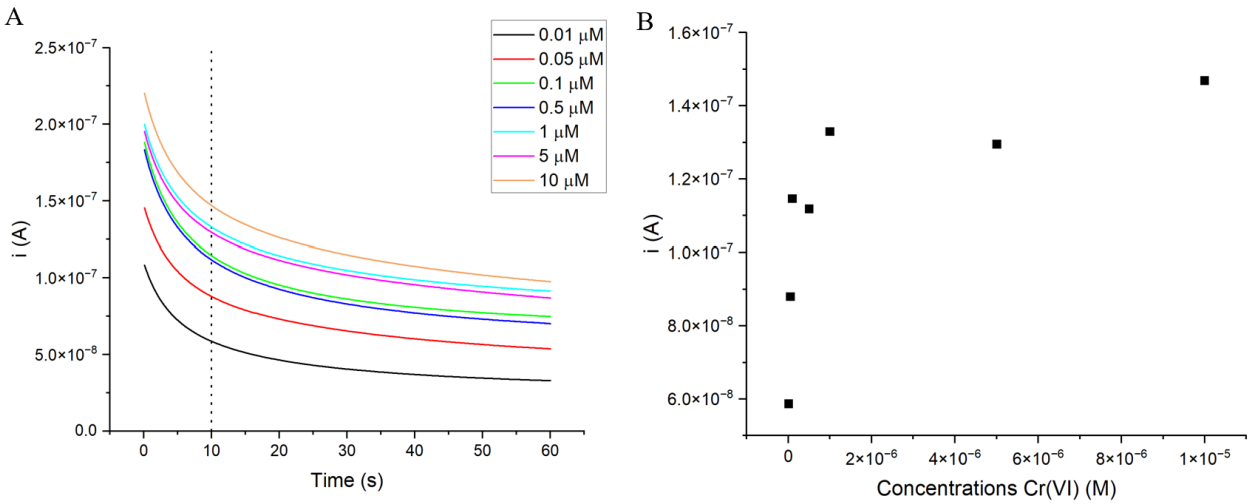

Figure 76:A) Chronoamperometries performed at -0.66 V vs Fe(III)/Fe(II) lasting 60s, buffer solution was not considered B) response curve for Cr(VI) obtained using CA and by analyzing the change in the current after 10 seconds. The buffer solution was not considered.

From the plot in Figure 76b, it is already noticeable that there is a similar trend as the one shown in Figure 74b. Once again there is a sensitivity for low concentration (0.01 µM) of hexavalent chromium and after reaching a concentration of 0.1 µM the sensor presents a saturation.

The plateau that is probably due to the sensor's saturation, meaning that there are no more Nile Blue molecules available to be re-oxidized by the hexavalent chromium.

5. Conclusions and perspectives

The detection of hexavalent chromium in water is crucial for human health and environmental protection. This contaminant is highly toxic and carcinogenic and its presence in water resources poses a significant threat to aquatic ecosystems, causing death of organisms and ecological alterations.

This thesis aims to detect hexavalent chromium in two ways: through a SERS-based method using DPC as reagent, and through a Spectro-electrochemical technique that utilizes sensor functionalization with lipNB. In both cases, the importance of producing the sensor with gold nanoparticles is highlighted, and how the sensor's production technique can influence its sensitivity.

From this work, it can be concluded that an unfunctionalized sensor composed solely of gold nanoparticles of around 15-20 nm, devoid of stabilizers and directly sprayed onto the sensor using the spray coating technique, exhibits good sensitivity for detecting hexavalent chromium concentrations above 10^{-7} M. This is the same limit that was reached using the DPC reagent on a sensor produced via drop casting, despite with a dilution of the Cr(DPCO) complex. Therefore, the sensor produced through spray coating might have shown a better sensitivity if utilized with the same reagent to detect hexavalent chromium, due to better homogeneity of the SERS performances. The sensitivity of the sensor changes when it is functionalized with the Nile Blue molecule. While using a bare sensor a correlation could only be made for concentrations from 10^{-7} M and above, once the sensor is functionalized, it becomes sensitive to concentrations ranging from 10^{-8} M to 10^{-7} M, with saturation occurring at higher concentrations.

Regarding the use of the electrochemical cell, it has demonstrated its capability to support the measurement, indicating that it could be used for Spectro-electrochemical measurements once the setup is improved to ensure that the contacts are well insulated by the electrolyte solution.

Possible improvements for this project certainly include the higher degree of functionalization of the Nile Blue molecule on the electrode, as this could be the main issue causing the sensor to show saturation at relatively low chromium concentrations. For the same reason, the surface area might be increased so that more Nile Blue molecules can be placed on the surface. Also, improving sensor production would help to increase its conductivity.

6. References

(1) Humans, I. W. G. on the E. of C. R. to. CHROMIUM AND CHROMIUM COMPOUNDS. In *Chromium, Nickel and Welding*; International Agency for Research on Cancer, 1990.

(2) Unceta, N.; Séby, F.; Malherbe, J.; Donard, O. F. X. Chromium Speciation in Solid Matrices and Regulation: A Review. *Anal. Bioanal. Chem.* **2010**, *397* (3), 1097–1111. https://doi.org/10.1007/s00216-009-3417-1.

(3) Masindi, V.; Muedi, K. L.; Masindi, V.; Muedi, K. L. Environmental Contamination by Heavy Metals. In *Heavy Metals*; IntechOpen, 2018. https://doi.org/10.5772/intechopen.76082.

(4) Achmad, R.; Budiawan, B.; Auerkari, E. Effects of Chromium on Human Body. *Annu. Res. Rev. Biol.* **2017**, *13*, 1–8. https://doi.org/10.9734/ARRB/2017/33462.

(5) *Chromium (Cr) Toxicity: What are the Standards and Regulations for Chromium Exposure? | Environmental Medicine | ATSDR*. https://www.atsdr.cdc.gov/csem/chromium/standards_and_regulations.html (accessed 2024-03-27).

(6) Maccarelli, M. *Valori limite cromo nelle acque consumo umano*. Certifico Srl. https://www.certifico.com/ambiente/legislazione-ambiente/287-legislazione-acque/18763-valori-limite-cromo-nelle-acque-consumo-umano (accessed 2024-03-27).

(7) Metze, D.; Jakubowski, N.; Klockow, D. Speciation of Chromium. In *Handbook of Elemental Speciation II – Species in the Environment, Food, Medicine and Occupational Health*; John Wiley & Sons, Ltd, 2005; pp 120–135. https://doi.org/10.1002/0470856009.ch2f(i).

(8) Markiewicz, B.; Komorowicz, I.; Sajnóg, A.; Belter, M.; Barałkiewicz, D. Chromium and Its Speciation in Water Samples by HPLC/ICP-MS – Technique Establishing Metrological Traceability: A Review since 2000. *Talanta* **2015**, *132*, 814–828. https://doi.org/10.1016/j.talanta.2014.10.002.

(9) Michalski, R. Ion Chromatography Method for the Determination of Trace Levels of Chromium(VI) in Water.

(10) Ion Chromatography (IC) ICP-MS for Chromium Speciation in Natural Samples.

(11) Garcia-Miranda Ferrari, A.; Crapnell, R. D.; Adarakatti, P. S.; Suma, B. P.; Banks, C. E. Electroanalytical Overview: The Detection of Chromium. *Sens. Actuators Rep.* **2022**, *4*, 100116. https://doi.org/10.1016/j.snr.2022.100116.

(12) Domínguez-Renedo, O.; Ruiz-Espelt, L.; García-Astorgano, N.; Arcos-Martínez, M. J. Electrochemical Determination of Chromium(VI) Using Metallic Nanoparticle-Modified

Carbon Screen-Printed Electrodes. *Talanta* **2008**, *76* (4), 854–858. https://doi.org/10.1016/j.talanta.2008.04.036.

(13) Sari, T. K.; Takahashi, F.; Jin, J.; Zein, R.; Munaf, E. Electrochemical Determination of Chromium(VI) in River Water with Gold Nanoparticles-Graphene Nanocomposites Modified Electrodes. *Anal. Sci.* **2018**, *34* (2), 155–160. https://doi.org/10.2116/analsci.34.155.

(14) Liu, S.; Lu, F.; Zhu, J.-J. Highly Fluorescent Ag Nanoclusters: Microwave-Assisted Green Synthesis and Cr3+ Sensing. *Chem. Commun.* **2011**, *47* (9), 2661–2663. https://doi.org/10.1039/C0CC04276E.

(15) Zhang, L.; Xu, C.; Li, B. Simple and Sensitive Detection Method for Chromium(VI) in Water Using Glutathione—Capped CdTe Quantum Dots as Fluorescent Probes. *Microchim. Acta* **2009**, *166* (1), 61–68. https://doi.org/10.1007/s00604-009-0164-0.

(16) Liu, L.; Leng, Y.; Lin, H. Photometric and Visual Detection of Cr(VI) Using Gold Nanoparticles Modified with 1,5-Diphenylcarbazide. *Microchim. Acta* **2016**, *183* (4), 1367–1373. https://doi.org/10.1007/s00604-016-1777-8.

(17) Liu, Y.; Wang, X. Colorimetric Speciation of Cr(III) and Cr(VI) with a Gold Nanoparticle Probe. *Anal. Methods* **2013**, *5* (6), 1442–1448. https://doi.org/10.1039/C3AY00016H.

(18) Tan, F.; Liu, X.; Quan, X.; Chen, J.; Li, X.; Zhao, H. Selective Detection of Nanomolar Cr(VI) in Aqueous Solution Based on 1,4-Dithiothreitol Functionalized Gold Nanoparticles. *Anal. Methods* **2011**, *3* (2), 343–347. https://doi.org/10.1039/C0AY00534G.

(19) Zhou, W.; Yin, B.-C.; Ye, B.-C. Highly Sensitive Surface-Enhanced Raman Scattering Detection of Hexavalent Chromium Based on Hollow Sea Urchin-like TiO2@Ag Nanoparticle Substrate. *Biosens. Bioelectron.* **2017**, *87*, 187–194. https://doi.org/10.1016/j.bios.2016.08.036.

(20) Ahmad, W.; Hassan, M. M.; Wang, J.; Zareef, M.; Annavaram, V.; Chen, Q. An Octahedral Cu2O@AgNCs Substrate in Liquid-Microextraction Coupled Chemometric Algorithms for SERS Sensing of Chromium(III & VI) Species. *Anal. Methods* **2019**, *11* (47), 6004–6012. https://doi.org/10.1039/C9AY01584A.

(21) Elgrishi, N.; Rountree, K. J.; McCarthy, B. D.; Rountree, E. S.; Eisenhart, T. T.; Dempsey, J. L. A Practical Beginner's Guide to Cyclic Voltammetry. *J. Chem. Educ.* **2018**, *95* (2), 197–206. https://doi.org/10.1021/acs.jchemed.7b00361.

(22) Bard, A. J.; Faulkner, L. R.; White, H. S. *Electrochemical Methods: Fundamentals and Applications*; John Wiley & Sons, 2022.

(23) Cho, Y.; Ahn, S. Fabricating a Raman Spectrometer Using an Optical Pickup Unit and Pulsed Power. *Sci. Rep.* **2020**, *10*. https://doi.org/10.1038/s41598-020-68650-7.

(24) Asher, S. A. UV Resonance Raman Spectroscopy for Analytical, Physical, and Biophysical Chemistry. *Anal. Chem.* **1993**, *65* (4), 201A-210A. https://doi.org/10.1021/ac00052a715.

(25) The Theory of Raman Spectroscopy. In *Modern Raman Spectroscopy*; John Wiley & Sons, Ltd, 2019; pp 77–99. https://doi.org/10.1002/9781119440598.ch3.

(26) Fenner, W. R.; Hyatt, H. A.; Kellam, J. M.; Porto, S. P. S. Raman Cross Section of Some Simple Gases. *J. Opt. Soc. Am.* **1973**, *63* (1), 73. https://doi.org/10.1364/JOSA.63.000073.

(27) Ferraro, J. R.; Nakamoto, K.; Brown, C. W. Introductory Raman Spectroscopy: Second Edition. *Introd. Raman Spectrosc. Second Ed.* **2003**, 1–434.

(28) Fleischmann, M.; Hendra, P. J.; McQuillan, A. J. Raman Spectra of Pyridine Adsorbed at a Silver Electrode. *Chem. Phys. Lett.* **1974**, *26* (2), 163–166. https://doi.org/10.1016/0009-2614(74)85388-1.

(29) Ma, H.; Pan, S.-Q.; Wang, W.-L.; Yue, X.; Xi, X.-H.; Yan, S.; Wu, D.-Y.; Wang, X.; Liu, G.; Ren, B. Surface-Enhanced Raman Spectroscopy: Current Understanding, Challenges, and Opportunities. *ACS Nano* **2024**, *18* (22), 14000–14019. https://doi.org/10.1021/acsnano.4c02670.

(30) Kumar, S.; Kumar, P.; Das, A.; Pathak, C. S.; Kumar, S.; Kumar, P.; Das, A.; Pathak, C. S. Surface-Enhanced Raman Scattering: Introduction and Applications. In *Recent Advances in Nanophotonics - Fundamentals and Applications*; IntechOpen, 2020. https://doi.org/10.5772/intechopen.92614.

(31) Le Ru, E. C.; Blackie, E.; Meyer, M.; Etchegoin, P. G. Surface Enhanced Raman Scattering Enhancement Factors: A Comprehensive Study. *J. Phys. Chem. C* **2007**, *111* (37), 13794–13803. https://doi.org/10.1021/jp0687908.

(32) Jones, R. R.; Hooper, D. C.; Zhang, L.; Wolverson, D.; Valev, V. K. Raman Techniques: Fundamentals and Frontiers. *Nanoscale Res. Lett.* **2019**, *14* (1), 231. https://doi.org/10.1186/s11671-019-3039-2.

(33) Sobuz, S. uddin ahmed. Principles of Surface Enhanced Raman Spectroscopy.

(34) Yang, X.; Su, D.; Yu, X.; Zeng, P.; Liang, H.; Zhang, G.; Song, B.; Jiang, S. Hot Spot Engineering in Hierarchical Plasmonic Nanostructures. *Small* **2023**, *19* (22), 2205659. https://doi.org/10.1002/smll.202205659.

(35) Israelsen, N. D.; Hanson, C.; Vargis, E. Nanoparticle Properties and Synthesis Effects on Surface-Enhanced Raman Scattering Enhancement Factor: An Introduction. *Sci. World J.* **2015**, *2015*, 124582. https://doi.org/10.1155/2015/124582.

(36) Stockman, M. I. Nanoplasmonics: The Physics behind the Applications. *Phys. Today* **2011**, *64* (2), 39–44. https://doi.org/10.1063/1.3554315.

(37) Mosier-Boss, P. A. Review of SERS Substrates for Chemical Sensing. *Nanomaterials* **2017**, *7* (6), 142. https://doi.org/10.3390/nano7060142.

(38) Le Ru, E. C.; Etchegoin, P. G. Chapter 7 - Metallic Colloids and Other SERS Substrates. In *Principles of Surface-Enhanced Raman Spectroscopy*; Le Ru, E. C., Etchegoin, P. G., Eds.; Elsevier: Amsterdam, 2009; pp 367–413. https://doi.org/10.1016/B978-0-444-52779-0.00013-1.

(39) Abid, N.; Khan, A. M.; Shujait, S.; Chaudhary, K.; Ikram, M.; Imran, M.; Haider, J.; Khan, M.; Khan, Q.; Maqbool, M. Synthesis of Nanomaterials Using Various Top-down and Bottom-up Approaches, Influencing Factors, Advantages, and Disadvantages: A Review. *Adv. Colloid Interface Sci.* **2022**, *300*, 102597. https://doi.org/10.1016/j.cis.2021.102597.

(40) Amendola, V.; Meneghetti, M. Laser Ablation Synthesis in Solution and Size Manipulation of Noble Metal Nanoparticles. *Phys. Chem. Chem. Phys.* **2009**, *11* (20), 3805–3821. https://doi.org/10.1039/B900654K.

(41) Sylvestre, J.-P.; Poulin, S.; Kabashin, A.; Meunier, M.; Luong, J. Surface Chemistry of Gold Nanoparticles Produced by Laser Ablation in Aqueous Media. *J. Phys. Chem. B* **2004**. https://doi.org/10.1021/jp047134+.

(42) Eisnor, M. M.; McLeod, K. E. R.; Bindesri, S.; Svoboda, S. A.; Wustholz, K. L.; Brosseau, C. L. Electrochemical Surface-Enhanced Raman Spectroscopy (EC-SERS): A Tool for the Identification of Polyphenolic Components in Natural Lake Pigments. *Phys. Chem. Chem. Phys.* **2021**, *24* (1), 347–356. https://doi.org/10.1039/D1CP03301H.

(43) Korshoj, L. E.; Zaitouna, A. J.; Lai, R. Y. Methylene Blue-Mediated Electrocatalytic Detection of Hexavalent Chromium. *Anal. Chem.* **2015**, *87* (5), 2560–2564. https://doi.org/10.1021/acs.analchem.5b00197.

(44) Acosta, E. Thin Films/Properties and Applications. In *Thin Films*; IntechOpen, 2021. https://doi.org/10.5772/intechopen.95527.

(45) Kaliyaraj Selva Kumar, A.; Zhang, Y.; Li, D.; Compton, R. G. A Mini-Review: How Reliable Is the Drop Casting Technique? *Electrochem. Commun.* **2020**, *121*, 106867. https://doi.org/10.1016/j.elecom.2020.106867.

(46) Lohse, D. Fundamental Fluid Dynamics Challenges in Inkjet Printing. *Annu. Rev. Fluid Mech.* **2022**, *54* (Volume 54, 2022), 349–382. https://doi.org/10.1146/annurev-fluid-022321-114001.

(47) Hoath, S. D. *Fundamentals of Inkjet Printing: The Science of Inkjet and Droplets*; John Wiley & Sons, 2016.

(48) Shah, M. A.; Lee, D.-G.; Lee, B.-Y.; Hur, S. Classifications and Applications of Inkjet Printing Technology: A Review. *IEEE Access* **2021**, *9*, 140079–140102. https://doi.org/10.1109/ACCESS.2021.3119219.

(49) Hussain, Z.; Kiaee, Z.; Nazarzadeh, M.; Reichel, C.; Tepner, S.; Tuladhar, T.; Jahn, M.; Keding, R. High-Frequency Rheological and Piezo-Voltage Waveform Characterization of Inkjet-Printed Polymer-Based Dopant-Source Inks. *Micromachines* **2023**, *14* (1), 80. https://doi.org/10.3390/mi14010080.

(50) Zhang, Y.; Hu, G.; Liu, Y.; Wang, J.; Yang, G.; Li, D. Suppression and Utilization of Satellite Droplets for Inkjet Printing: A Review. *Processes* **2022**, *10* (5), 932. https://doi.org/10.3390/pr10050932.

(51) Green, R.; Morfa, A.; Ferguson, A. J.; Kopidakis, N.; Rumbles, G.; Shaheen, S. E. Performance of Bulk Heterojunction Photovoltaic Devices Prepared by Airbrush Spray Deposition. *Appl. Phys. Lett.* **2008**, *92* (3), 033301. https://doi.org/10.1063/1.2836267.

(52) Abdellah, A.; Baierl, D.; Fabel, B.; Lugli, P.; Scarpa, G. Spray-Coating Deposition for Large Area Organic Thin-Film Devices; 2009.

(53) Lee, J.; Yoshikawa, S.; Sagawa, T. Fabrication of Efficient Organic and Hybrid Solar Cells by Fine Channel Mist Spray Coating. *Sol. Energy Mater. Sol. Cells* **2014**, *127*, 111–121. https://doi.org/10.1016/j.solmat.2014.04.010.

(54) Sciutto, G.; Litti, L.; Lofrumento, C.; Prati, S.; Ricci, M.; Gobbo, M.; Roda, A.; Castellucci, E.; Meneghetti, M.; Mazzeo, R. Alternative SERRS Probes for the Immunochemical Localization of Ovalbumin in Paintings: An Advanced Mapping Detection Approach. *Analyst* **2013**, *138* (16), 4532–4541. https://doi.org/10.1039/C3AN00057E.

(55) D. Casimir, H. Alghamdi, I. y. Ahmed, R. Garcia-Sanchez, P. Misra *Raman Spectroscopy of Graphene, Graphite and Graphene Nanoplatelets **2019*** 10.5772/intechopen.84527.

(56) *B. Manggalaa, C. Chaichana, W. Syahputra, W. Wongwilai Pesticide Residues Detection in Agricultural Products Nat. Life Sci. Commun. **2023***.

(57) Litti, L.; Meneghetti, M. Predictions on the SERS Enhancement Factor of Gold Nanosphere Aggregate Samples. *Phys. Chem. Chem. Phys.* **2019**, *21* (28), 15515–15522. https://doi.org/10.1039/C9CP02015B.

(58) Manapat, J. Z.; Chen, Q.; Ye, P.; Advincula, R. C. 3D Printing of Polymer Nanocomposites via Stereolithography. *Macromol. Mater. Eng.* **2017**, *302* (9), 1600553. https://doi.org/10.1002/mame.201600553.

(59) Haiss, W.; Thanh, N. T. K.; Aveyard, J.; Fernig, D. G. Determination of Size and Concentration of Gold Nanoparticles from UV−Vis Spectra. *Anal. Chem.* **2007**, *79* (11), 4215–4221. https://doi.org/10.1021/ac0702084.

(60) Ricci, S.; Buonomo, M.; Casalini, S.; Bonacchi, S.; Meneghetti, M.; Litti, L. High Performance Multi-Purpose Nanostructured Thin Films by Inkjet Printing: Au Micro-Electrodes and SERS Substrates. *Nanoscale Adv.* **2023**, *5* (7), 1970–1977. https://doi.org/10.1039/D2NA00917J.

(61) Thambiliyagodage, C. Ligand Exchange Reactions and PEG Stabilization of Gold Nanoparticles. *Curr. Res. Green Sustain. Chem.* **2022**, *5*, 100245. https://doi.org/10.1016/j.crgsc.2021.100245.

(62) Ragheb, I.; Braïk, M.; Lau-Truong, S.; Belkhir, A.; Rumyantseva, A.; Kostcheev, S.; Adam, P.-M.; Chevillot-Biraud, A.; Lévi, G.; Aubard, J.; Boubekeur-Lecaque, L.; Félidj, N. Surface Enhanced Raman Scattering on Regular Arrays of Gold Nanostructures: Impact of Long-Range Interactions and the Surrounding Medium. *Nanomater. Basel Switz.* **2020**, *10* (11), 2201. https://doi.org/10.3390/nano10112201.

(63) Laura Bizzo, Study and optimization of EC-SERS techniques for in-situ speciation of Cr(III) and Cr(VI), tesi di laurea 2021.

(64) Mažeikienė, R.; Niaura, G.; Eicher-Lorka, O.; Malinauskas, A. Raman Spectroelectrochemical Study of Redox Dye Nile Blue Adsorbed or Electropolymerised at a Gold Electrode. *Chemija* **2019**, *30* (2). https://doi.org/10.6001/chemija.v30i2.3997.

(65) Wilson, A. J.; Molina, N. Y.; Willets, K. A. Modification of the Electrochemical Properties of Nile Blue through Covalent Attachment to Gold As Revealed by Electrochemistry and SERS. *J. Phys. Chem. C* **2016**, *120* (37), 21091–21098. https://doi.org/10.1021/acs.jpcc.6b03962.